AERODYNAMIC AND THREE-DEGREE-OF-FREEDOM FLIGHT MECHANICS ANALYSIS OF A SLENDER BODY OF RECTANGULAR CROSS SECTION

A THESIS SUBMITTED TO
THE GRADUATE SCHOOL OF NATURAL AND APPLIED SCIENCES
OF
MIDDLE EAST TECHNICAL UNIVERSITY

BY

BAHRİ TUĞCAN SELİMHOCAOĞLU

IN PARTIAL FULFILLMENT OF THE REQUIREMENTS
FOR
THE DEGREE OF MASTER OF SCIENCE
IN
AEROSPACE ENGINEERING

JUNE 2014

Approval of the thesis:

AERODYNAMIC AND THREE-DEGREE-OF-FREEDOM FLIGHT MECHANICS ANALYSIS OF A SLENDER BODY OF RECTANGULAR CROSS SECTION

submitted by **BAHRİ TUĞCAN SELİMHOCAOĞLU** in partial fulfillment of the requirements for the degree of **Master of Science in Aerospace Engineering Department, Middle East Technical University** by,

Prof. Dr. Canan Özgen _________________________
Dean, Graduate School of **Natural and Applied Sciences**

Prof. Dr. Ozan Tekinalp _________________________
Head of Department, **Aerospace Engineering**

Prof. Dr. Yusuf Özyörük _________________________
Supervisor, **Aerospace Engineering Dept., METU**

Prof. Dr. Nafiz Alemdaroğlu _________________________
Co-Supervisor, **Aerospace Engineering Dept., METU**

Examining Committee Members:

Prof. Dr. İsmail H. Tuncer _________________________
Aerospace Engineering Dept., METU

Prof. Dr. Serkan Özgen _________________________
Aerospace Engineering Dept., METU

Prof. Dr. Nafiz Alemdaroğlu _________________________
Aerospace Engineering Dept., METU

Prof. Dr. Kemal Özgören _________________________
Mechanical Engineering Dept., METU

Prof. Dr. Yusuf Özyörük _________________________
Aerospace Engineering Dept., METU

Date: 27.06.2014

I hereby declare that all information in this document has been obtained and presented in accordance with academic rules and ethical conduct. I also declare that, as required by these rules and conduct, I have fully cited and referenced all material and results that are not original to this work.

Name, Surname: Bahri Tuğcan SELİMHOCAOĞLU

Signature:

ABSTRACT

AERODYNAMIC AND THREE-DEGREE-OF-FREEDOM FLIGHT MECHANICS ANALYSIS OF A SLENDER BODY OF RECTANGULAR CROSS SECTION

Selimhocaoğlu, Bahri Tuğcan

M. Sc., Department of Aerospace Engineering

Supervisor : Prof. Dr. Yusuf Özyörük

Co-Supervisor : Prof. Dr. Nafiz Alemdaroğlu

June 2014, 108 pages

A slender body with rectangular cross section is considered as an aircraft countermeasure for self-protection purposes as a decoy. An initial design is necessary, for the detailed aerodynamic design of the decoy. For quick initial design purposes, three-degree-of-freedom (longitudinal, vertical, pitching) dynamic analyses of the decoy are carried out. The aerodynamic coefficients for the decoy are obtained first at different Mach numbers, angles of attack, and tail sizes with two different methodologies which are DatCOM and steady CFD analyses utilizing RANS. The comparison of these two methodologies showed that CFD results are more reliable than the DatCOM results. The aerodynamic coefficients are then input to a code numerically implementing the 3DOF motion of the decoy at different Mach numbers, center of gravity values and tail sizes. The aerodynamic coefficients necessary for this method are obtained assuming quasi-steady conditions exist, that is the angle of attack corresponding to the time of 3DOF simulation is frozen and aerodynamic coefficients are computed accordingly. For the assessment of the initial design methodology, grid independence, selection of time step for both the numerical implementation and the transient CFD analyses are considered. Also, the comparison of transient 3DOF CFD and 6DOF CFD analyses are carried out as an evaluation of 3DOF approach. The matrix of results obtained from the 3DOF numerical implementation are compared with the transient 6DOF CFD analyses. According to the results, provided the decoy has static stability, the 3DOF initial design methodology is able to capture the trend of the parameter variations, the trajectory of the decoy and the pitching angle oscillations in a conservative manner. Hence, this approach is deemed sufficient for initial design purposes of the decoy.

Keywords: Decoy, Slender Body, Rectangular Cross Section, Initial Design, 3DOF, Flight Mechanics, CFD, DatCOM, Fluent.

ÖZ

DİKDÖRTGEN KESİTLİ İNCE UZUN BİR GÖVDENİN AERODİNAMİK VE 3 SERBESTLİK DERECELİ UÇUŞ MEKANİĞİ ANALİZİ

Selimhocaoğlu, Bahri Tuğcan
Yüksek Lisans, Havacılık ve Uzay Mühendisliği Bölümü
Tez Yöneticisi : Prof. Dr. Yusuf Özyörük
Ortak Tez Yöneticisi : Prof. Dr. Nafiz Alemdaroğlu

Haziran 2014, 108 sayfa

Dikdörtgen kesit alanlı bir aerodinamik gövde uçaklarda kendini koruma amacı ile kullanılacaktır. Aerodinamik gövdenin tasarımını yapabilmek için, bir ilk tasarıma ihtiyaç duyulmaktadır. İlk tasarıma hızlı bir şekilde erişebilmek için 3 serbestlik derecesinde (yatay, dikey ve yunuslama yönlerinde) dinamik analizler gerçekleştirilmesine karar verilmiştir. Öncelikle gövdenin aerodinamik katsayılarını bulabilmek için farklı hızlarda, hücum açılarında ve kuyruk alanı değerlerinde hem DatCom kullanılmış hem de zamandan bağımsız Navier Stokes denklemlerini çözen HAD (Hesaplamalı Akışkanlar Dinamiği) analizleri koşturulmuştur. Yapılan karşılaştırmalara göre HAD sonuçlarının söz edilen aerodinamik gövde için daha güvenilir olduğu değerlendirilmiştir. Elde edilen aerodinamik katsayılar, dinamik analizleri gerçekleştiren bir koda girdi olarak sağlanmıştır. Kod, aerodinamik gövdenin dinamik hareketini farklı Mach sayılarında, ağırlık merkezi değerlerinde ve kuyruk boyutlarında 3 serbestlik derecesinde zamandan bağımsız olarak elde edilen aerodinamik katsayılarla hesaplama yeteneğine sahiptir. Zaman adımı, çözüm ağı ve bazı aerodinamik türevlerin (yunuslama sönümlemesi) etkileri HAD analizleri ve kod üzerinde incelenmiştir. Koddan elde edilen hıza, ağırlık merkezine ve kuyruk boyutuna bağlı sonuç matrisi, zamana bağlı öncelikle üç, daha sonrasında altı serbestlik derecesine sahip HAD analiz matrisi ile karşılaştırılmıştır. Elde edilen sonuçlara göre, aerodinamik gövde boylamasına durağan kararlılığa sahip olduğu sürece 3 serbestlik dereceli kod, incelenen analiz matrisindeki parametrelerin değişim eğilimlerini, aerodinamik gövdenin yörüngesini ve yunuslama açısındaki salınımları korunumlu bir şekilde yakalayabilmiştir. Bu sebeple yöntem, aerodinamik gövdenin ön tasarımını yapabilmek için yeterli bulunmuştur.

Anahtar kelimeler: Aerodinamik Gövde, Dikdörtgen Kesit Alanı, Ön Tasarım, 3 serbestlik dereceli, Uçuş Mekaniği, DatCOM, HAD (Hesaplamalı Akışkanlar Dinamiği), Fluent.

To my family...

To my love...

To my friends...

ACKNOWLEDGEMENTS

I would like to express my sincere gratitude to Prof. Dr. Yusuf Özyörük and Prof. Dr. Nafiz Alemdaroğlu for guiding this work. I want to state my special thanks to Prof. Dr. Yusuf Özyörük for his supervision, encouragement and patience during all steps in this work. I would also like to thank all committee members.

I owe my gratitude to Tahir Fidan for encouraging me to start my master thesis about this kind of topic as well as his guidance and friendship.

I wish to state my endless thanks to Serkan Kaymak and Ali Türker Kutay for their support on the flight mechanics of the problem. I would also like to thank Özgür Demir, Yusuf Okan Pekel and Mustafa Berispek for helping me in the computational fluid dynamics stages. I thank Sevinç Çalışkan and Serpil Gönenç Dinçer for their support throughout the thesis stages.

Thanks to my father Adil, my mother Yasemin and my sister Ecenaz as well as my girlfriend Ceren and my close friends for their smiling faces and endless support throughout my life.

I would also like to thank ASELSAN A.Ş for providing the necessary software and hardware for the analyses and TÜBİTAK M.Sc National Scholarship Programme for its financial support that has proved to be of so much use for especially the analysis pre-processing throughout the thesis.

TABLE OF CONTENTS

ABSTRACT v

ÖZ vii

ACKNOWLEDGEMENTS x

TABLE OF CONTENTS xi

LIST OF TABLES xiv

LIST OF FIGURES xv

LIST OF SYMBOLS xxiii

CHAPTERS

1. INTRODUCTION 1

  1.1 BACKGROUND 1

  1.2 OBJECTIVE OF THE THESIS 4

  1.3 SCOPE AND OUTLINE OF THE THESIS 4

2. THEORY AND NUMERICAL IMPLEMENTATION 7

  2.1 COORDINATE SYSTEMS 7

    2.1.1 Body-Fixed Coordinate System 7

    2.1.2 Vehicle Carried Frame of Reference 8

    2.1.3 Wind Frame of Reference 9

  2.2 COORDINATE SYSTEM TRANSFORMATIONS 10

    2.2.1 Vehicle Carried to Body Fixed Coordinate System Transformation ... 10

    2.2.2 Body-Fixed Coordinate System to Wind Axes Transformation 12

    2.2.3 Derivative of a Vector using the Theorem of Coriolis 12

2.3 A BODY IN 6DOF MOTION 13

2.4 THE 3DOF ASSUMPTION 16

2.5 AERODYNAMIC FORCES / MOMENTS ACTING ON THE BODY 20

2.6 NUMERICAL IMPLEMENTATION 22

2.6.1 Atmospheric Conditions Module 23

2.6.2 Geometric Calculations Module 24

2.6.3 Aerodynamic Data Table Lookup Module 26

2.6.4 Time Integration Module 28

3. CALCULATION OF AERODYNAMIC COEFFICIENTS 31

3.1 METHOD 1 – THE EMPIRICAL SOLUTION (DatCOM) 31

3.2 METHOD 2 – THE NUMERICAL SOLUTION 33

3.2.1 Governing Equations 33

3.2.2 Turbulence Modeling 34

3.2.3 Boundary Conditions 36

3.2.4 Solver Approaches And Discretization 36

3.2.5 Computational Grid Generation 37

3.3 METHODOLOGY COMPARISON 40

4. ASSESSMENT OF THE METHODOLOGY 45

4.1 NON-DIMENSIONAL QUANTITIES 45

4.2 TIME-STEP SELECTION 46

4.2.1 Time Step Selection for 3FL-DYN 46

4.2.2 Time Step Selection for Transient CFD Analyses 49

4.3 PITCH DAMPING TERM REQUIREMENT IN 3FL-DYN 51

4.3.1 Obtaining the Pitch Damping Term 52

4.3.2 Evaluating the Effect of Pitch Damping 54

4.4 GRID INDEPENDENCE 57
4.5 EVALUATION OF THE 3DOF ASSUMPTION 59
4.5.1 3DOF / 6DOF Solution Methodology 59
4.5.2 Comparison of 3DOF / 6DOF Motion 60
5. RESULTS AND DISCUSSIONS 67
5.1 ANALYSIS CONDITIONS 67
5.2 CENTER OF GRAVITY EFFECT 69
5.3 MACH NUMBER EFFECT 76
5.4 TAIL SIZE EFFECT 83
6. CONCLUSION AND FUTURE WORK 91
REFERENCES 93

APPENDICES

APPENDIX A. SUPPLEMENTARY RESULTS 95

LIST OF TABLES

TABLES

Table 1. Prism Layer Mesh Parameters 39

Table 2. The different grid sizes used for the grid independence study........ 57

Table 3. The analysis conditions........ 68

Table 4. The analysis matrix 69

LIST OF FIGURES

FIGURES

Figure 1. ChemRing Flare CM 218 K7 Type 1 CounterMeasure [2] 1

Figure 2. Utilization of Flare Countermeasure [3].. 2

Figure 3. Unsafe Seperation of a 600 Gallon Fuel Tank from F-111A Aircraft [4].... 2

Figure 4. The Body Coordinate System... 7

Figure 5. The Vehicle Carried Frame of Reference... 8

Figure 6. The Wind Frame of Reference 9

Figure 7. The Three Transformations and Euler Angles.. 10

Figure 8. Forces and Moments acting on the Decoy with respect to body axes 13

Figure 9. Forces and Moments acting on the Decoy with respect to inertial axes in 3DOF 20

Figure 10. The flowchart of 3FL-DYN.. 22

Figure 11. Center of Gravity Reference and Inertia Calculation 24

Figure 12. Recalculation of Moment Coefficient 27

Figure 13. Sample DatCOM Input File for MIG-17.. 32

Figure 14. The Surface Mesh Around the Nose Region of the Decoy (Grid #2) 38

Figure 15. The Surface Mesh Around the Tail Region of the Decoy (Grid #2) 38

Figure 16. The Surface Mesh Around the Domain.. 39

Figure 17. Overall Prism Layer Thickness Distribution Around the Decoy.............. 40

Figure 18. Comparison of drag coefficients calculated by two methodologies at M=0.3 41

Figure 19. Comparison of lift coefficients calculated by two methodologies at M=0.3 41

Figure 20. Comparison of pitching moment coefficients calculated by two methodologies at M=0.3 42

Figure 21. Comparison of drag coefficients calculated by two methodologies at M=0.6 42

Figure 22. Comparison of lift coefficients calculated by two methodologies at M=0.6 43

Figure 23. Comparison of pitching moment coefficients calculated by two methodologies at M=0.6 43

Figure 24. Non-dimensional Theta vs. Time at M = 0.3 for various timesteps utilized in 3FL-DYN 47

Figure 25. Non-dimensional $\boldsymbol{q}$ vs. Time at M = 0.3 for various timesteps utilized in 3FL-DYN 47

Figure 26. Non-dimensional Theta vs. Time at M = 0.6 for various timesteps utilized in 3FL-DYN 48

Figure 27. Non-dimensional $\boldsymbol{q}$ vs. Time at M = 0.6 for various timesteps utilized in 3FL-DYN 48

Figure 28. Non-dimensional Phi vs. Time at M = 0.6 for various timesteps utilized in transient 6DOF CFD 49

Figure 29. Non-dimensional Theta vs. Time at M = 0.6 for various timesteps utilized in transient 6DOF CFD 50

Figure 30. Non-dimensional Psi vs. Time at M = 0.6 for various timesteps utilized in transient 6DOF CFD 50

Figure 31. The outer domain solution mesh used for the interface boundary condition in FLUENT 53

Figure 32. Pitch Damping Coefficient $\boldsymbol{CM,q}$ vs. Angle of Attack at M = 0.3 54

Figure 33. Non-dimensional Theta vs. Time at M = 0.6 for the evaluation of the pitch damping term $\boldsymbol{CM,q}$ utilized in 3DOF numerical implementation 55

Figure 34. Non-dimensional $\boldsymbol{q}$ vs. Time at M = 0.6 for the evaluation of the pitch damping term $\boldsymbol{CM,q}$ utilized in 3DOF numerical implementation 55

Figure 35. Non-dimensional $\boldsymbol{q}$ vs. Time at M = 0.6 for the evaluation of the pitch damping term $\boldsymbol{CM,q}$ utilized in 3DOF numerical implementation 56

Figure 36. Drag coefficient comparison of four different grid sizes.......................... 58

Figure 37. Lift coefficient comparison of four different grid sizes........................... 58

Figure 38. Pitching moment coefficient comparison of four different grid sizes 58

Figure 39. Non-dimensional Theta vs. Time 3DOF / 6DOF comparison for M = 0.3, CG1 61

Figure 40. Non-dimensional Theta vs. Time 3DOF / 6DOF comparison for M = 0.6, CG1 61

Figure 41. Non-dimensional Theta vs. Time 3DOF / 6DOF comparison for M = 0.3, CG2 62

Figure 42. Non-dimensional Theta vs. Time 3DOF / 6DOF comparison for M = 0.6, CG2 62

Figure 43. Non-dimensional Phi vs. Time of 6DOF motion for M = 0.6, CG1 63

Figure 44. Non-dimensional Psi vs. Time of 6DOF motion for M = 0.6, CG1......... 64

Figure 45. Non-dimensional Phi vs. Time of 6DOF motion for M = 0.6, CG2 64

Figure 46. Non-dimensional Psi vs. Time of 6DOF motion for M = 0.6, CG2......... 65

Figure 47. Non-dimensional Theta vs. Time 3FL-DYN / 6DOF CFD comparison for M = 0.6, CG = 30%, Tail = 100%... 70

Figure 48. Non-dimensional Theta vs. Time 3FL-DYN / 6DOF CFD comparison for M = 0.6, CG = 10%, Tail = 100%... 70

Figure 49. 3FL-DYN Non-dimensional Theta vs. Time comparison of two center of gravity values for M = 0.6, Tail = 100%... 71

Figure 50. 6DOF CFD Non-dimensional Theta vs. Time comparison of two center of gravity values for M = 0.6, Tail = 100% 71

Figure 51. 6DOF CFD Non-dimensional Psi vs. Time comparison of two center of gravity values for M = 0.6, Tail = 100% 72

Figure 52. 3FL-DYN / 6DOF CFD Trajectory Comparison for M = 0.6, CG = 30%, Tail = 100% 73

Figure 53. 3FL-DYN / 6DOF CFD Trajectory Comparison for M = 0.6, CG = 10%, Tail = 100% 73

Figure 54. Motion history of the decoy at different time points with 10 non-dimensional time interval obtained from 6DOF CFD analyses colored with the pressure distribution around the decoy for two different center of gravity values for M = 0.6, Tail = 100% (CG = 10% : Left, CG = 30% Right) 75

Figure 55. Non-dimensional Theta vs. Time 3FL-DYN / 6DOF CFD comparison for M = 0.6, CG = 30%, Tail = 100% 76

Figure 56. Non-dimensional Theta vs. Time 3FL-DYN / 6DOF CFD comparison for M = 0.45, CG = 30%, Tail = 100% 77

Figure 57. Non-dimensional Theta vs. Time 3FL-DYN / 6DOF CFD comparison for M = 0.3, CG = 30%, Tail = 100% 77

Figure 58. 3FL-DYN Non-dimensional Theta vs. Time comparison of three Mach number values for CG = 30%, Tail = 100% 78

Figure 59. 6DOF CFD Non-dimensional Theta vs. Time comparison of three Mach number values for CG = 30%, Tail = 100% 78

Figure 60. 6DOF CFD Non-dimensional Psi vs. Time comparison of three Mach number values for CG = 30%, Tail = 100% 79

Figure 61. 3FL-DYN / 6DOF CFD Trajectory Comparison for M = 0.6, CG = 30%, Tail = 100% 80

Figure 62. 3FL-DYN / 6DOF CFD Trajectory Comparison for M = 0.45, CG = 30%, Tail = 100% 80

Figure 63. 3FL-DYN / 6DOF CFD Trajectory Comparison for M = 0.3, CG = 30%, Tail = 100% 81

Figure 64. Mach Number distribution around the decoy at different time points a, b, c, d with 20 non-dimensional time interval obtained from 6DOF CFD analyses for three different Mach Number values for CG = 30%, Tail = 100% 82

Figure 65. Non-dimensional Theta vs. Time 3FL-DYN / 6DOF CFD comparison for M = 0.6, CG = 30%, Tail = 100% 83

Figure 66. Non-dimensional Theta vs. Time 3FL-DYN / 6DOF CFD comparison for M = 0.6, CG = 30%, Tail = 80% 84

Figure 67. 3FL-DYN Non-dimensional Theta vs. Time comparison of two tail size values for M = 0.6, CG = 30% 84

Figure 68. 6DOF CFD Non-dimensional Theta vs. Time comparison of two tail size values for M = 0.6, CG = 30% 85

Figure 69. Pressure distribution on the tail section of the decoy for two different tail sizes at initial time step (Tail = 100% : Left, Tail = 80% Right) 86

Figure 70. 6DOF CFD Non-dimensional Psi vs. Time comparison of two tail size values for M = 0.6, CG = 30% 86

Figure 71. 3FL-DYN / 6DOF CFD Trajectory Comparison for M = 0.6, CG = 30%, Tail = 100% 87

Figure 72. 3FL-DYN / 6DOF CFD Trajectory Comparison for M = 0.6, CG = 30%, Tail = 80% 88

Figure 73. Motion history of the decoy at different time points with 10% time interval obtained from 6DOF CFD analyses colored with the pressure distribution around the decoy for two different tail size values for M = 0.6, CG = 30% (Tail = 100% : Left, Tail = 80% Right) 89

Figure 74. 6DOF CFD Non-dimensional Phi vs. Time comparison of two center of gravity values for M = 0.6, Tail = 100% 95

Figure 75. 6DOF CFD Non-dimensional Phi vs. Time comparison of three Mach numbers for CG = 30%, Tail = 100% 96

Figure 76. 6DOF CFD Non-dimensional Phi vs. Time comparison of two tail sizes for M = 0.6, CG = 30% 96

Figure 77. Non-dimensional Theta vs. Time 3FL-DYN / 6DOF CFD comparison for M = 0.3, CG = 10%, Tail = 80% 97

Figure 78. 3FL-DYN / 6DOF CFD Trajectory Comparison for M = 0.3, CG = 10%, Tail = 80% 97

Figure 79. 6DOF CFD Non-dimensional Psi vs. Time for M = 0.3, CG = 10%, Tail = 80% 97

Figure 80. Non-dimensional Theta vs. Time 3FL-DYN / 6DOF CFD comparison for M = 0.45, CG = 10%, Tail = 80% 98

Figure 81. 3FL-DYN / 6DOF CFD Trajectory Comparison for M = 0.45, CG = 10%, Tail = 80% 98

Figure 82. 6DOF CFD Non-dimensional Psi vs. Time for M = 0.45, CG = 10%, Tail = 80% 98

Figure 83. Non-dimensional Theta vs. Time 3FL-DYN / 6DOF CFD comparison for M = 0.6, CG = 10%, Tail = 80% 99

Figure 84. 3FL-DYN / 6DOF CFD Trajectory Comparison for M = 0.6, CG = 10%, Tail = 80% 99

Figure 85. 6DOF CFD Non-dimensional Psi vs. Time for M = 0.6, CG = 10%, Tail = 80% 99

Figure 86. Non-dimensional Theta vs. Time 3FL-DYN / 6DOF CFD comparison for M = 0.3, CG = 30%, Tail = 80% 100

Figure 87. 3FL-DYN / 6DOF CFD Trajectory Comparison for M = 0.3, CG = 30%, Tail = 80% 100

Figure 88. 6DOF CFD Non-dimensional Psi vs. Time for M = 0.3, CG = 30%, Tail = 80% 100

Figure 89. Non-dimensional Theta vs. Time 3FL-DYN / 6DOF CFD comparison for M = 0.45, CG = 30%, Tail = 80% 101

Figure 90. 3FL-DYN / 6DOF CFD Trajectory Comparison for M = 0.45, CG = 30%, Tail = 80% 101

Figure 91. 6DOF CFD Non-dimensional Psi vs. Time for M = 0.45, CG = 30%, Tail = 80% 101

Figure 92. Non-dimensional Theta vs. Time 3FL-DYN / 6DOF CFD comparison for M = 0.6, CG = 30%, Tail = 80% 102

Figure 93. 3FL-DYN / 6DOF CFD Trajectory Comparison for M = 0.6, CG = 30%, Tail = 80% 102

Figure 94. 6DOF CFD Non-dimensional Psi vs. Time for M = 0.6, CG = 30%, Tail = 80% 102

Figure 95. Non-dimensional Theta vs. Time 3FL-DYN / 6DOF CFD comparison for M = 0.3, CG = 10%, Tail = 100% 103

Figure 96. 3FL-DYN / 6DOF CFD Trajectory Comparison for M = 0.3, CG = 10%, Tail = 100% 103

Figure 97. 6DOF CFD Non-dimensional Psi vs. Time for M = 0.3, CG = 10%, Tail = 100% 103

Figure 98. Non-dimensional Theta vs. Time 3FL-DYN / 6DOF CFD comparison for M = 0.45, CG = 10%, Tail = 100% 104

Figure 99. 3FL-DYN / 6DOF CFD Trajectory Comparison for M = 0.45, CG = 10%, Tail = 100% 104

Figure 100. 6DOF CFD Non-dimensional Psi vs. Time for M = 0.45, CG = 10%, Tail = 100% 104

Figure 101. Non-dimensional Theta vs. Time 3FL-DYN / 6DOF CFD comparison for M = 0.6, CG = 10%, Tail = 100% 105

Figure 102. 3FL-DYN / 6DOF CFD Trajectory Comparison for M = 0.6, CG = 10%, Tail = 100% 105

Figure 103. 6DOF CFD Non-dimensional Psi vs. Time for M = 0.6, CG = 10%, Tail = 100% 105

Figure 104. Non-dimensional Theta vs. Time 3FL-DYN / 6DOF CFD comparison for M = 0.3, CG = 30%, Tail = 100% 106

Figure 105. 3FL-DYN / 6DOF CFD Trajectory Comparison for M = 0.3, CG = 30%, Tail = 100% 106

Figure 106. 6DOF CFD Non-dimensional Psi vs. Time for M = 0.3, CG = 30%, Tail = 100% 106

Figure 107. Non-dimensional Theta vs. Time 3FL-DYN / 6DOF CFD comparison for M = 0.45, CG = 30%, Tail = 100% 107

Figure 108. 3FL-DYN / 6DOF CFD Trajectory Comparison for M = 0.45, CG = 30%, Tail = 100% 107

Figure 109. 6DOF CFD Non-dimensional Psi vs. Time for M = 0.45, CG = 30%, Tail = 100% 107

Figure 110. Non-dimensional Theta vs. Time 3FL-DYN / 6DOF CFD comparison for M = 0.6, CG = 30%, Tail = 100% 108

Figure 111. 3FL-DYN / 6DOF CFD Trajectory Comparison for M = 0.6, CG = 30%, Tail = 100% 108

Figure 112. 6DOF CFD Non-dimensional Psi vs. Time for M = 0.6, CG = 30%, Tail = 100% 108

LIST OF SYMBOLS

x	x-coordinate
y	y-coordinate
z	z-coordinate
t	Time
X	Force on x-axis
Y	Force on y-axis
Z	Force on z-axis
α	Angle of attack
β	Angle of sideslip
V	Velocity
ϕ	Roll angle
θ	Pitch angle
ψ	Yaw angle
u	Velocity on body x-axis
v	Velocity on body y-axis
w	Velocity on body z-axis
p	Roll rate on body x-axis

q	Pitching rate on body y-axis
r	Yaw rate on body z-axis
ω	Angular velocity
γ	Ratio of specific heats
P	Pressure
T	Temperature
C_D	Drag Coefficient
C_L	Lift Coefficient
C_M	Moment Coefficient
$C_{M,q}$	Derivative of moment coefficient with respect to pitching rate
l	Length
S_{ref}	Reference area
L_h	Temperature lapse rate
h_{ALT}	Pressure altitude
ρ	Density
m	Mass
k	Thermal conductivity
τ	Shear stress

CHAPTER 1

INTRODUCTION

1.1 BACKGROUND

A decoy is defined as “something designed to deceive an enemy or divert its attention”. [1] For military aviation purposes, decoys are generally utilized as countermeasures such as flares (Figure 1) for protection against infrared-homing missiles or countermeasures that deploys electronic warfare methods to deceive radar-guided missiles. These decoys produce a more favorable target for the missile to track; higher infrared emission etc., thus protecting the aircraft. (Figure 2) As they are expendable, the decoys generally do not have control infrastructures, but some have stabilizing surfaces due to initial high angle of attack values they are exposed to.

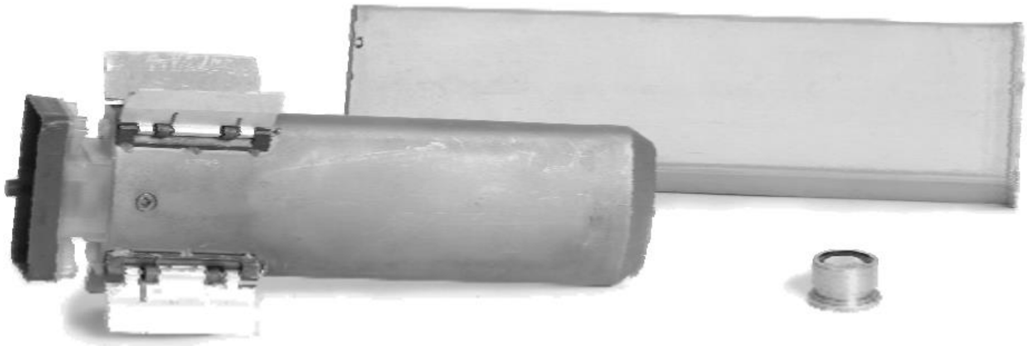

Figure 1. ChemRing Flare CM 218 K7 Type 1 CounterMeasure [2]

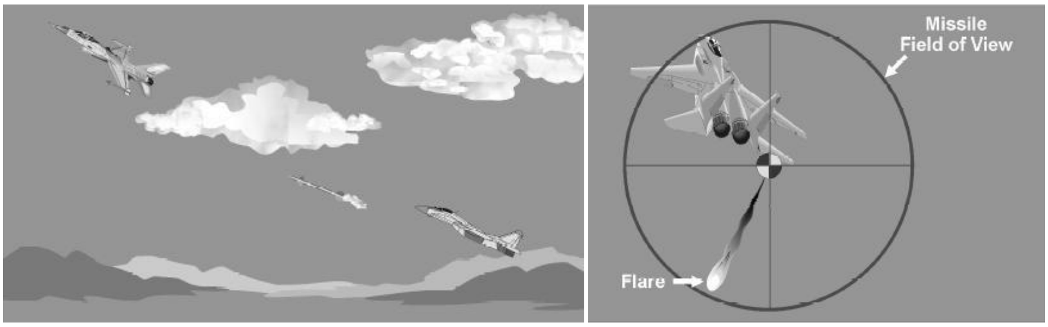

Figure 2. Utilization of Flare Countermeasure [3]

Whenever a decoy is released in flight, there are basically two requirements for the decoy to satisfy: safe separation from the aircraft and effectiveness, which is the ability to deceive the threat. These two requirements should be investigated in detail.

Safe separation is always a requirement for any store (a bomb, rocket, fuel tank, electronic warfare pod, decoy etc.) which is released from an aircraft during flight. Otherwise, flight safety might be at risk due to a damaged crucial aerodynamic surface or an aircraft system. Essentially, the decoy should not collide with the aircraft. As an example, Figure 3 shows the seperation of a 600 gallon fuel tank on an F-111A aircraft, which was not able to satisfy the safe separation requirement resulting in the loss of the right horizontal tail. [4]

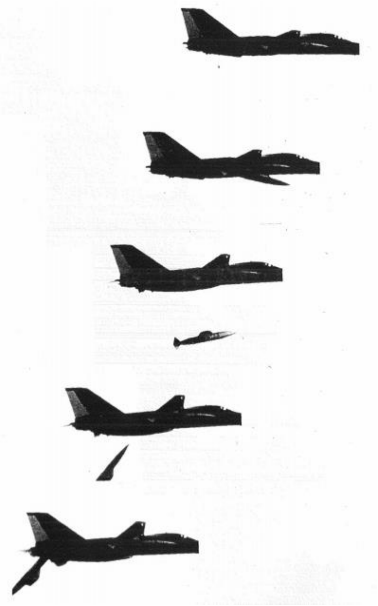

Figure 3. Unsafe Seperation of a 600 Gallon Fuel Tank from F-111A Aircraft [4]

The ability of the decoy to deceive the threat depends not only on the effectiveness of the methods it employs, but also the flight path of the aircraft as well as that of the decoy. Today, some seekers have algorithms which may be able to notice the differences between the horizontal speed of the aircraft and the decoy, with the help of Doppler effect like a Police radar. [5] For instance, if a decoy’s flight path is perpendicular to the flight path of an aircraft, the seeker may be able to understand the impossibility of the aircraft to suddenly decrease its speed in a very short amount of time thus making the decoy ineffective. In order to remedy this situation, the decoy should be able to mimic the flight path of the aircraft just long enough to deceive the threat. In addition, if the decoy is an electronic countermeasure, due to the placement of antennas and such, the orientation of the decoy is going to be crucial.

From the aerodynamics point of view of such decoys, the design process can be problematic. In order to satisfy the two basic requirements mentioned above, the aerodynamic loads, moments acting on the decoy and the aerodynamic derivatives of the decoy both in the carriage and after release phase should be known in all directions. This is due to the fact that the decoy is actually a six-degree-of-freedom (6DOF) system. Besides the decoy itself, the attitude history of the aircraft should be known. This includes the maneuvering (level turn, pushdown etc.), hence the position, orientation and the flowfield, along with the flight conditions (altitude, flow regime) and the ejector forces and moments. Therefore, a huge matrix of separation conditions awaits the aerodynamic designer of the decoy.

In order to design such a decoy, the designer needs such a full set of aerodynamic data for the decoy and the aircraft. This set includes the forces and moments acting on the decoy at different Mach numbers, angles of attack, angles of sideslip as well as the aerodynamic derivatives like the pitch, yaw, roll damping and stiffness at different angular rates and accelerations. The designer might obtain this set by means of computational fluid dynamics analyses (CFD), wind tunnel testing or flight testing. However, before spending a big effort on obtaining the set of aerodynamic data needed, a problem emerges. The design process is iterative. Hence, there should be an initial design of the decoy to begin the iteration process, as wind tunnel and flight testing would be time-consuming and costly for an initial design. Although, CFD analyses are time-consuming and costly as well, compared to testing, they are still cheaper for an initial design approach.

1.2 OBJECTIVE OF THE THESIS

As a consequence of the above discussions, it may be concluded that the designer needs a fast initial design tool to begin this iterative design process. The goal is to develop and validate a fast and cheap initial aerodynamic design methodology for a decoy. The methodology basically consists of the numerical integration of 3-degree-of-freedom (3DOF) flight equations in a quasi-steady manner. These equations model the aerodynamics of the decoy with the help of tabulated aerodynamic data. The methodology is validated by comparing the results obtained with transient 6-degree-of-freedom CFD results, in terms of trajectory, orientation and time-history of the decoy. The flowfield of CFD results are investigated as well. During the validation phase, the code results are not expected to be identical to the 6DOF transient CFD results, they are just expected to capture the physics of the problem.

1.3 SCOPE AND OUTLINE OF THE THESIS

This study is divided into six chapters. Chapter 1 gives some background information about decoys as well as the design methodology of a decoy. In Chapter 2, the theoretical background of flight mechanics as well as the workflow and the development of the numerical implementation is explained. In Chapter 3, the aerodynamic coefficients obtained from different calculation methods are compared. In Chapter 4, an assessment of the design methodology is presented, which involves numerical work on grid independence and time step selection for both the numerical implementation and the transient CFD analyses. Also, it includes the addition of an aerodynamic derivative to the numerical implementation as well as comparisons of transient 3DOF and 6DOF CFD analyses with these additional terms as an evaluation of 3DOF assumption. In Chapter 5, the results obtained from transient CFD analyses and the 3DOF methodology are compared and discussed thoroughly to validate the approach in this study; while Chapter 6 consists of conclusion remarks and possible future work.

CHAPTER 2

THEORY AND NUMERICAL IMPLEMENTATION

In this chapter, the flight mechanics theory of an object in 6DOF flight, the reduction of 6DOF equations to 3DOF equations and the numerical implementation of 3DOF equations are discussed. The axes systems are shown on a generic geometry with circular cross-section.

2.1 COORDINATE SYSTEMS

2.1.1 Body-Fixed Coordinate System

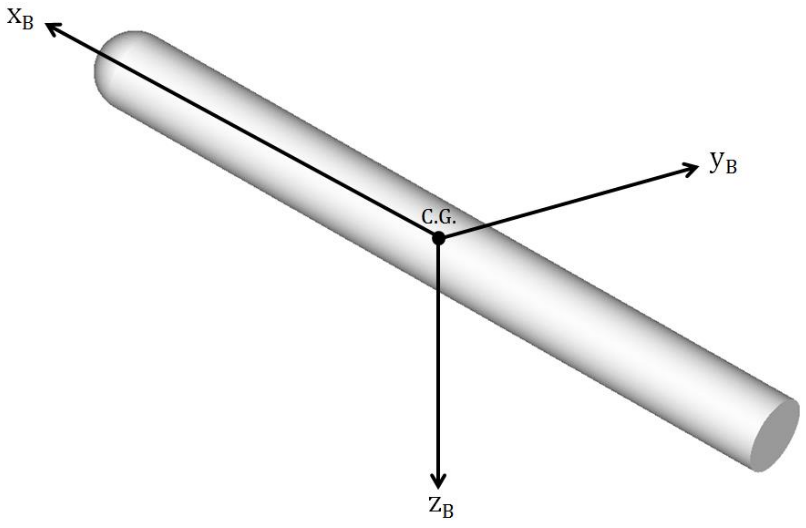

Figure 4. The Body Coordinate System

Body coordinate system translates and rotates with the aircraft and is denoted by the subscript “B”. In this coordinate system, x_B-axis points towards the nose and y_B-axis points towards the right side of the aircraft while the z_B-axis forms a right hand rule as illustrated in Figure 4. The origin of the coordinate system is the center of gravity (c.g.) of the aircraft. x_B-axis is the roll, y_B-axis is the pitch and z_B-axis is the yaw axis of the aircraft. [6]

2.1.2 Vehicle Carried Frame of Reference

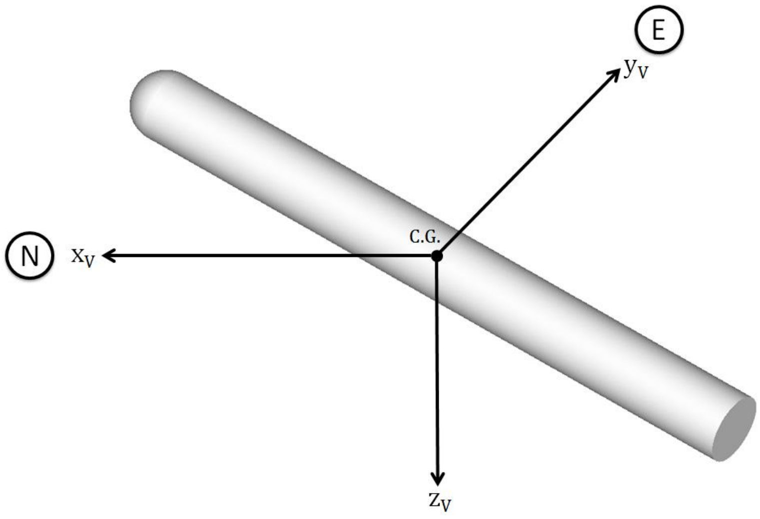

Figure 5. The Vehicle Carried Frame of Reference

This coordinate system is an “inertial coordinate system” which basically means that a linear accelerometer or a rate gyro would detect zero linear or angular acceleration if they were moving with the inertial coordinate system. Newton’s laws of motion is only valid if they are written in an inertial coordinate system. [6]

Different from the body fixed coordinate system, the vehicle carried coordinate system does not rotate with the aircraft; though it translates with the aircraft. It is denoted by the subscript “V”. The origin of the coordinate system is the center of gravity of the aircraft. The x_V-axis points towards North (N), y_V-axis points towards East (E) and z_V-axis is along the gravity direction as can be seen from Figure 5. [7]

For ease, the direction of flight is always towards North in this study.

2.1.3 Wind Frame of Reference

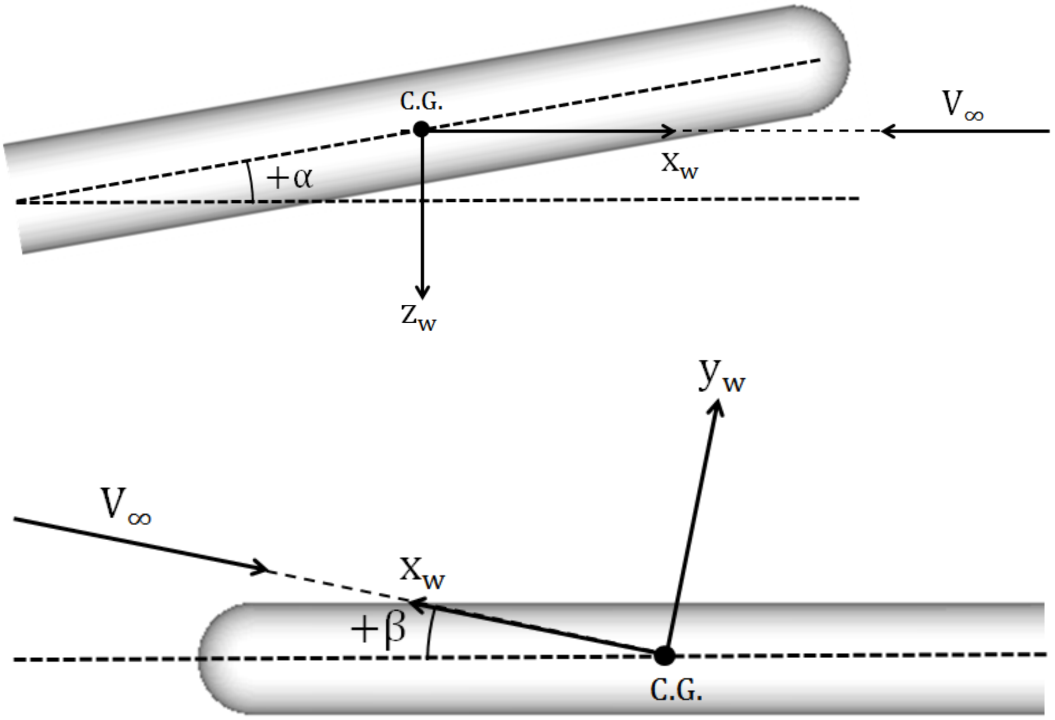

Figure 6. The Wind Frame of Reference

This coordinate system is derived from the local air around the aircraft. It is denoted by the subscript “w”. The origin of the coordinate system is the center of gravity of the aircraft. The x_w-axis points towards the local vehicle relative atmospheric movement, z_w-axis is perpendicular to x_w-axis and in the symmetry plane of the aircraft, while the y_w-axis forms a right-handed rule as can be seen from Figure 6. [6]

2.2 COORDINATE SYSTEM TRANSFORMATIONS

Any coordinate system can be transformed into one another, with the help of a sequence of three rotations with three different angles.

2.2.1 Vehicle Carried to Body Fixed Coordinate System Transformation

During the transformation of the vehicle carried coordinate system to the body fixed coordinate system, the angles are defined as the *"Euler angles"*, if the transformation is initiated about the z_v-axis and continued with the new y_1-axis and x_2-axis respectively. The angle about the z_v-axis transformation is defined as the "yaw", y_1-axis transformation is the "pitch" and x_2-axis transformation is the "roll" angle. Figure 7 shows the Euler angles and the defined transformations. [6]

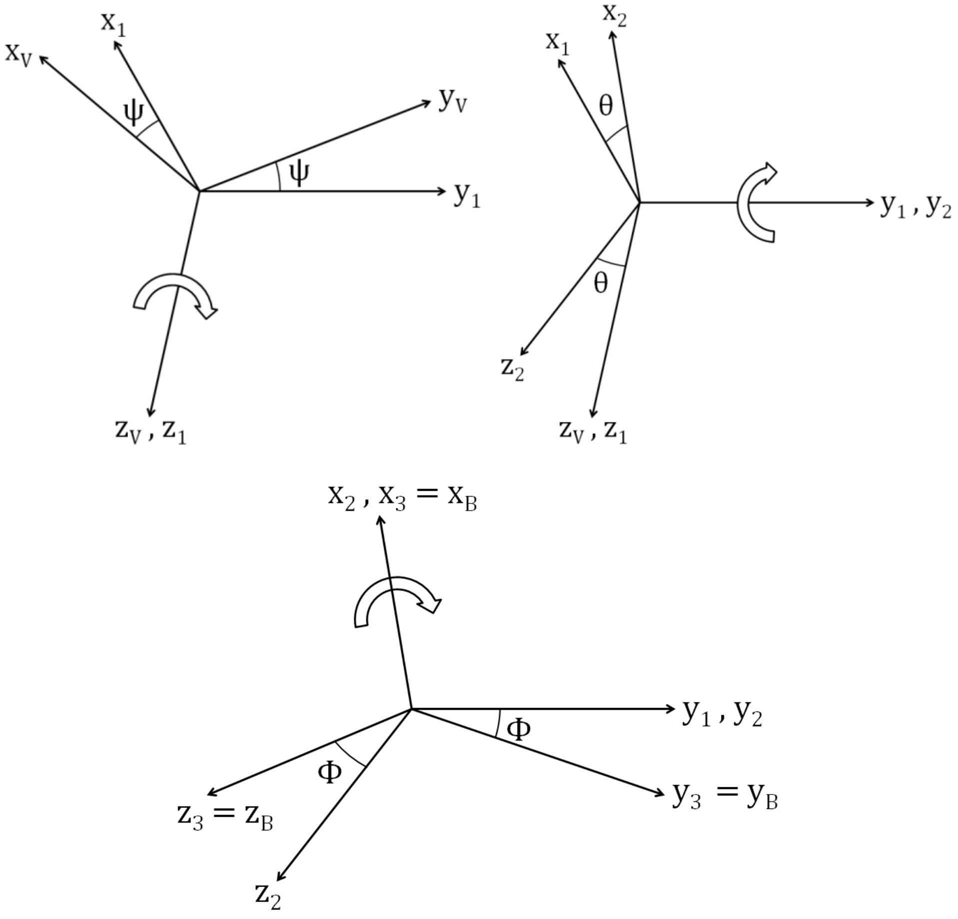

Figure 7. The Three Transformations and Euler Angles

For instance, for the transformation around the z_V-axis (first transformation), the following equations can be written:

$$z_1 = z_V \tag{1}$$

$$y_1 = y_V \cos(\psi) - x_V \sin(\psi) \tag{2}$$

$$x_1 = y_V \sin(\psi) + x_V \cos(\psi) \tag{3}$$

which basically means that in order to make a transformation around the z-axis, the following transformation matrix can be written as:

$$R = \begin{bmatrix} \cos\psi & \sin\psi & 0 \\ -\sin\psi & \cos\psi & 0 \\ 0 & 0 & 1 \end{bmatrix} \tag{4}$$

If the transformation matrices are written for all of directions and multiplied together:

$$\begin{bmatrix} x_B \\ y_B \\ z_B \end{bmatrix} = \begin{bmatrix} 1 & 0 & 0 \\ 0 & \cos\phi & \sin\phi \\ 0 & -\sin\phi & \cos\phi \end{bmatrix} \begin{bmatrix} \cos\theta & 0 & -\sin\theta \\ 0 & 1 & 0 \\ \sin\theta & 0 & \cos\theta \end{bmatrix} \begin{bmatrix} \cos\psi & \sin\psi & 0 \\ -\sin\psi & \cos\psi & 0 \\ 0 & 0 & 1 \end{bmatrix} \begin{bmatrix} x_V \\ y_V \\ z_V \end{bmatrix} \tag{5}$$

Then the transformation can be denoted as:

$$\begin{bmatrix} x_B \\ y_B \\ z_B \end{bmatrix} = L_{VB} \begin{bmatrix} x_V \\ y_V \\ z_V \end{bmatrix} \tag{6}$$

For the inverse transformation, which is from the vehicle carried coordinate system to the body coordinate system, the following statement can be used:

$$\begin{bmatrix} x_V \\ y_V \\ z_V \end{bmatrix} = {L_{VB}}^{-1} \begin{bmatrix} x_B \\ y_B \\ z_B \end{bmatrix} \tag{7}$$

2.2.2 Body-Fixed Coordinate System to Wind Axes Transformation

Wind Axis coordinate system has one of the axes defined in the plane of symmetry of the aircraft. There is no rotation around the x_w-axis of the wind axis coordinate system. The drag force is along the x_w-axis with negative direction, the lift force is along the z_w-axis with negative direction, while the aerodynamic pitching moment is along the y-axis with a positive direction. Hence, there are only two angles defined for the wind axis coordinate system which are the angle of attack (α) and the angle of sideslip (β). Due to the positive sign convention of the angle of sideslip (Figure 6), the transformation is done with the negative sign of angle of sideslip. Applying the same method discussed in the section above, the transformation matrix is found out to be:

$$\begin{bmatrix} x_W \\ y_W \\ z_W \end{bmatrix} = \begin{bmatrix} cos\,\alpha\,cos\,\beta & -\,cos\,\alpha\,sin\,\beta & -\,sin\,\alpha \\ -\,sin\,\beta & cos\,\beta & 0 \\ sin\,\alpha\,cos\,\beta & -\,sin\,\alpha\,sin\,\beta & cos\,\alpha \end{bmatrix} \begin{bmatrix} x_B \\ y_B \\ z_B \end{bmatrix} \tag{8}$$

2.2.3 Derivative of a Vector using the Theorem of Coriolis

When the derivative of a vector is written as components of a rotating frame (body-fixed) with respect to a non-rotating frame (vehicle-carried, inertial), the theorem of coriolis should be applied. For the derivative of vector $\vec{V}$ defined in an inertial coordinate system with respect to time, the theorem is written as:

$$\left.\frac{d\vec{V}}{dt}\right|_I = \left.\frac{d\vec{V}}{dt}\right|_B + \overrightarrow{\omega_B} \times \overrightarrow{V_B} \tag{9}$$

where $\overrightarrow{\omega_B}$ is the angular velocity of the rotating coordinate system (body-fixed) with respect to the non-rotating frame. (vehicle-carried)

In order to find the relation of the body angular rates ($\overrightarrow{\omega_B}$) with Euler angular rates ($\overrightarrow{\omega_V}$), a transformation is required. When the transformation is done from body-fixed coordinate system to the vehicle carried coordinate system according to the same order defined above, of the three transformations the last one is not necessary. This is due to the fact that at the last transformation, the x-axis, at which the rates are being measured in two coordinate systems, are aligned; so that the values of the angular rates are the same. When the transformation is done according to the necessary two axes, the result is as follows:

$$\overrightarrow{\omega_B} = \begin{bmatrix} p \\ q \\ r \end{bmatrix} = \begin{bmatrix} 1 & 0 & -\sin\theta \\ 0 & \cos\phi & \sin\phi\cos\theta \\ 0 & -\sin\phi & \cos\phi\cos\theta \end{bmatrix} \overrightarrow{\omega_V} = \begin{bmatrix} 1 & 0 & -\sin\theta \\ 0 & \cos\phi & \sin\phi\cos\theta \\ 0 & -\sin\phi & \cos\phi\cos\theta \end{bmatrix} \begin{bmatrix} \dot{\phi} \\ \dot{\theta} \\ \dot{\psi} \end{bmatrix} \quad (10)$$

The inverse transformation, then, is found out to be:

$$\begin{bmatrix} \dot{\phi} \\ \dot{\theta} \\ \dot{\psi} \end{bmatrix} = \begin{bmatrix} 1 & \sin\phi\tan\theta & \cos\phi\tan\theta \\ 0 & \cos\phi & -\sin\phi \\ 0 & \sin\phi\sec\theta & \cos\phi\sec\theta \end{bmatrix} \begin{bmatrix} p \\ q \\ r \end{bmatrix} \quad (11)$$

2.3 A BODY IN 6DOF MOTION

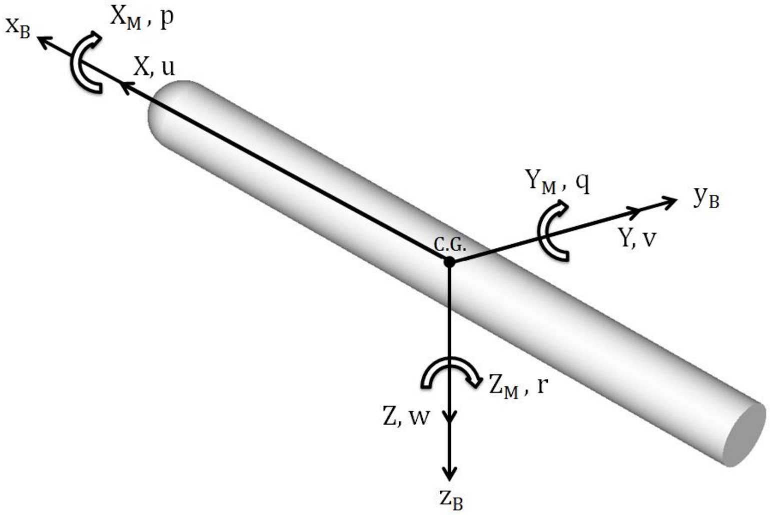

Figure 8. Forces and Moments acting on the Decoy with respect to body axes

When a body is in motion, Newton's 2nd Law of Motion should be satisfied, which is written for forces and moments separately:

$$\sum \vec{F} = m\vec{a} = m\left.\frac{d\vec{V}}{dt}\right|_I = m\left(\left.\frac{d\vec{V}}{dt}\right|_B + \overrightarrow{\omega_B} \times \overrightarrow{V_B}\right) \quad (12)$$

$$\sum \vec{G} = \left.\frac{d\vec{H}}{dt}\right|_I = \left.\frac{d\vec{H}}{dt}\right|_B + \overrightarrow{\omega_B} \times \overrightarrow{H_B} \tag{13}$$

In this representation, the linear accelerations are given in a straightforward manner; while the angular accelerations are given as the time derivative of the angular momentum $\vec{H}$. Also, the derivatives written according to the inertial coordinate systems are expanded as well. [6]

For the forces acting on the body, as can be seen from Figure 8, given that the components of the vectors are written in the body-fixed coordinate system:

$$\overrightarrow{F_B} = \begin{bmatrix} X \\ Y \\ Z \end{bmatrix} \tag{14}$$

$$\sum \vec{F} = \overrightarrow{F_B} + L_{BV} \begin{bmatrix} 0 \\ 0 \\ mg \end{bmatrix} \tag{15}$$

$$\overrightarrow{V_B} = \begin{bmatrix} u \\ v \\ w \end{bmatrix} \tag{16}$$

$$\left.\frac{d\vec{V}}{dt}\right|_B = \begin{bmatrix} \dot{u} \\ \dot{v} \\ \dot{w} \end{bmatrix} \tag{17}$$

The 2nd Law of Motion can be written as:

$$\sum \vec{F} = \begin{bmatrix} X \\ Y \\ Z \end{bmatrix} + L_{BV} \begin{bmatrix} 0 \\ 0 \\ mg \end{bmatrix} = m \left\{ \begin{bmatrix} \dot{u} \\ \dot{v} \\ \dot{w} \end{bmatrix} + \begin{bmatrix} p \\ q \\ r \end{bmatrix} \times \begin{bmatrix} u \\ v \\ w \end{bmatrix} \right\} \tag{18}$$

Expanding the equation and rearranging:

$$\dot{u} = rv - qw + \frac{X}{m} - g \sin\theta \tag{19}$$

$$\dot{v} = pw - ru + \frac{Y}{m} + g \sin\phi \cos\theta \tag{20}$$

$$\dot{w} = qu - pv + \frac{Z}{m} + g\,cos\,\phi\,cos\,\theta \tag{21}$$

For the moments acting on the body, as can be seen from Figure 8, given that the components of the vectors are written in the body-fixed coordinate system:

$$\sum \vec{G} = \begin{bmatrix} X_m \\ Y_m \\ Z_m \end{bmatrix} \tag{22}$$

$$\overrightarrow{H_B} = [I_B]\,\overrightarrow{\omega_B} \tag{23}$$

where I_B is the inertia matrix denoted as:

$$I_B = \begin{bmatrix} I_{xx} & -I_{xy} & -I_{xz} \\ -I_{xy} & I_{yy} & -I_{yz} \\ -I_{xz} & -I_{yz} & I_{zz} \end{bmatrix} \tag{24}$$

where:

$$I_{xx} = \int (y^2 + z^2)\,dm \tag{25}$$

$$I_{yy} = \int (x^2 + z^2)\,dm \tag{26}$$

$$I_{zz} = \int (x^2 + y^2)\,dm \tag{27}$$

$$I_{xy} = \int (xy)\,dm \tag{28}$$

$$I_{yz} = \int (yz)\,dm \tag{29}$$

$$I_{xz} = \int (xz)\,dm \tag{30}$$

It is clear that the inertia matrix is going to change with respect to an inertial coordinate system due to the fact that the mass distribution is going to change when the body rotates. Hence, the inertia matrix should be based on a coordinate system which is rotating and translating with the aircraft which is the body-fixed coordinate system. The reason behind the presentation of Newton's 2nd Law of Motion with the body fixed coordinate system is the difficulty of calculating the mass moment of inertia matrix with an inertial coordinate system. With this information on mind, expanding the 2nd Law of Motion for the moments:

$$\left.\frac{d\vec{H}}{dt}\right|_B = \frac{dI_B}{dt}\overrightarrow{\omega_B} + I_B\frac{d\overrightarrow{\omega_B}}{dt} \tag{31}$$

As the inertia of the decoy does not change with time, dI_B/dt term is zero, resulting in:

$$\sum\vec{G} = \begin{bmatrix} X_m \\ Y_m \\ Z_m \end{bmatrix} = \left.\frac{d\vec{H}}{dt}\right|_B + \overrightarrow{\omega_B} \times \overrightarrow{H_B} = I_B\frac{d\overrightarrow{\omega_B}}{dt} + \begin{bmatrix} p \\ q \\ r \end{bmatrix} \times \left[I_B \begin{bmatrix} p \\ q \\ r \end{bmatrix} \right] \tag{32}$$

where:

$$\frac{d\overrightarrow{\omega_B}}{dt} = \begin{bmatrix} \dot{p} \\ \dot{q} \\ \dot{r} \end{bmatrix} \tag{33}$$

2.4 THE 3DOF ASSUMPTION

As the decoy is released during flight, the dynamics of the problem should be resolved in six-degrees-of-freedom due to the fact that when an aircraft is in flight, it might be in a level flight or in a climbing or a maneuvering flight condition. This means that it might have any arbitrary orientations and all of the translational and rotational components of accelerations and velocities may be involved. A three-degrees-of-freedom dynamics model of a decoy is not going to be able to cover all of the components, but as explained before there is a need for a fast, cheap initial estimation tool. A 3DOF dynamics model requires less effort as there is only need for the aerodynamic data of a three-dimensional model of a decoy in two-dimensions.

There are applications of making a 3DOF assumption to reduce the calculation time required to find the aerodynamic coefficients as well as the time required for the solution of the dynamics of the model. For instance, Brochu et. al [9] developed and compared a 3DOF missile model,which eliminates the moments on the missile, with a high fidelity 6DOF model. The missile was a generic DND AIM-7 air-to-air missile which had autopilot control. They found out that the calculation time is about 1.7 times faster than the 6DOF model. The error for maximum range envelope calculations, which was the main purpose of the study, was 12% for 15km of altitude.

During most of the flight, the aircraft is going to be in a trimmed level flight condition which means that sum of all of the forces and moments acting on the aircraft is zero. The heading, altitude and attitude of the aircraft are constant. If the decoy were to be released during such a flight condition, as long as there were no lateral perturbations in the flow around the decoy and the decoy is symmetrical in the lateral direction, <u>ideally</u> the decoy should have no motion on the lateral directions. Hence, the decoy should move strictly in the longitudinal direction eliminating the two rotational and one translational degree-of-freedoms, resulting in a three-degrees-of-freedom motion. Of course, this is a strictly ideal case. The flowfield around the decoy most definitely is going to have lateral perturbations and the aircraft is going to be oscillating around both the longitudinal and rotational directions during flight affecting the release of the decoy. The strict movement of the decoy in longitudinal direction is only an assumption, a starting point.

The three-degree-of-freedom assumption basically restricts the motion of the body into two dimensions with three dimensional forces and pitching moment. In this study, the body is limited to travel in the longitudinal directions implying that there are no lateral movement or rotation both initially and during the motion. In other words, the body is limited to travel in forward-backward (x) and upward-downward (z) direction and rotate around pitch axis in vehicle carried coordinate system. For ease, the direction of flight is always towards North in this thesis.

With these limitations, it is understood that:

$$\begin{gathered} v = 0 \\ p = 0 \\ r = 0 \\ \dot{v} = 0 \\ \dot{p} = 0 \\ \dot{r} = 0 \\ \phi = 0 \\ \psi = 0 \\ Y = 0 \\ X_m = 0 \\ Z_m = 0 \end{gathered} \tag{34}$$

Applying these conditions to the translational and rotational equations of motion and given that the mass and the inertia of the decoy is constant throughout the whole motion, three equations are obtained:

$$\dot{u} = -qw + \frac{X}{m} - g \sin\theta \tag{35}$$

$$\dot{w} = qu + \frac{Z}{m} + g \cos\theta \tag{36}$$

$$\dot{q} = \frac{Y_m}{I_{yy}} \tag{37}$$

Examining these equations, it is seen that there is only one mass moment of inertia value required, which is the pitch moment of inertia. Given that there is no lateral motion, pitch moment of inertia is only dependent on the center of gravity location of the decoy, hence actually there is no need to write the equations of motion in the body axes. To be explained in Section 4.5.1, the flow solver utilizes an inertial frame of reference while calculating the motion of the decoy. The output is also given in this particular frame as well. In order to avoid another transformation from body axes to an inertial frame of reference, the equations of motion written in the vehicle carried coordinate system are used in this study. In order to transform these equations to vehicle carried coordinate system, firstly the terms emerging from the coriolis theorem should be eliminated. This is done according to:

$$\left.\frac{d\vec{V}}{dt}\right|_I = \left.\frac{d\vec{V}}{dt}\right|_B + \overrightarrow{\omega_B} \times \overrightarrow{V_B} \tag{38}$$

$$\left.\frac{d\vec{V}}{dt}\right|_I = \begin{bmatrix}\ddot{x}\\ \ddot{y}\\ \ddot{z}\end{bmatrix} = \left.\frac{d\vec{V}}{dt}\right|_B + \overrightarrow{\omega_B} \times \overrightarrow{V_B} = \begin{bmatrix}\dot{u}\\ \dot{v}\\ \dot{w}\end{bmatrix} + \begin{bmatrix}p\\ q\\ r\end{bmatrix} \times \begin{bmatrix}u\\ v\\ w\end{bmatrix} \tag{39}$$

Eliminating the lateral terms due to the 3DOF assumption:

$$\begin{bmatrix}\ddot{x}\\ \ddot{y}\\ \ddot{z}\end{bmatrix} = \begin{bmatrix}\dot{u}\\ \dot{v}\\ \dot{w}\end{bmatrix} + \begin{bmatrix}qw\\ 0\\ -qu\end{bmatrix} \tag{40}$$

It should also be noted that the gravity force were transformed to body axes coordinate system as well. Untransforming the gravity force into vehicle carried coordinate system and using the relation above (40), the translational equations of motion transform into:

$$\ddot{x} = \frac{X_V}{m} \tag{41}$$

$$\ddot{z} = \frac{Z_V}{m} - g \tag{42}$$

As the pitch axis on the vehicle carried coordinate system and the y-axis on the body axis coordinate system is coincident, the following relation can be written:

$$\dot{q} = \ddot{\theta} = \frac{Y_m}{I_{yy}} = \frac{Y_{m,V}}{I_{yy}} \tag{43}$$

The axes, forces and moments on the decoy can be seen from Figure 9.

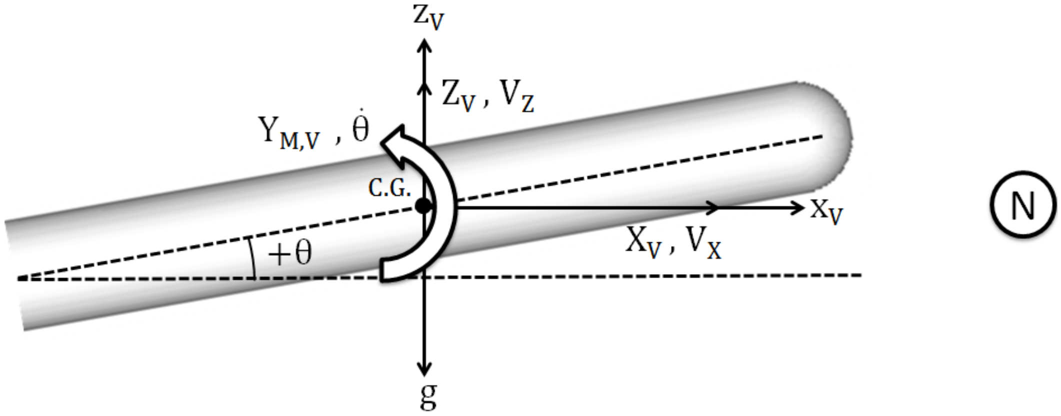

Figure 9. Forces and Moments acting on the Decoy with respect to inertial axes in 3DOF

2.5 AERODYNAMIC FORCES AND MOMENTS ACTING ON THE BODY

The decoy studied in this thesis has a tail geometry with no control infrastructure and no propulsion, hence the only forces and moment acting on the decoy are the aerodynamic forces and moments, which are drag, lift and the pitching moment created due to the asymmetrical pressure distribution on the longitudinal axis. They are defined in the wind axes coordinate system and given as:

$$D = \frac{\gamma}{2}\, P_\infty\, M_\infty^2\, S_{ref}\, C_D \tag{44}$$

$$L = \frac{\gamma}{2}\, P_\infty\, M_\infty^2\, S_{ref}\, C_L \tag{45}$$

$$M = \frac{\gamma}{2}\, P_\infty\, M_\infty^2\, S_{ref}\, l_{ref}\, C_M \tag{46}$$

Due to the three-degree-of-freedom assumption, there is no sideslip angle on the wind axis, which implies that the y-axis on the wind frame, body frame and vehicle carried coordinate system are coincident. Hence there is no need for the pitching moment on the wind axis to be transformed. In order to transform the remaining aerodynamic forces from wind axes to vehicle carried coordinate system:

$$F_V = \begin{bmatrix} X_I \\ 0 \\ Z_I \end{bmatrix} = L_{BV}\, L_{WB} \begin{bmatrix} D \\ 0 \\ L \end{bmatrix} = \begin{bmatrix} \cos\theta & 0 & -\sin\theta \\ 0 & 1 & 0 \\ \sin\theta & 0 & \cos\theta \end{bmatrix} \begin{bmatrix} \cos\alpha & 0 & -\sin\alpha \\ 0 & 1 & 0 \\ \sin\alpha & 0 & \cos\alpha \end{bmatrix} \begin{bmatrix} D \\ 0 \\ L \end{bmatrix} \tag{47}$$

$$X_I = D\cos(\alpha+\theta) - L\sin(\alpha+\theta) \tag{48}$$

$$Z_I = D\sin(\alpha+\theta) + L\cos(\alpha+\theta) \tag{49}$$

$$Y_{m,I} = Y_m = M \tag{50}$$

Note that the aerodynamic force and moment equations, a coefficient term is present. The coefficient term is dependent on Reynolds Number, which is a dimensionless number representing the flow characteristics, the orientation of the body according to the flow (α, β), Mach number of the flow, which represents the compressibility of the flow, and the rates the body is rotating. Besides, the moment coefficient also depends on the center of gravity location of the decoy. [8] For the drag coefficient, with the help of Taylor Series expansion, the dependencies can be written such as:

$$\begin{gathered} C_D(\alpha,\beta,M_\infty,Re,p,q,r) = C_{D0}(Re,M_\infty) + C_{D,\alpha}\alpha + C_{D,\beta}\beta + \\ C_{D,\alpha^2}\alpha^2 + C_{D,\beta^2}\beta^2 + C_{D,\alpha\beta}\,\alpha\,\beta + C_{D,p}p + C_{D,q}q + C_{D,r}r + \cdots \end{gathered} \tag{51}$$

According to reference [8], drag, lift and moment coefficient for a missile can be written as:

$$C_D(\alpha,\beta,M_\infty,Re,p,q,r) = C_{D0}(Re,M_\infty) + C_{D,\alpha^2}\alpha^2 \tag{52}$$

$$C_L(\alpha,\beta,M_\infty,Re,p,q,r) = C_{L0}(Re,M_\infty) + C_{L,\alpha}\alpha \tag{53}$$

$$C_M(\alpha,\beta,M_\infty,Re,p,q,r,cg) = C_{M0}(Re,M_\infty,cg) + C_{M,\alpha}\alpha + C_{M,q}q \tag{54}$$

Note that, while the drag and lift coefficients are dependent on only angle of attack, the moment coefficient is also dependent on the pitching rate, which equals to $\dot{\theta}$ with the three-degree-of-freedom motion assumption. The term $C_{M,q}$ also known as the "pitch damping" term, is found out to be crucial for estimating the pitch angle, which is going to be explained in Section 4.3.

The methodology to find the variation of drag, lift and moment coefficient with angle of attack, Reynolds Number and pitching rate for only the moment coefficient are going to be explained in Chapter 3 and Section 4.3.1.

2.6 NUMERICAL IMPLEMENTATION

The numerical implementation of the problem was done by using four modules: atmospheric conditions module, geometrical properties module, aerodynamic data table lookup module and the time integration module. The flowchart of the numerical implementation can be seen from Figure 10. The 3DOF Numerical Implementation is called 3FL-DYN throughout the thesis. (3DOF Flight Dynamics)

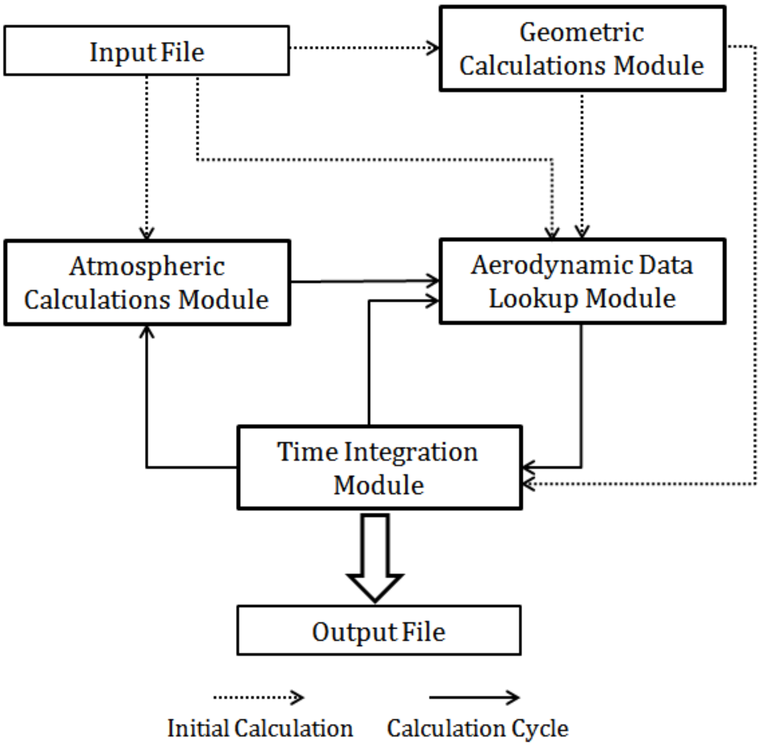

Figure 10. The flowchart of 3FL-DYN

Atmospheric conditions module calculates the ISA conditions at which altitude the decoy is after its release and feeds this information to the aerodynamic data table lookup and time-integration module during both the initial calculations and the calculation cycle.

Geometric properties module calculates the inertia and keeps the mass and the tail size information of the decoy. This module is not included in the calculation cycle, it is used only in the initial calculations phase due to the fact that the mass and the inertia of the decoy does not change as time progresses.

Aerodynamic data table lookup module reads the aerodynamic data tables of the decoy at different Mach numbers and angles of attack and linearly interpolates these data according to the flight parameters of the decoy calculated by the time integration module. Then, it feeds the new information to the time integration module. Hence, it is used for both the initial calculations and calculation cycle.

Time-integration module integrates the 3DOF flight equations over time to find the orientation and the position of the decoy after one time step utilizing Runge-Kutta time integration algorithm. It is fed by all of the other modules. It is the main element of the calculation cycle.

2.6.1 Atmospheric Conditions Module

The atmospheric conditions during decoy flight are calculated by using the International Standard Atmosphere (ISA) model. International Standard Atmosphere is a model [10] used to obtain the atmospheric conditions at different altitudes like density, pressure, temperature etc. The equations to find these atmospheric properties until the stratosphere (36089 ft) are given below, in where SL subscript defines the standard sea level conditions.

$$T_{ALT} = T_{SL} - L_h . h_{ALT} \tag{55}$$

$$P_{ALT} = P_{SL} \left(\frac{T_{ALT}}{T_{SL}} \right)^{g/L_h R} \tag{56}$$

$$\rho_{ALT} = \rho_{SL} \frac{P_{ALT}}{P_{SL}} \frac{T_{SL}}{T_{ALT}} \tag{57}$$

2.6.2 Geometric Calculations Module

The center of gravity (c.g.) of the decoy is calculated from the longitudinal center (half-length) of the decoy. (Figure 11) If the center of gravity is located towards the nose of the decoy it is positive. The mass distribution of the decoy is assumed to be symmetrical on the lateral axes, so that the center of gravity only changes in the longitudinal axis.

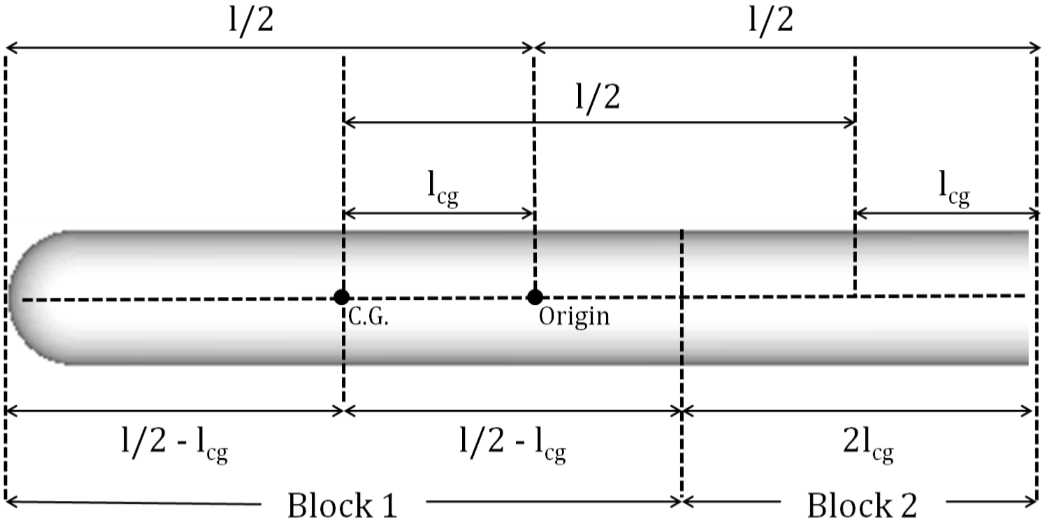

Figure 11. Center of Gravity Reference and Inertia Calculation

Accordingly, the inertia along the pitch axis of the decoy varies with the center of gravity location of the decoy as well. During the inertia calculations, it is assumed that the decoy is a rectangular prism implying that the mass is distributed homogeneously along the decoy and the curvatures on the nose and sides of the decoy is not accounted for. After these assumptions, the pitch inertia variation with the center of gravity can be calculated.

The mass moment of inertia of the decoy around the axis shown in Figure 11 whose center of gravity is located on the centroid of the volume is:

$$I = \frac{1}{12} m(l^2 + h^2) \tag{58}$$

So when the center of gravity of the decoy is shifted, the parallel axis theorem should be applied. This is due to the fact that the mass moment of inertia is actually the superposition of a new rectangular block whose centroid is located on the center of gravity of the decoy named Block 1 and Block 2, which is the remaining part. Block 1 and Block 2 are illustrated in Figure 11.

Taking the even mass distribution assumption into account, the mass of Block 1 and Block 2 is as follows:

$$m = m_1 + m_2 \tag{59}$$

$$m_1 = \left(1 - \frac{2l_{cg}}{l}\right)m \tag{60}$$

$$m_2 = \frac{2l_{cg}}{l}m \tag{61}$$

Then, the mass moment of inertia of the block 1 is:

$$I_1 = \frac{1}{12}m_1\left[\left(l - 2l_{cg}\right)^2 + h^2\right] \tag{62}$$

$$I_1 = \frac{1}{12}m\left(1 - \frac{2l_{cg}}{l}\right)\left[\left(l - 2l_{cg}\right)^2 + h^2\right] \tag{63}$$

Applying the parallel axes theorem, the mass moment of inertia of the block 2 is:

$$I_2 = \frac{1}{12}m_2\left[\left(2l_{cg}\right)^2 + h^2\right] + \frac{m_2 l}{2} \tag{64}$$

$$I_2 = \frac{1}{12}\frac{2l_{cg}}{l}m\left[\left(2l_{cg}\right)^2 + h^2\right] + \frac{\frac{2l_{cg}}{l}ml}{2} \tag{65}$$

Adding the two together:

$$I = I_{yy} = \frac{1}{12}m\left(1 - \frac{2l_{cg}}{l}\right)\left(\left(l - 2l_{cg}\right)^2 + h^2\right) + \frac{l_{cg}}{6l}m\left(4{l_{cg}}^2 + h^2\right) + l_{cg}m \tag{66}$$

2.6.3 Aerodynamic Data Table Lookup Module

The methodology to obtain the aerodynamic forces and moments acting on the decoy are to be explained in Chapter 3. Owing to the fact that the analyses were run at a matrix of certain conditions (angle of attack, Mach number etc.), the conditions required by the 3FL-DYN which falls between these conditions should be interpolated. All conditions covered are interpolated linearly. For instance, when the decoy has a flight Mach number of M and angle of attack of α, the interpolation of lift coefficient of the decoy is done according to:

$$M_1 < M < M_2$$

$$\alpha_1 < \alpha < \alpha_2$$

$$\begin{gathered} C_L(\alpha, M) = C_L(\alpha, M_1) + \frac{C_L(\alpha, M_2) - C_L(\alpha, M_1)}{M_2 - M_1}(M - M_1) \\ C_L(\alpha, M_1) = C_L(\alpha_1, M_1) + \frac{C_L(\alpha_2, M_1) - C_L(\alpha_1, M_1)}{\alpha_2 - \alpha_1}(\alpha - \alpha_1) \\ C_L(\alpha, M_2) = C_L(\alpha_1, M_2) + \frac{C_L(\alpha_2, M_2) - C_L(\alpha_1, M_2)}{\alpha_2 - \alpha_1}(\alpha - \alpha_1) \end{gathered} \tag{67}$$

For the moment coefficient of the decoy, the interpolation for the angle of attack and Mach number is done exactly as the example for the lift coefficient above, but in addition another interpolation for the pitching rate is done:

$$M_1 < M < M_2$$

$$\alpha_1 < \alpha < \alpha_2$$

$$\begin{gathered} C_{M0}(\alpha, M) = C_{M0}(\alpha, M_1) + \frac{C_{M0}(\alpha, M_2) - C_{M0}(\alpha, M_1)}{M_2 - M_1}(M - M_1) \\ C_{M0}(\alpha, M_1) = C_{M0}(\alpha_1, M_1) + \frac{C_{M0}(\alpha_2, M_1) - C_{M0}(\alpha_1, M_1)}{\alpha_2 - \alpha_1}(\alpha - \alpha_1) \\ C_{M0}(\alpha, M_2) = C_{M0}(\alpha_1, M_2) + \frac{C_{M0}(\alpha_2, M_2) - C_{M0}(\alpha_1, M_2)}{\alpha_2 - \alpha_1}(\alpha - \alpha_1) \end{gathered} \tag{68}$$

$$C_{M,q}(\alpha, M) = C_{M,q}(\alpha, M_1) + \frac{C_{M,q}(\alpha, M_2) - C_{M,q}(\alpha, M_1)}{M_2 - M_1}(M - M_1)$$

$$C_{M,q}(\alpha, M_1) = C_{M,q}(\alpha_1, M_1) + \frac{C_{M,q}(\alpha_2, M_1) - C_{M,q}(\alpha_1, M_1)}{\alpha_2 - \alpha_1}(\alpha - \alpha_1)$$

$$C_{M,q}(\alpha, M_2) = C_{M,q}(\alpha_1, M_2) + \frac{C_{M,q}(\alpha_2, M_2) - C_{M,q}(\alpha_1, M_2)}{\alpha_2 - \alpha_1}(\alpha - \alpha_1)$$

$$C_M(\alpha, M) = C_{M0}(\alpha, M) + C_{M,q}(\alpha, M)\, q$$

As stated in Section 2.6.2, the center of gravity is measured from the half length of the decoy with positive direction pointing towards the nose, the output of the methodology for obtaining the aerodynamic moments was taken out according to this reference point as well. In order to add the effect of center of gravity location to the moment coefficient, a recalculation of the moment coefficient according to the cg location of the decoy is done. From Figure 12, when the moment is taken according to the new cg location:

$$C_M\left(l_{cg}\right) = C_M\left(l_{cg} = 0\right) - l_{cg}\,\left(C_L\, cos\,\alpha + C_D\, sin\,\alpha\right) \qquad (69)$$

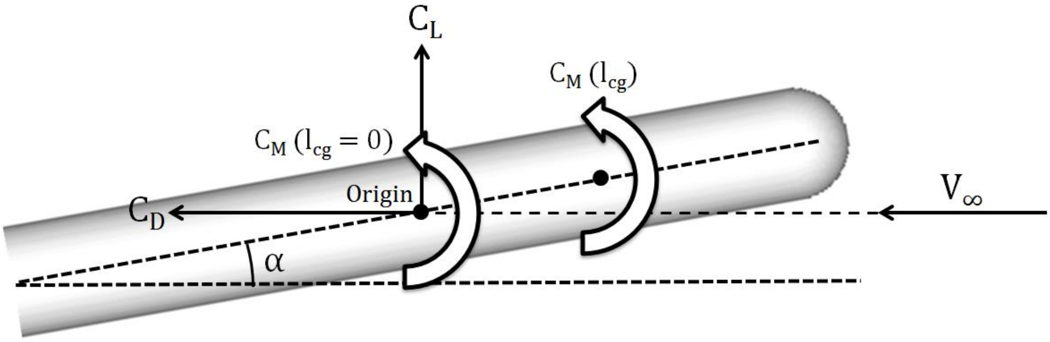

Figure 12. Recalculation of Moment Coefficient

2.6.4 Time Integration Module

Runge-Kutta methods are numerical methods involving successive steps that are used to solve differential equations. Runge-Kutta methods have different orders of accuracy. The classical Runge-Kutta method, which is a fourth-order method and sometimes referred to as RK4 method, is utilized in 3FL-DYN. RK4 method discretizes the time step that is being calculated into four steps: calculation is done at the beginning, the midpoint followed by a reiteration of the midpoint of the time interval and the end of the time interval with more weight on the values calculated at midpoint. [11]

The 3DOF equations of motion in this thesis given in Section 2.4 are three second order ordinary differential equations (ODE) that depend on time. Writing the three 2nd order ODE's as six 1st order ODE's with variable manipulation in terms of displacement and its derivatives (Figure 9):

$$\ddot{x} = \dot{V}_x = \frac{X_V}{m} \tag{70}$$

$$\ddot{z} = \dot{V}_z = \frac{Z_V}{m} - g \tag{71}$$

$$\ddot{\theta} = \dot{q} = \frac{Y_{m,V}}{I_{yy}} \tag{72}$$

$$\dot{x} = V_x \tag{73}$$

$$\dot{z} = V_z \tag{74}$$

$$\dot{\theta} = q \tag{75}$$

When RK4 is applied this system of equations and the variables are written as a vector $\vec{X}$:

$$\vec{X} = \begin{bmatrix} x \\ z \\ \theta \\ V_x \\ V_z \\ q \end{bmatrix} = \begin{bmatrix} x(t, V_x) \\ z(t, V_z) \\ \theta(t, q) \\ V_x(t, V_x, V_z, \theta) \\ V_z(t, V_x, V_z, \theta) \\ q(t, V_x, V_z, \theta, q) \end{bmatrix} \tag{76}$$

With the initial values written as a vector of $\vec{X}_0$:

$$\vec{X}_0 = \begin{bmatrix} x_0 \\ z_0 \\ \theta_0 \\ V_{x,0} \\ V_{z,0} \\ q_0 \end{bmatrix} \tag{77}$$

Writing the gradients calculated at four different steps in the time interval for variable V_x at time n, with a time step of Δt:

$$k_{1,V_x} = V_x(t_n, V_{x,n}, V_{z,n}, \theta_n) \tag{78}$$

$$k_{2,V_x} = V_x\left(t_n + \frac{\Delta t}{2}, V_{x,n} + k_{1,V_x}\frac{\Delta t}{2}, V_{z,n} + k_{1,V_z}\frac{\Delta t}{2}, \theta_n + k_{1,\theta}\frac{\Delta t}{2}\right) \tag{79}$$

$$k_{3,V_x} = V_x\left(t_n + \frac{\Delta t}{2}, V_{x,n} + k_{2,V_x}\frac{\Delta t}{2}, V_{z,n} + k_{2,V_z}\frac{\Delta t}{2}, \theta_n + k_{2,\theta}\frac{\Delta t}{2}\right) \tag{80}$$

$$k_{4,V_x} = V_x\left(t_n + \Delta t, V_{x,n} + k_{3,V_x}\Delta t, V_{z,n} + k_{3,V_z}\Delta t, \theta_n + k_{3,\theta}\Delta t\right) \tag{81}$$

Calculating the variable at the next time step $n + 1$:

$$V_{x,n+1} = V_{x,n} + \frac{1}{6}\left(k_{1,V_x} + 2k_{2,V_x} + 2k_{3,V_x} + k_{4,V_x}\right)\Delta t \tag{82}$$

Writing all the gradients for all the variables as a matrix and the integration as a matrix addition and multiplication:

$$\overrightarrow{\mathrm{X}_{n+1}} = \begin{bmatrix} x_{n+1} \\ z_{n+1} \\ \theta_{n+1} \\ V_{x,n+1} \\ V_{z,n+1} \\ q_{n+1} \end{bmatrix} = \begin{bmatrix} x_{n} \\ z_{n} \\ \theta_{n} \\ V_{x,n} \\ V_{z,n} \\ q_{n} \end{bmatrix} + \frac{\Delta t}{6} \begin{bmatrix} k_{1,x} & k_{2,x} & k_{3,x} & k_{4,x} \\ k_{1,z} & k_{2,z} & k_{3,z} & k_{4,z} \\ k_{1,\theta} & k_{2,\theta} & k_{3,\theta} & k_{4,\theta} \\ k_{1,V_x} & k_{2,V_x} & k_{3,V_x} & k_{4,V_x} \\ k_{1,V_z} & k_{2,V_z} & k_{3,V_z} & k_{4,V_z} \\ k_{1,q} & k_{2,q} & k_{3,q} & k_{4,q} \end{bmatrix} \begin{bmatrix} 1 \\ 2 \\ 2 \\ 1 \end{bmatrix} \qquad (83)$$

CHAPTER 3

CALCULATION OF AERODYNAMIC COEFFICIENTS

In this chapter, two different methodologies for calculating the aerodynamic coefficients of the decoy are compared with each other. One of the methodologies is a lower order method based on empirical data while the other is based on the numerical solution of the decoy flowfield.

3.1 METHOD 1 – THE EMPIRICAL SOLUTION (DatCOM)

For the empirical acquirement of the aerodynamic coefficients of the decoy, DatCOM [12] software was utilized. DatCOM is a rapid estimation tool which calculates the aerodynamic coefficients and derivatives of the input geometry. It uses these values to give an estimation about the aerodynamic stability and control characteristics of the body in seconds. DatCOM is able to make estimations about missiles, aircraft etc. by the calculation of aerodynamic coefficients and derivatives done utilizing a component build-up method based on experimental data. DatCOM can be used for preliminary aircraft and missile designs, so the embedded experimental data may not accommodate the Mach and Reynolds Number combination of the decoy.

DatCOM has the capability to address many configurations such as body, wing-body, wing-body-horizontal tail etc., but for comparison purposes only the body configuration was used. [12] An example input file used for tutorials in DatCOM of a MIG-17 aircraft is given in Figure 13.

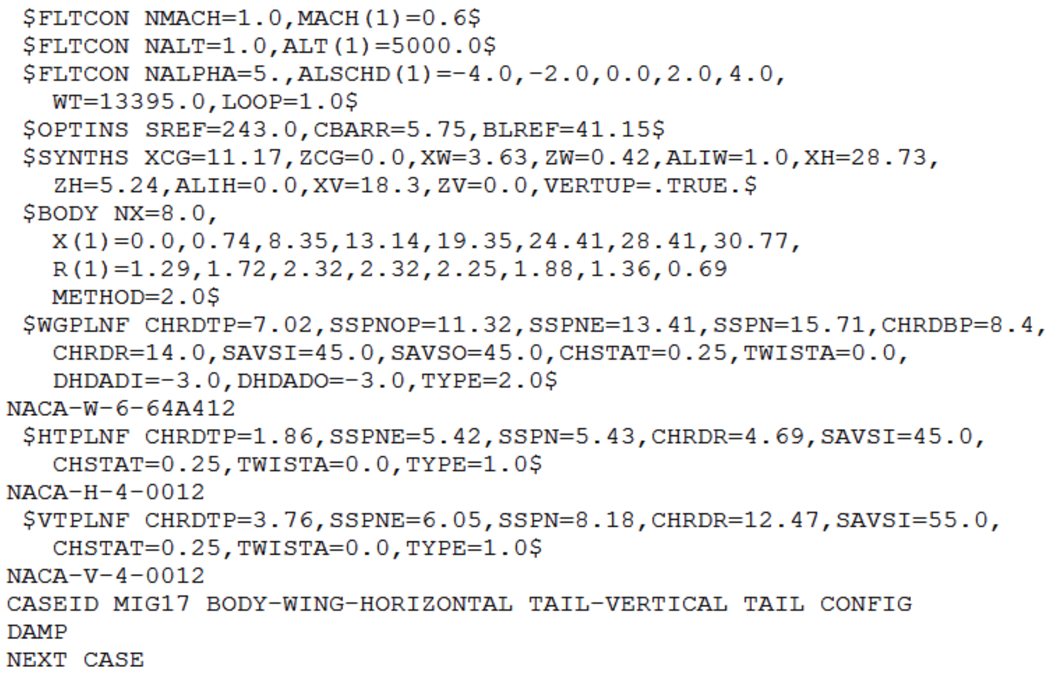

```
 $FLTCON NMACH=1.0,MACH(1)=0.6$
 $FLTCON NALT=1.0,ALT(1)=5000.0$
 $FLTCON NALPHA=5.,ALSCHD(1)=-4.0,-2.0,0.0,2.0,4.0,
   WT=13395.0,LOOP=1.0$
 $OPTINS SREF=243.0,CBARR=5.75,BLREF=41.15$
 $SYNTHS XCG=11.17,ZCG=0.0,XW=3.63,ZW=0.42,ALIW=1.0,XH=28.73,
   ZH=5.24,ALIH=0.0,XV=18.3,ZV=0.0,VERTUP=.TRUE.$
 $BODY NX=8.0,
   X(1)=0.0,0.74,8.35,13.14,19.35,24.41,28.41,30.77,
   R(1)=1.29,1.72,2.32,2.32,2.25,1.88,1.36,0.69
   METHOD=2.0$
 $WGPLNF CHRDTP=7.02,SSPNOP=11.32,SSPNE=13.41,SSPN=15.71,CHRDBP=8.4,
   CHRDR=14.0,SAVSI=45.0,SAVSO=45.0,CHSTAT=0.25,TWISTA=0.0,
   DHDADI=-3.0,DHDADO=-3.0,TYPE=2.0$
NACA-W-6-64A412
 $HTPLNF CHRDTP=1.86,SSPNE=5.42,SSPN=5.43,CHRDR=4.69,SAVSI=45.0,
   CHSTAT=0.25,TWISTA=0.0,TYPE=1.0$
NACA-H-4-0012
 $VTPLNF CHRDTP=3.76,SSPNE=6.05,SSPN=8.18,CHRDR=12.47,SAVSI=55.0,
   CHSTAT=0.25,TWISTA=0.0,TYPE=1.0$
NACA-V-4-0012
CASEID MIG17 BODY-WING-HORIZONTAL TAIL-VERTICAL TAIL CONFIG
DAMP
NEXT CASE
```

Figure 13. Sample DatCOM Input File for MIG-17

In DatCOM, in order to model a body with a rectangular cross-section, the properties of different cross-sections at different longitudinal locations should be input. The parameters to model the body include the cross-sectional area, the periphery, planform half-width and the vertical coordinates at the lower/upper body surfaces. The center of gravity location of the body should be given as well. The nature of the cross-sectional parameters suggests that a true rectangular cross-section cannot be defined in DatCOM due to the fact that only height and width of a rectangle is enough to define a true rectangular cross-section. Besides, DatCOM has a limitation such that no external stores can be modeled because of the fact that it analyzes the body as a body of revolution. Due to this approach, separation from sides of the decoy caused by the blunt edges may not be modeled effectively. [12]

DatCOM is also able to evaluate a configuration at different Mach numbers ranging from subsonic to hypersonic speeds at different altitudes. In this study, subsonic Mach numbers at subsonic flow region are considered. [12]

DatCOM has many limitations like the “body-of-revolution” approach and the possible non-existence of the Reynolds – Mach number range of the decoy, but as it can calculate aerodynamic data tables in seconds, it was decided to be evaluated.

3.2 METHOD 2 – THE NUMERICAL SOLUTION

For the numerical solution of the decoy, the commercial solver FLUENT was used. FLUENT is a computational fluid dynamics (CFD) solver utilizing the Reynolds-Averaged Navier-Stokes (RANS) equations for steady or unsteady inviscid, turbulent and laminar flow problems. FLUENT has a variety of turbulence models like k-omega, k-epsilon, Spalart-Allmaras etc. utilizing different wall treatment models as well as different discretization schemes. It is able to solve every flow regime such as subsonic, transonic, supersonic etc. [14]

HyperMesh [13] is a pre-processor which is able to create both triangular and quad surface meshes for geometries. It has a CFD meshing algorithm that is able to create finer meshes on curved surfaces, while the mesh on the straight surfaces are coarsened. For boundary-layer and volume meshing, Tgrid [14] software which has well-defined algorithms embedded in FLUENT that can produce quality meshes was used.

FLUENT also has the capability to solve the problems with parallel processes to speed up the analysis.

3.2.1 Governing Equations

For all types of flows, FLUENT solves the Reynolds-Averaged Navier-Stokes equations, which involves one conservation of mass (continuity) and three conservation of momentum equations in three directions. If the flow is compressible, due to the necessity for solving the density, the energy equation is also needed to be solved. As the static temperature variable emerges from the energy equation, the ideal gas law has to be solved as well. [15]

When the decoy is ejected from the aircraft, it is exposed to the turbulent flowfield around the aircraft implying that the flow around the decoy is turbulent. Hence, turbulence should also be included in the solution. In order to do this, FLUENT solves additional transport equations like kinetic energy transport equation. All these equations are given below. The subcripts i and j differ from 1 to 3.

Continuity equation:

$$\frac{\partial \rho}{\partial t} + \frac{\partial}{\partial x_i}(\rho u_i) = 0 \tag{84}$$

The averaged momentum equations:

$$\rho\left(\frac{\partial \overline{u_i}}{\partial t} + U_j \frac{\partial \overline{u_i}}{\partial x_j}\right) = \frac{\partial}{\partial x_j}\left(-\bar{P}\delta_{ij} + \mu\left(\frac{\partial \overline{u_i}}{\partial x_j} + \frac{\partial \overline{u_j}}{\partial x_i}\right) - \rho\overline{u_i{}' u_j{}'}\right) \tag{85}$$

where the terms on the right hand side of the equation is isotropic pressure component, viscous stress and Reynolds stresses respectively.

Ideal gas law:

$$P = \rho R T \tag{86}$$

Energy equation for a flow involving turbulent conductivity and viscous dissipation:

$$\frac{\partial}{\partial t}(\rho E) + \nabla.[u(\rho E + P)] = \nabla.(k_{eff}\nabla T + \overline{\overline{\tau_{eff}}}.\vec{u}) \tag{87}$$

Kinetic energy transport equation:

$$\left[\frac{\partial k}{\partial t} + \overline{U_j}\frac{\partial k}{\partial x_j}\right] = -\frac{\partial}{\partial x_j}\left[\frac{1}{2}\overline{u_i' u_j' u_j'} + \frac{1}{\rho}\overline{p' u_j'} - 2\nu\overline{u_i' s_{ij}}\right] - \overline{u_i' u_j'}\frac{\partial \overline{U_i}}{\partial x_j} - 2\nu\overline{s_{ij} s_{ij}} \tag{88}$$

Where s_{ij} is the strain rate term and defined as:

$$s_{ij} = \frac{1}{2}\left(\frac{\partial u_i'}{\partial x_j} + \frac{\partial u_j'}{\partial x_i}\right) \tag{89}$$

3.2.2 Turbulence Modeling

Turbulent flow is the flow of a fluid in which its vorticity at any point and time is random and has a wide and continuous distribution of length and time scales. The flow is essentially unsteady, three-dimensional and any flow quantity is random in time and space. [16] Turbulent flow problem has its own set of differential equations, but solving them, called the Direct Numerical Simulation (DNS), is computationally expensive due to very fine mesh requirements in the order of billions as well as the complexity of equations. [17]

Luckily, the mean quantities of turbulent flows are deterministic implying that if the governing equations are to be time-averaged, the fluctuations are going to be smoothed out, decreasing the computational expense. This is achieved by using Reynolds-Averaging and filtering methods on the turbulent Navier-Stokes equations. However, these methods yield some unknowns, resulting in the “Closure problem”. [15] The problem with the averaging is the number of unknowns is always one higher than the number of equations. At this point, the turbulence modeling is utilized in such a way that using the known quantities, the unknown parameters are simulated.

There are many turbulence models with each having their strengths and weaknesses for different flow solutions:

Spalart-Allmaras model is a one-equation low-cost model that solves a Reynolds Averaged transport equation for the eddy viscosity. Generally, it is used for wall-bounded flow with mild separation like supersonic/transonic flows over airfoils, boundary layer flows etc. [18]

k-omega model is a two-equation model that solves transport equations for both the turbulent kinetic energy and omega, which is the ratio of turbulent dissipation rate to turbulent kinetic energy, k. This model is superior for wall-bounded low Reynolds number flows due to the fact that it solves the viscous sublayer with no wall-treatment. As this model resolves the viscous sublayer, it requires very fine mesh near the wall increasing the computational cost. [18]

k-epsilon model is a two equation model that solves transport equations for both the turbulent kinetic energy and turbulent dissipation rate. This model is the most widely used turbulence model in the industry for especially external flow problems. It is proven to be sufficiently accurate for a wide range of flow problems. It also has different formulations such as RNG k-epsilon and Realizable k-epsilon. They are computationally lower-cost than k-omega model due to the fact that near the walls, a wall treatment model is applied since the viscous sublayer is not resolved. [18]

There are also three, four equation models such as Transition k-kl-omega, Transition SST as well as Reynolds Stress Model (RSM) which have seven extra equations, but due to computational expenses they are not utilized in flow solutions.

Realizable k-epsilon model was selected due to the fact that it handles separation, recirculation, swirling etc. better than the other k-epsilon models with being easiest to converge among them. [14]

3.2.3 Boundary Conditions

In this study, pressure-farfield boundary condition was utilized for a spherical domain. Pressure farfield is a boundary condition that models the free-stream conditions at infinity, using the freestream Mach number and static conditions such as temperature. [14] This boundary condition can only be applied if the flow is compressible. FLUENT extrapolates the flow variables inside of the domain starting from the freestream conditions.

Adiabatic wall boundary condition with no slip was used for the decoy geometry.

3.2.4 Solver Approaches And Discretization

FLUENT has two types of solvers: Pressure-Based Solver and Density Based Solver. In the Pressure-Based Approach, pressure is an unknown variable in the governing equations and the density of the flow is derived from the ideal-gas law; while in the density based approach, density is the unknown and pressure is the one being derived from the ideal-gas law. Density-based approach yields better results when a strong coupling between momentum, pressure and density is expected, like a high-speed compressible flow with combustion. Hence, in this thesis the pressure-based approach was used. [14]

FLUENT has two types of Pressure-Based solver approaches: Segregated and Coupled. As the name implies, Segregated approach solves the pressure and momentum sequentially; while the Coupled approach solves them at the same time. Although the simultaneous solution of pressure and momentum results in higher memory usage, it yields better results than the Segregated approach. Hence, in this study the Coupled approach was utilized. [14]

FLUENT keeps the scalar values stored at cell centers. For the flux terms at the cell faces, upwind scheme is utilized. In first-order upwind scheme, it is assumed that the values at the cell centers are equal to the values at cell faces, while in higher-order upwind scheme Taylor Series expansion of the values at cell centers to find the values at cell faces. For pressure, density, momentum, energy, turbulent dissipation rate and turbulent kinetic energy, second-order upwind discretization schemes were utilized.

For the evaluation of diffusive fluxes, velocity derivatives etc., the gradients of some solution variables, such as pressure, should be found. There are three methods in FLUENT to calculate the gradients of solution variables, from which the Green-Gauss Node-Based was selected due to the fact that although it is computationally more intensive, it minimizes false diffusion, is more accurate and appropriate for unstructured meshes. [14]

3.2.5 Computational Grid Generation

For grid generation, two preprocessors were used: HyperMesh for unstructured surface mesh generation for both the domain and the decoy; TGrid for boundary layer and tetrahedral flow domain meshes.

For the decoy surface mesh generation, the step model of the decoy geometry was imported into HyperMesh and some modifications were made in order to have better quality mesh. Taking the necessary first layer height emerging from the required y-plus value for wall-treatment model into account, surface mesh sizes was selected. This is important due to the fact the aspect ratio between the first prism layer cell and the surface mesh should not be too high to obtain better numerical accuracy. Besides, in the curved surfaces of the geometry as well as the tail section, “R-tria” mesh type, which is actually a triangular mesh type with a right angle, was utilized due to the fact that especially the curved surfaces are more accurately defined. [13] Figure 14 and Figure 15 show the surface mesh of the decoy for Grid #2 around the nose and tail regions.

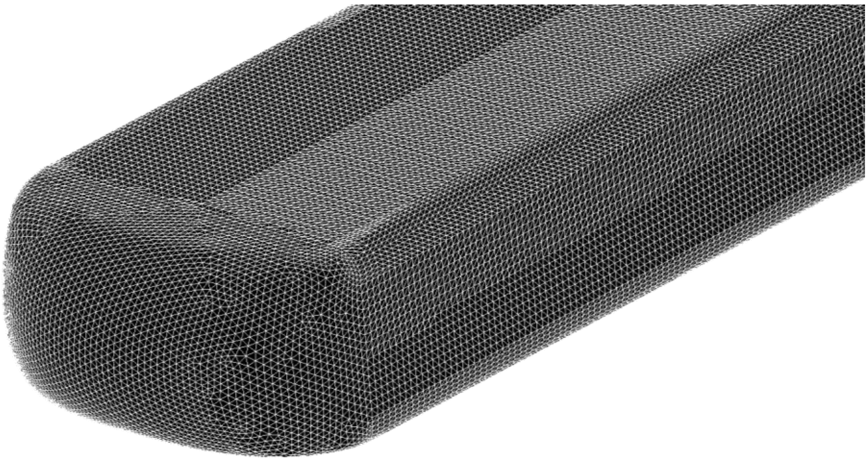

Figure 14. The Surface Mesh Around the Nose Region of the Decoy (Grid #2)

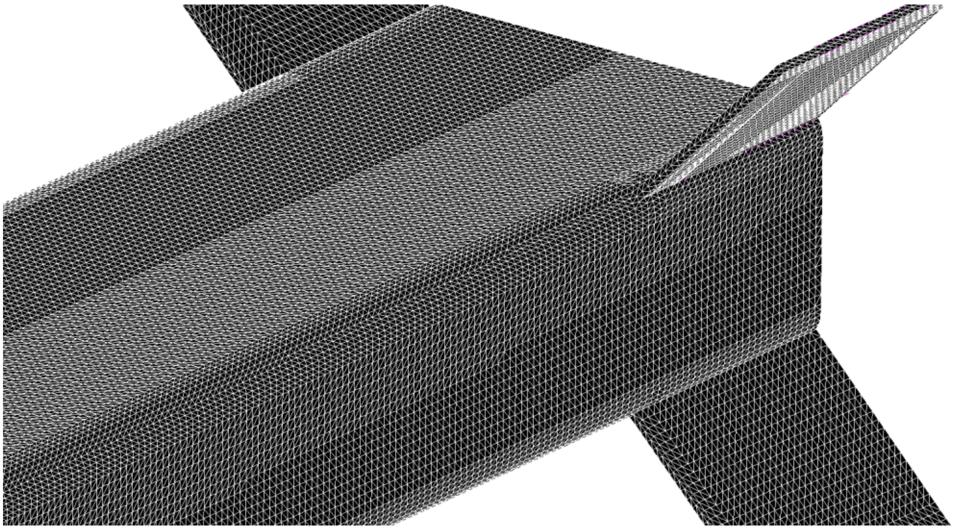

Figure 15. The Surface Mesh Around the Tail Region of the Decoy (Grid #2)

For the domain surface mesh generation, in order to find the surface mesh size of the domain geometry, the tethahedral size growing with a constant rate from the boundary layer of the decoy was taken into account. Figure 16 shows the domain surface mesh.

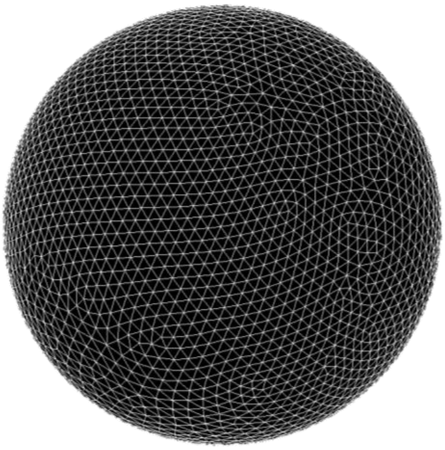

Figure 16. The Surface Mesh Around the Domain

After the surface mesh generation was finalized, the mesh was imported to TGrid software to first generate the boundary layer prisms, then the domain mesh tetrahedrals.

For boundary layer generation, a first layer height which is going to yield a y-plus value between 30 and 300, at different flow velocities was selected. This y-plus interval emerges from the turbulence and wall-treatment model selection. [18] In order to estimate the boundary layer thickness, a turbulent flat plate boundary layer thickness formulation was utilized. As the decoy geometry is simple, prism layer mesh generation was done with a constant geometric growth rate methodology. The number of prism layers is dependent on the estimated boundary layer thickness. Figure 17 shows the overall prism layer thickness distribution around the decoy, while Table 1 represents the prism layer mesh parameters.

Table 1. Prism Layer Mesh Parameters

First Layer Thickness (mm)	0.1
Number of Prism Layers	11
Growth Rate	1.2

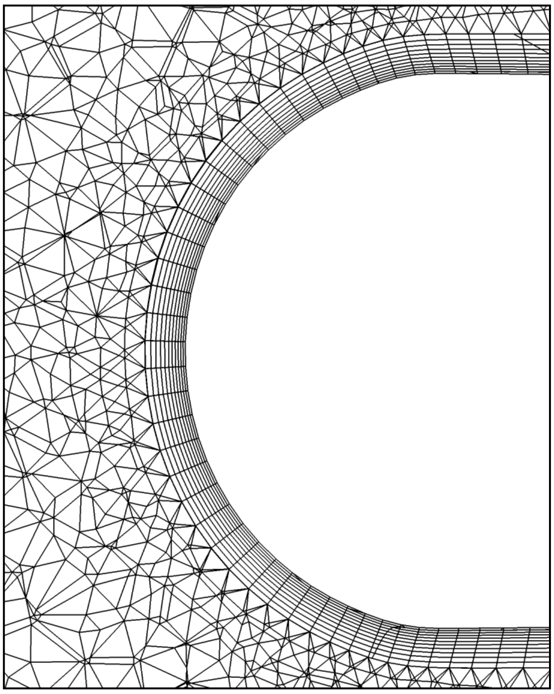

Figure 17. Overall Prism Layer Thickness Distribution Around the Decoy

The flow domain is a sphere, whose radius is fifteen times bigger than the length of the decoy. This was done so that the flow around the geometry does not affect the freestream boundary conditions.

The selected mesh size and its reasons of selection are going to be explained in the grid independence study at Section 4.4.

3.3 METHODOLOGY COMPARISON

To compare the two methodologies, the same decoy body was modeled at two different Mach numbers, one of which had compressibility effects, and the drag, lift and moment coefficients of the decoy were found. The decoy body was solved at angles of attack up to 90° with an interval of 5° between them for both methodologies.

Between Figure 18 and Figure 23, the comparison between DatCOM and FLUENT for drag, lift and moment coefficients at Mach numbers of 0.3 and 0.6 are shown, respectively.

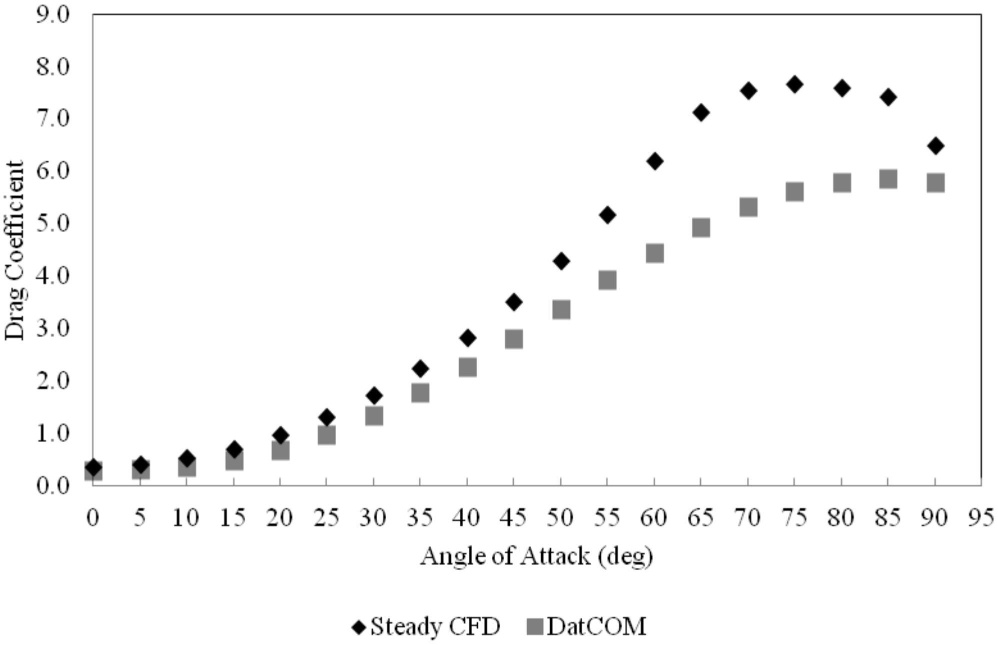

Figure 18. Comparison of drag coefficients calculated by two methodologies at M=0.3

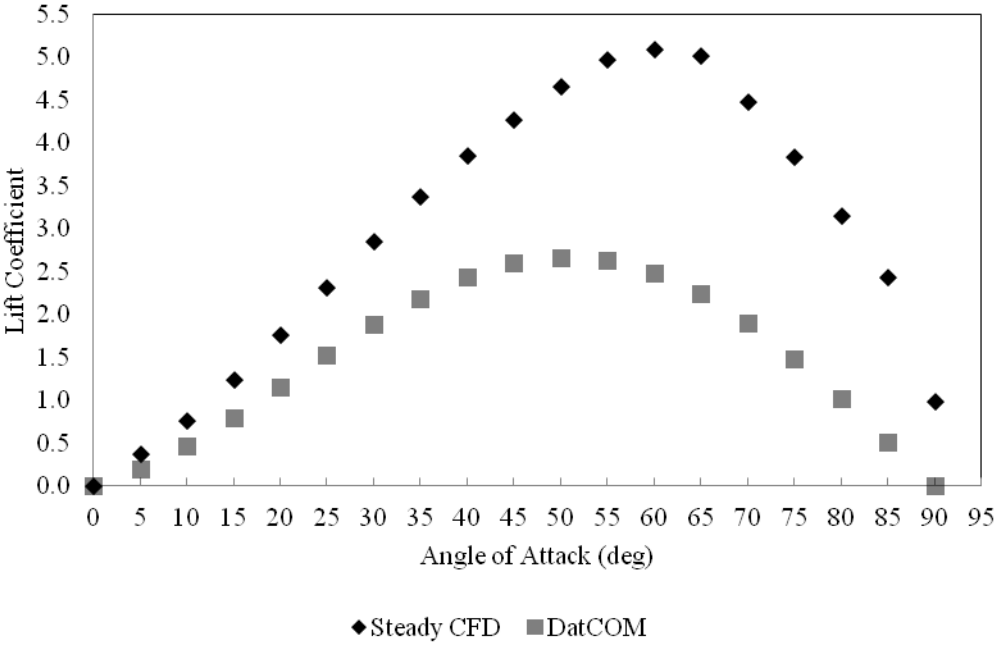

Figure 19. Comparison of lift coefficients calculated by two methodologies at M=0.3

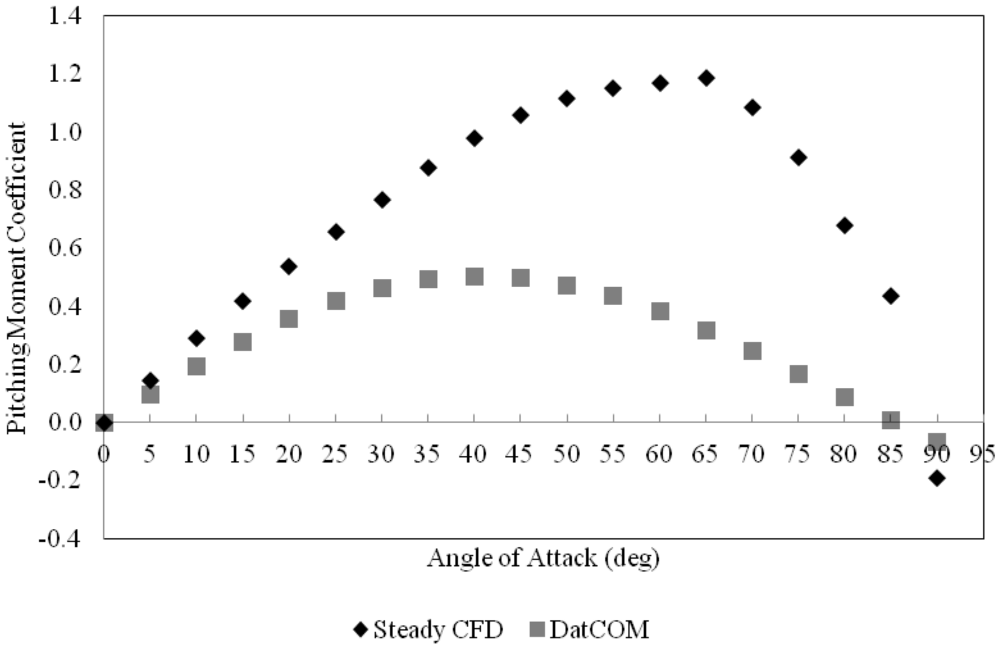

Figure 20. Comparison of pitching moment coefficients calculated by two methodologies at M=0.3

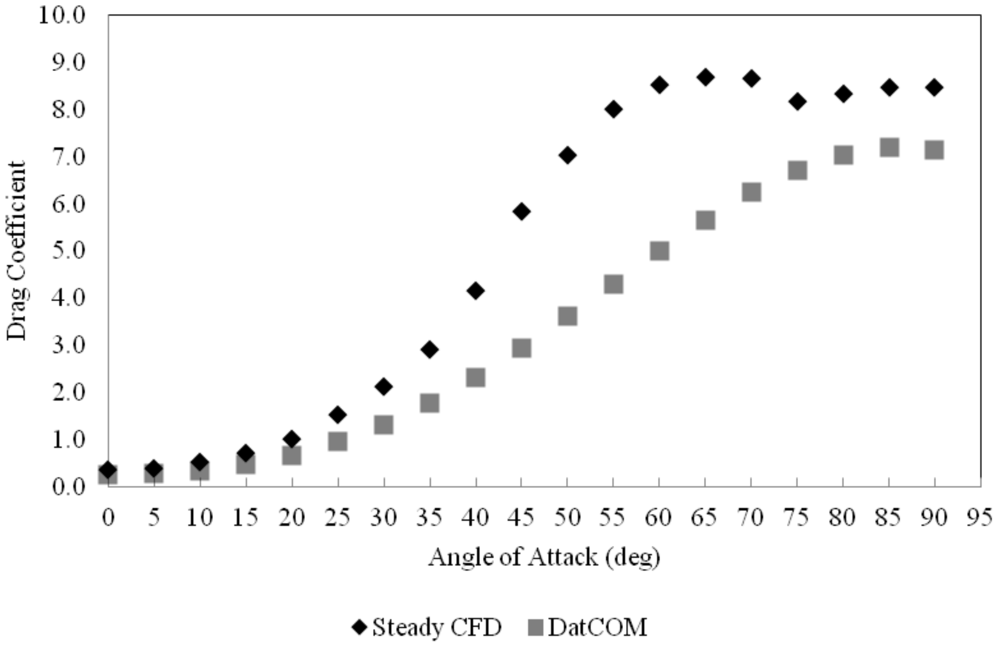

Figure 21. Comparison of drag coefficients calculated by two methodologies at M=0.6

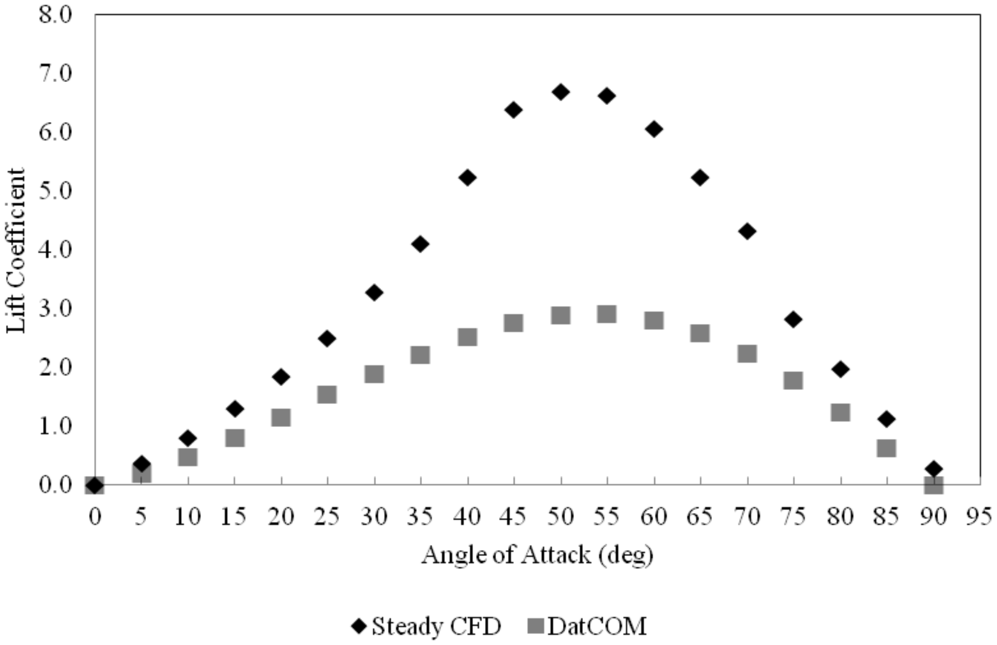

Figure 22. Comparison of lift coefficients calculated by two methodologies at M=0.6

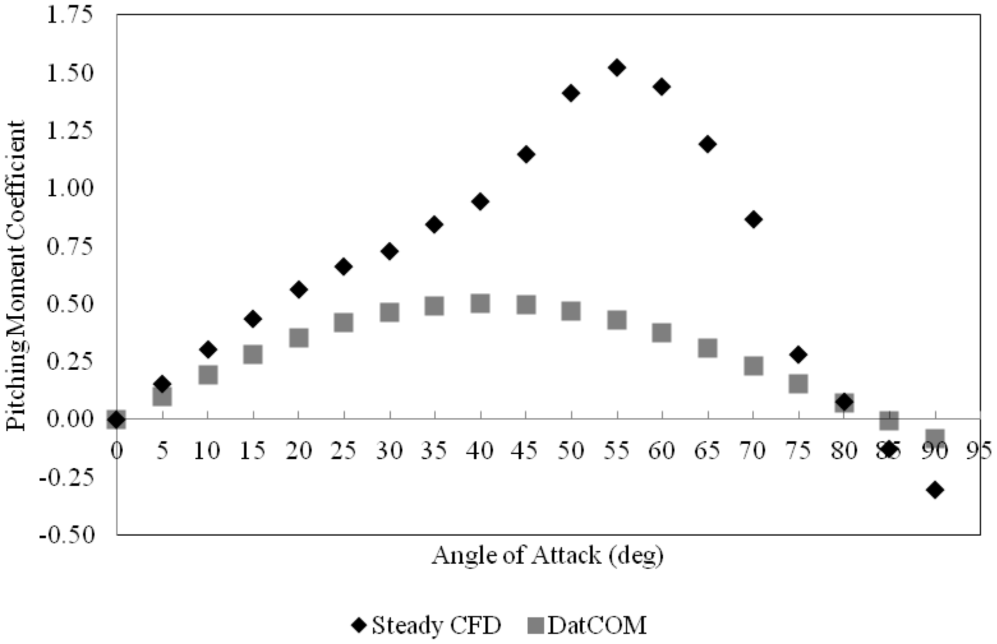

Figure 23. Comparison of pitching moment coefficients calculated by two methodologies at M=0.6

The figures clearly show that the results of two methodologies are not similar. Generally, DatCOM predicts smaller forces and moments. The differences between two methodologies are especially greater for lift and moment coefficients. For M = 0.6, the lift coefficient predicted by FLUENT is two and a half times the value predicted by DatCOM at 50° angle of attack. Besides, in some cases the trends of the results are not similar either. For instance, in Figure 23 the pitching moment peak predicted at 55° angle of attack is not observable in DatCOM predictions, while in Figure 21, the increase in drag due to accelerated flow reaching transonic flow region on the nose area is not predicted by DatCOM method.

Based on such differences observed, FLUENT solutions were decided to be the reference solutions because of higher level of equations solved with compressibility and seperated boundary layer effects. The reasons behind the lack of accuracy of DatCOM, its limitations was explained in Section 3.1.

CHAPTER 4

ASSESSMENT OF THE METHODOLOGY

4.1 NON-DIMENSIONAL QUANTITIES

In this study, from this point on, time histories of Euler Angles and angular rates / accelerations as well as trajectories are going to be given as results. These quantities are non-dimensionalized with a reference value and given with the subscript of “nd”. They are non-dimensionalized as:

$$\begin{aligned} t_{nd} &= \frac{t}{t_{ref}} \times 100 \\ x_{nd} &= \frac{x}{l_{ref}} \\ h_{ALT,nd} &= \frac{h_{ALT}}{h_{ALT,ref}} \times 100 \\ \phi_{nd} &= \frac{\phi}{\phi_{ref}} \\ \theta_{nd} &= \frac{\theta}{\theta_{ref}} \\ \psi_{nd} &= \frac{\psi}{\psi_{ref}} \\ q_{nd} &= \frac{q}{q_{ref}} \end{aligned} \tag{90}$$

$$\dot{q}_{nd} = \frac{\dot{q}}{\dot{q}_{ref}}$$

where l is the reference length and $h_{ALT,ref}$ is the reference pressure altitude of the decoy. t_{ref} is the total flight duration of interest.

4.2 TIME-STEP SELECTION

Both the 3FL-DYN and the transient CFD analyses are based on the integration of certain variables like acceleration or velocity with time. The time step utilized in the integrations directly affects the accuracy of the integrated quantities, but a very small time step is going to increase the calculation cost in terms of time and computational power. Hence, a time step which is going to yield the sufficient accuracy with an optimization of calculational cost should be selected.

4.2.1 Time Step Selection for 3FL-DYN

For the evalulation of the time step size for 3FL-DYN, pitch angle (θ) and pitching rate (q) vs. time graphs are plotted for different time step sizes for a dynamically stable case at two different Mach numbers as can be seen from Figure 24 to Figure 27. Pitch angle and pitching rate time histories are picked for time step selection, as these quantities are most prone to numerical errors.

The graphs show that effect of time step size on the accuracy of the solution is more evident in the M = 0.6 case due to the fact that the forces and moments acting on the decoy are higher. In the M = 0.3 case, the solution acquired at a time step of 0.2ms yields a sufficiently accurate solution as it shows nearly identical results with the solutions attained with time steps of 0.01 and 0.02ms. However, for the M = 0.6 case, the solution acquired at 0.2ms starts to differ from the solutions at 0.01 and 0.02ms as time marches on. The solutions for 0.01 and 0.02ms are identical to each other. Therefore, in order to reduce computational cost and preserve accuracy, a time step of 0.02ms is selected for the dynamic analyses with 3FL-DYN.

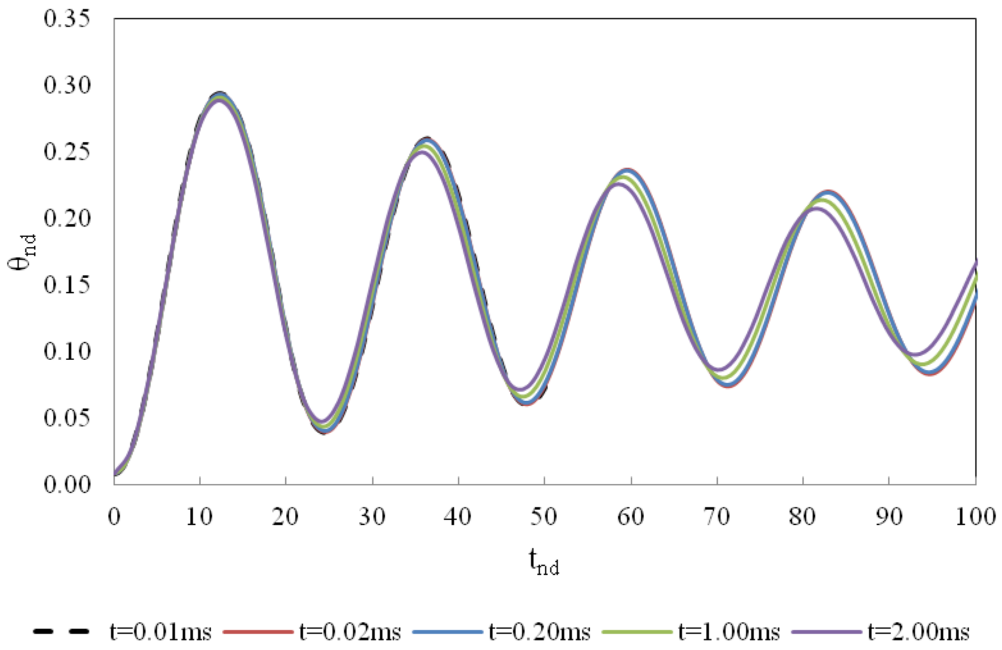

Figure 24. Non-dimensional Theta vs. Time at M = 0.3 for various timesteps utilized in 3FL-DYN

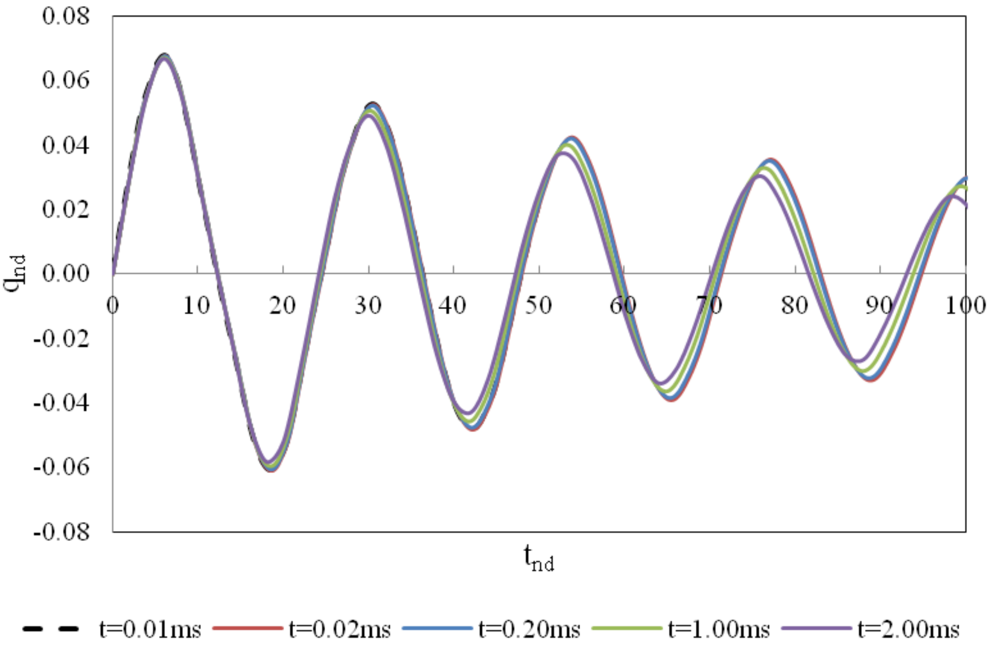

Figure 25. Non-dimensional *q* vs. Time at M = 0.3 for various timesteps utilized in 3FL-DYN

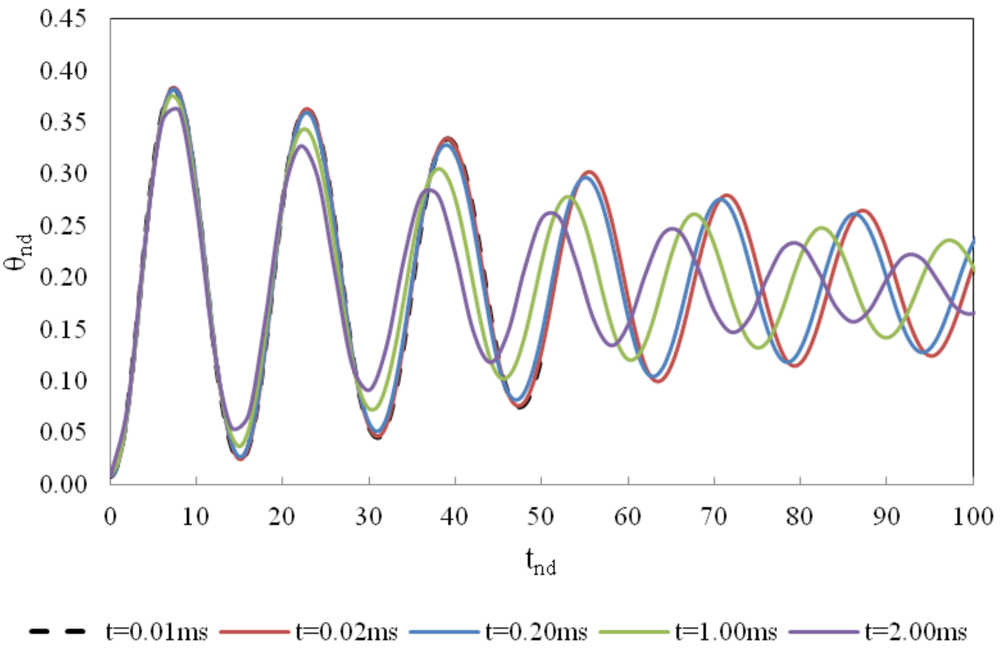

Figure 26. Non-dimensional Theta vs. Time at M = 0.6 for various timesteps utilized in 3FL-DYN

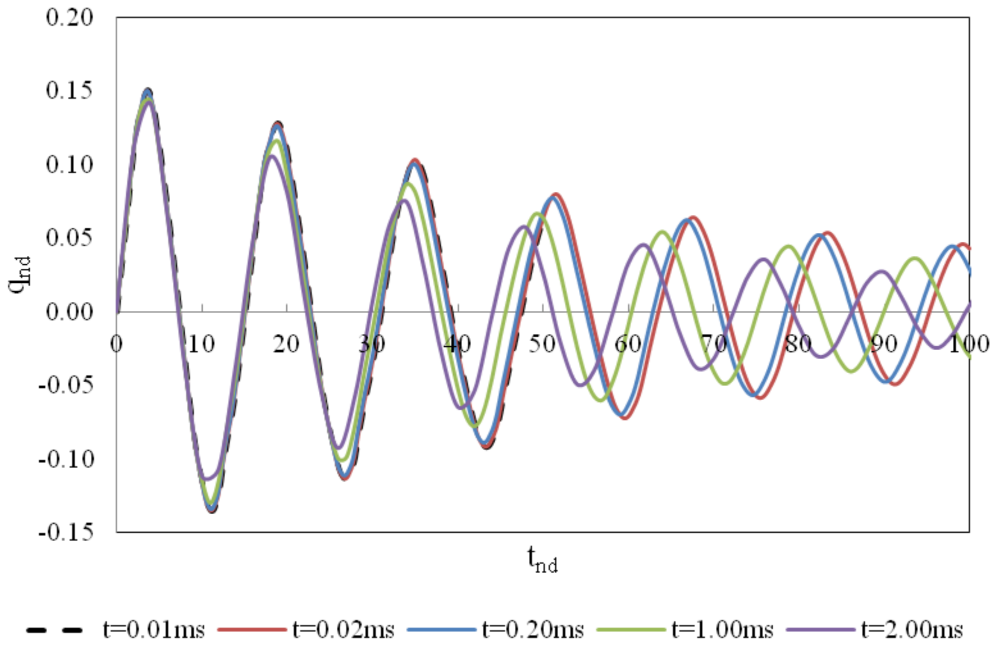

Figure 27. Non-dimensional *q* vs. Time at M = 0.6 for various timesteps utilized in 3FL-DYN

4.2.2 Time Step Selection for Transient CFD Analyses

Correct time step selection in transient CFD analyses is essential for the accuracy of the solution due to the fact that the time-integration of non-linear RANS equations is done utilizing the selected time step. For instance, Rumsey et. al [18] solved time-dependent flow around a 18% thickness arc airfoil and found out that drag and lift of the airfoil can change about 20% with a coarse time step size.

To select a suitable time step size for transient CFD analyses, solutions utilizing 6DOF motion were carried out at a statically unstable M = 0.6 case to evaluate the solution on the lateral direction in more detail. Fixed time steps of 0.02, 0.05, 0.2 and 0.5ms were used on the same boundary conditions described in Sections 3.2 and 4.5.1. Figure 28 to Figure 30 show the Euler angles (ϕ, θ, ψ) obtained from the transient 6DOF CFD solutions carried out at four different time step sizes.

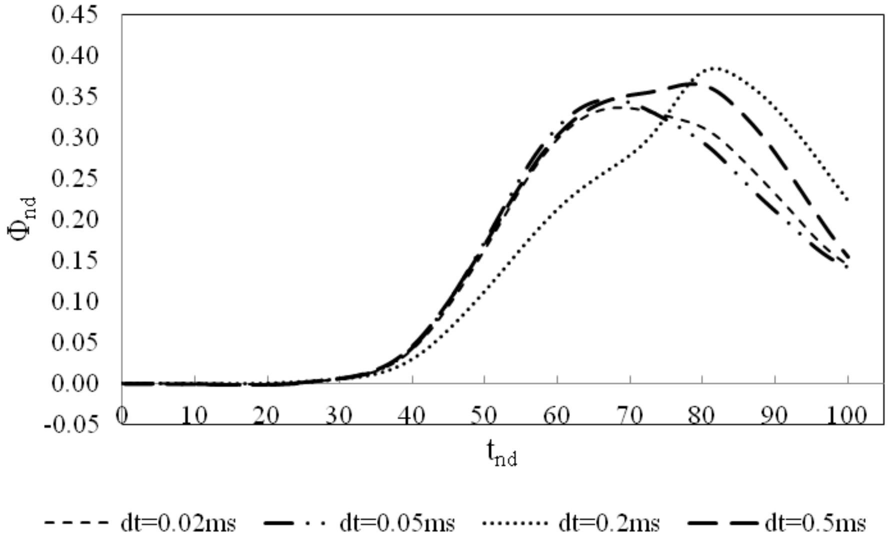

Figure 28. Non-dimensional Phi vs. Time at M = 0.6 for various timesteps utilized in transient 6DOF CFD

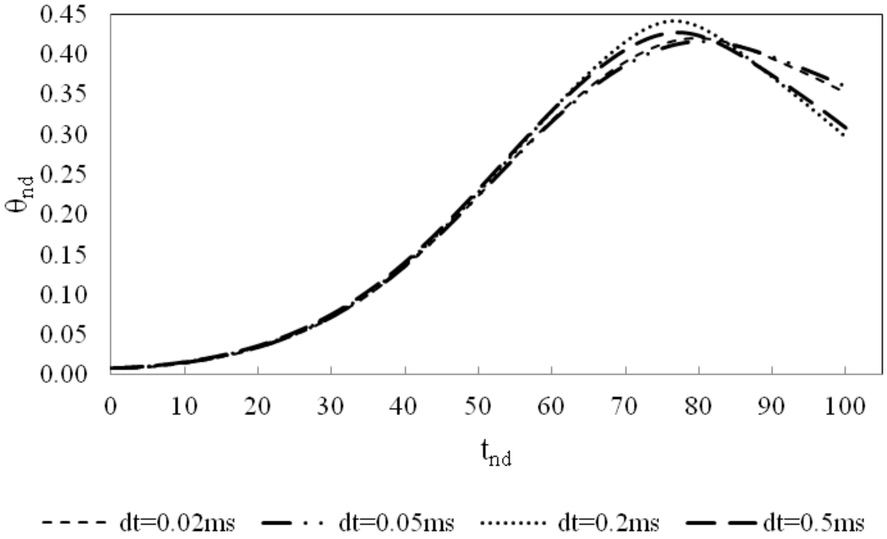

Figure 29. Non-dimensional Theta vs. Time at M = 0.6 for various timesteps utilized in transient 6DOF CFD

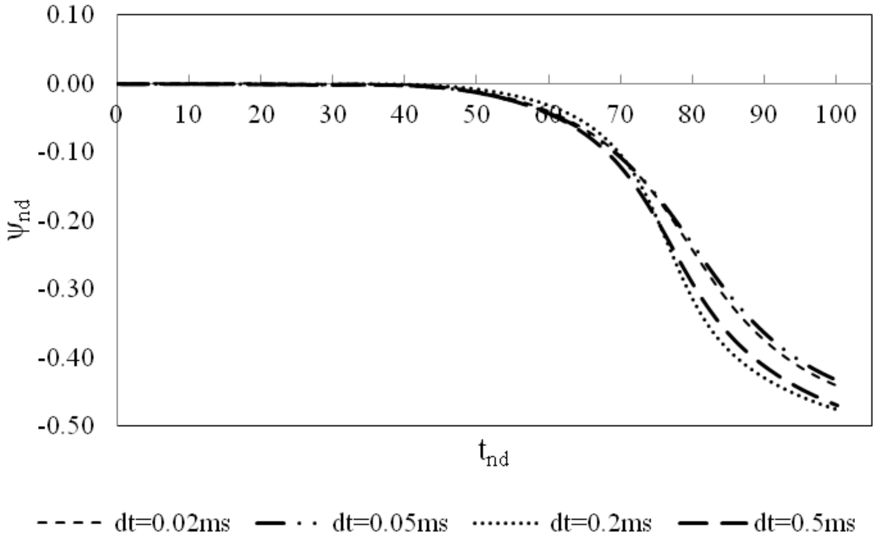

Figure 30. Non-dimensional Psi vs. Time at M = 0.6 for various timesteps utilized in transient 6DOF CFD

Due to the 3DOF nature of 3FL-DYN, the main Euler angle used for comparison in this study is going to be the pitch angle (θ). Taking the finest time interval of 0.02ms results as reference, when a comparison was done, the least difference occurs at a time interval of 0.05ms, which was 0.7% overall. For time intervals of 0.2ms and 0.5ms, the differences were found out to be 4.1% and 5.0% respectively. Taking the roll angle (ϕ) into account, for time intervals of 0.05ms, 0.2ms and 0.5ms, the differences were 5.4%, 27.7% and 9.6% respectively. For the yaw angle (ψ), they were 2.8%, 16.5% and 11.7%.

Based on these results, a time interval of 0.05ms was selected for all the transient CFD analyses carried out throughout the thesis. Taking the main Euler angle, the pitch angle, into account, the difference of 0.7% was deemed sufficient. Although there is 5.4% difference for the roll angle (ϕ), the transient CFD solution duration of the 0.02ms case is roughly 2.5 times of the 0.05ms time interval, which is about 3-4 weeks of solution time for transient 6DOF solutions. Hence, an optimization was made between calculation cost and solution accuracy in the lateral directions with the selection of a 0.05ms time interval.

4.3 PITCH DAMPING TERM REQUIREMENT IN 3FL-DYN

Pitch damping term denoted by $C_{M,q}$ is the derivative of the pitching moment C_M with respect to the pitching rate q. The term “damping” is used as an analogy of the effect of a damper in a spring-damper system. Ideally, if a spring system had no energy loss, it would oscillate forever. However; adding a damper to a spring system would dissipate the energy of the system and bring the oscillations to a stop. A damper dissipates energy utilizing a variety of methods such as viscous damping in mechanical systems, resistance in electronic oscillators, etc. [20]

For the case of a decoy in 6DOF flight, the damping could be due to viscous drag depending on the angles of attack and sideslip, the atmospheric conditions, the flow conditions etc. As damping relies on the rate of change of position (linear or rotational velocity etc.) for a mechanical system, damping terms written for a decoy in flight are dependent on the linear and angular velocities of the decoy.

As the decoy flight is modeled in 3DOF, there can only be nine damping terms which are $C_{D,u}$, $C_{L,u}$, $C_{M,u}$, $C_{D,w}$, $C_{L,w}$, $C_{M,w}$, $C_{D,q}$, $C_{L,q}$ and $C_{M,q}$. Owing to the fact that the aerodynamic coefficients are obtained as a function of Mach number and angle of attack, which is a function of u and w, the first six terms are inherently present in the 3DOF model. However, the last three terms depending on the pitching rate q are not. In Section 2.5, according to reference [8], $C_{D,q}$, $C_{L,q}$ terms are not deemed necessary for 3DOF decoy flight modeling.

In this study, initially the pitch damping term was not included in 3FL-DYN. However, the resulting model turned out to have insufficient and unphysical damping characteristics making it nearly impossible to find a configuration working effectively as a countermeasure against threats.

4.3.1 Obtaining the Pitch Damping Term

In order to obtain the pitch damping terms at different angles of attack and Mach numbers, CFD methodology is utilized. As explained in Section 2.5, [8] states that for 3DOF flight modeling, at identical angles of attack and Mach numbers, the moment coefficient varies linearly with pitching rate. The moment coefficients are obtained at a pitching rate of zero while the aerodynamic coefficients of the decoy are calculated. Hence, a transient CFD analysis with a constant pitching rate is going to yield the ΔC_M related to the pitching motion of the decoy. Dividing ΔC_M with the pitching rate utilized in the CFD analyses, the pitch damping term at different angles of attack and Mach numbers can be found.

For the methodology of transient CFD analyses with a constant pitching rate, the mesh motion feature of the commercial program FLUENT was used. Mesh motion feature is able to rotate and/or translate the defined zone with a constant rotational or translational velocity.

Differing from the boundary conditions defined in Section 3.2.3, there is an extra boundary condition called the interface. It was used to assert the pressure-farfield boundary condition without any effect on convergence and accuracy due to the rotation of the decoy. The domain is divided into two parts which are the rotating part called the inner domain and the non-rotating part called the outer domain, which can be seen from Figure 31. The pressure-farfield boundary condition was applied to the outer shell of the outer domain while the interface boundary condition was applied between the inner and outer domains. The reason behind the utilization of the interface boundary condition is the non-conformal mesh emerging from the rotation of the inner domain. With an interface, FLUENT is able to handle the non-conformal mesh. [14] The boundary condition on the wall of the decoy was again an adiabatic no-slip wall condition.

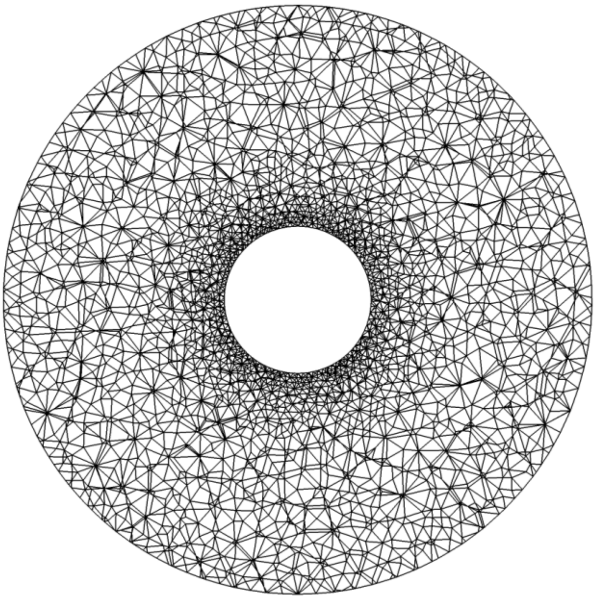

Figure 31. The outer domain solution mesh used for the interface boundary condition in FLUENT

The constant pitching rate utilized in the CFD analyses was obtained from the pitching rate value of the first-time step from 3FL-DYN, which is the highest pitching rate value the decoy is going to have throughout the motion. The constant time step used in the CFD analyses was 0.05ms, which is the same time step used for the transient 3DOF/6DOF CFD analyses explained in Section 4.2.2.

An example graph of the results of the CFD analyses carried out to obtain the pitch damping values at M = 0.3 for different angles of attack can be seen in Figure 32. The pitch damping coefficient remains almost constant until about 40° angle of attack, but from this point on at high angles of attack a sharp increase is observed. This proves useful for the damping of high magnitudes of oscillations.

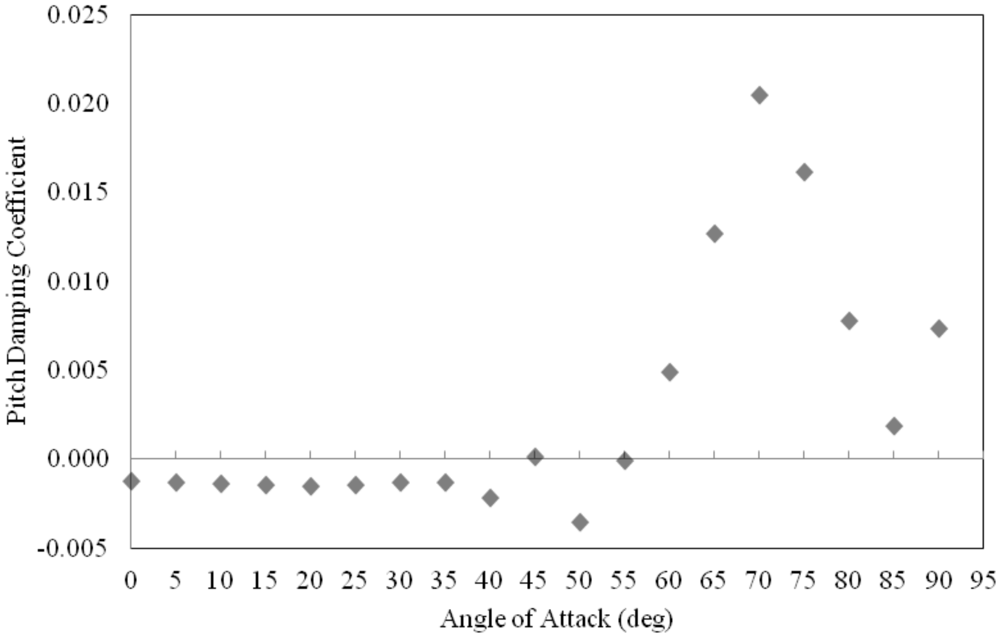

Figure 32. Pitch Damping Coefficient $C_{M,q}$ vs. Angle of Attack at M = 0.3

4.3.2 Evaluating the Effect of Pitch Damping

To evaluate the effect of pitch damping term, 3FL-DYN was run at M = 0.6, due to higher forces and moments for two different cases, emphasizing the differences. They are the cases with and without the pitch damping term $C_{m,q}$ obtained from the transient CFD analyses. For comparison purposes, the quantities most affected from the presence of $C_{M,q}$ term: pitch angle θ, pitching rate q and pitching acceleration $\dot{q}$, are plotted with respect to time, which can be seen from Figure 33 to Figure 35.

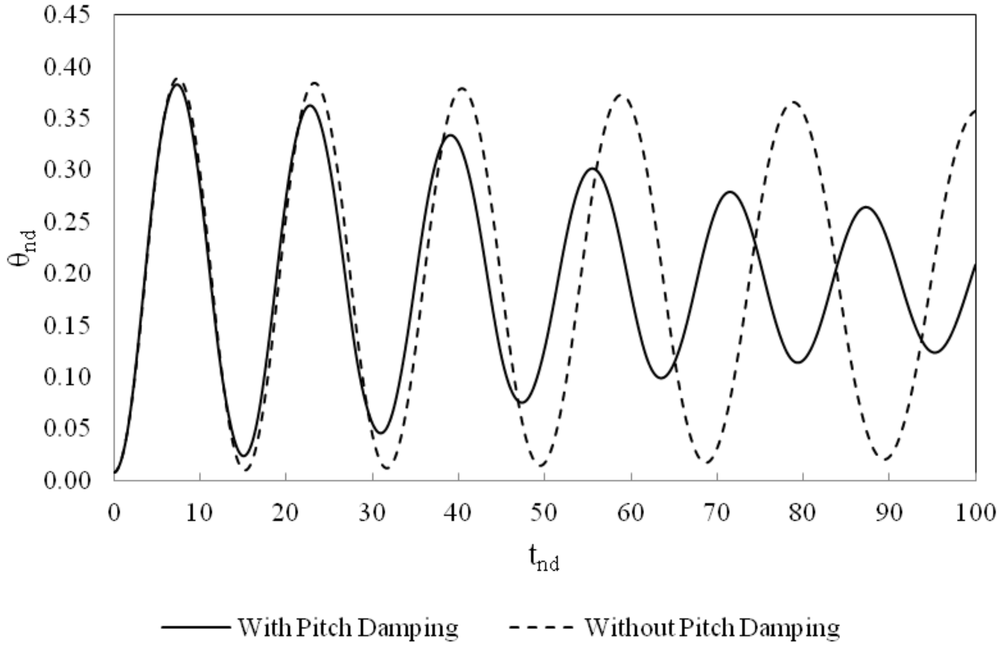

Figure 33. Non-dimensional Theta vs. Time at M = 0.6 for the evaluation of the pitch damping term $C_{M,q}$ utilized in 3DOF numerical implementation

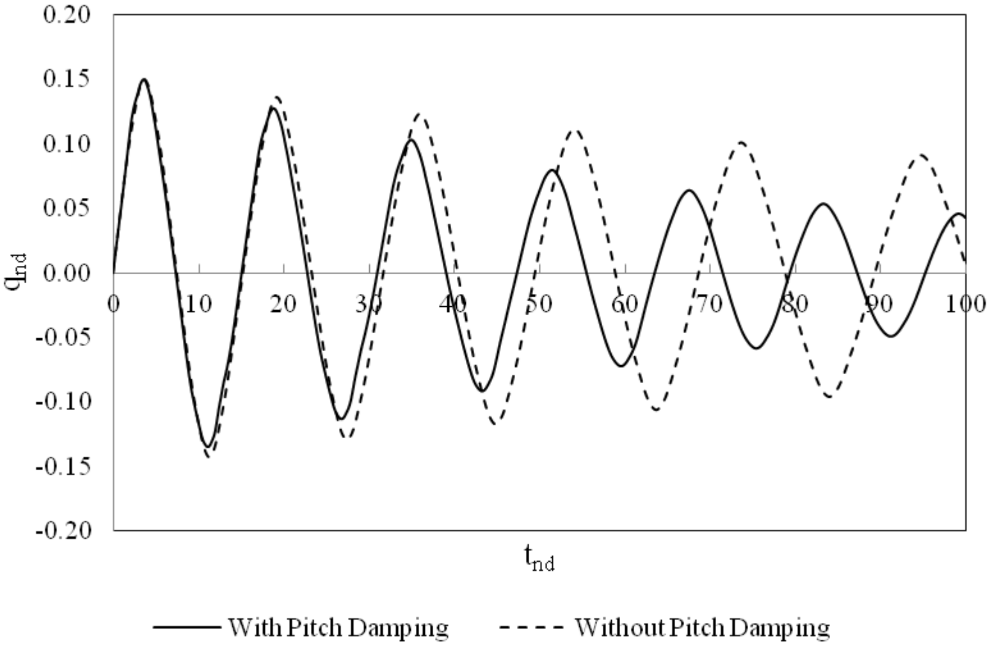

Figure 34. Non-dimensional q vs. Time at M = 0.6 for the evaluation of the pitch damping term $C_{M,q}$ utilized in 3DOF numerical implementation

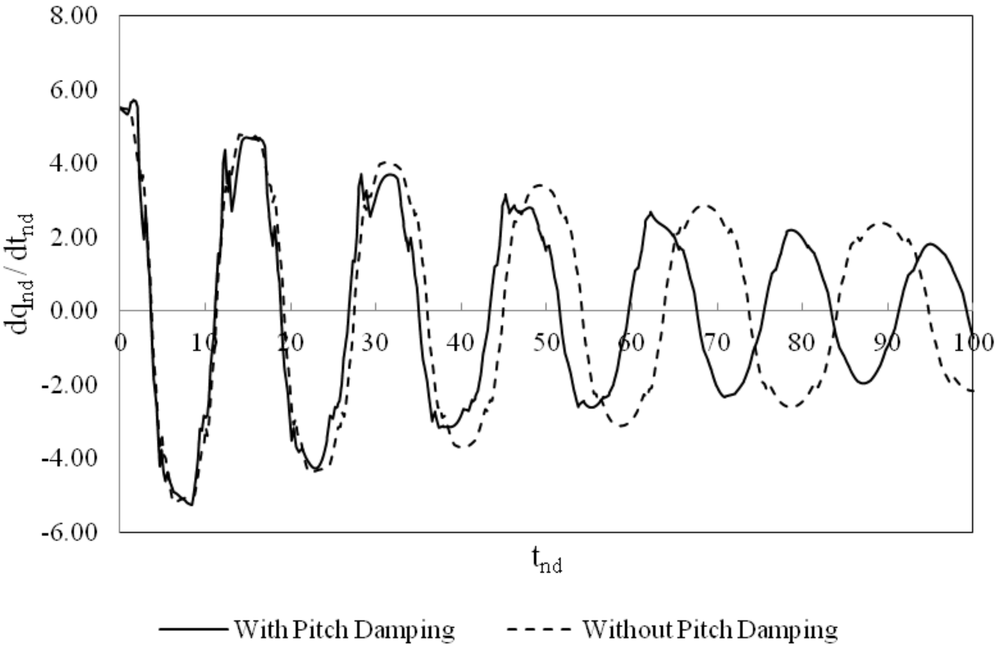

Figure 35. Non-dimensional $\dot{q}$ vs. Time at M = 0.6 for the evaluation of the pitch damping term $C_{M,q}$ utilized in 3DOF numerical implementation

When the results are compared, it is observed that both cases are underdamped; as the magnitude of the oscillations are decreasing as time progresses. The reason of damping in the case without pitch damping term is due to other terms like $C_{D,u}$, $C_{L,u}$, $C_{M,u}$ etc. However, when the rate of decrease in the magnitude of the oscillations are concerned, the model with pitch damping derivative is superior due to the fact that the oscillations observed in all figures are decreasing in an increasing rate. Addition of pitch damping derivative proves to be most effective on the pitching rate with a difference of about 60% between the initial and final time steps.

For the design of a decoy of which the orientation is essential, the oscillations obtained from the model without pitch damping is going to be make the overall countermeasure design process harder. Because, coming up with an effective configuration against threats is going to be harder. Moreover, taking the results given in Chapter 5 into account, the case with the pitch damping derivative was found out to be closer to the transient CFD results.

4.4 GRID INDEPENDENCE

In CFD applications, in order for the solution to be accurate, the grid used in the problem should not affect the solution to unacceptable levels. In other words, the solution has to be grid independent. The effect of the grid on the solution might occur in various ways. For instance, for a very coarse domain mesh due to insufficient resolution of the eddies created by the geometry, the diffusion of the turbulent parameters might be unnaturally faster. As an example, Karcz et al. [21] found out that distribution of the kinetic energy and its dissipation is significantly affected by the density of the computational grid for their test case of an agitated vessel resulting underestimated local velocity values.

To evaluate the grid independence of the solution, four different grid sizes were solved with the exact same conditions specified in Section 3.2. The comparisons of these grids in terms of drag, lift and pitching moment coefficients at five different angles of attack can be seen from Figure 36 to Figure 38. At high angles of attack achieving better accuracy of the forces and moments calculated is going to be harder. Therefore, the angle of attack values were chosen to be relatively high angle of attack values to better evaluate the accuracy of the solution. Table 2 shows the sizes of the different grids utilized in the grid independence study in terms of decoy surface and domain mesh size.

Table 2. The different grid sizes used for the grid independence study

	Surface mesh size (# elements)	Domain mesh size (# elements)
Grid 1	32856	1126275
Grid 2	71434	1744834
Grid 3	104986	2798373
Grid 4	141498	3667583

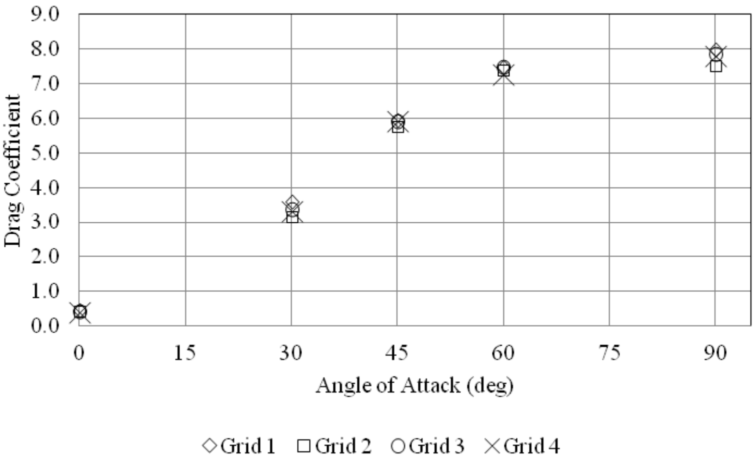

Figure 36. Drag coefficient comparison of four different grid sizes

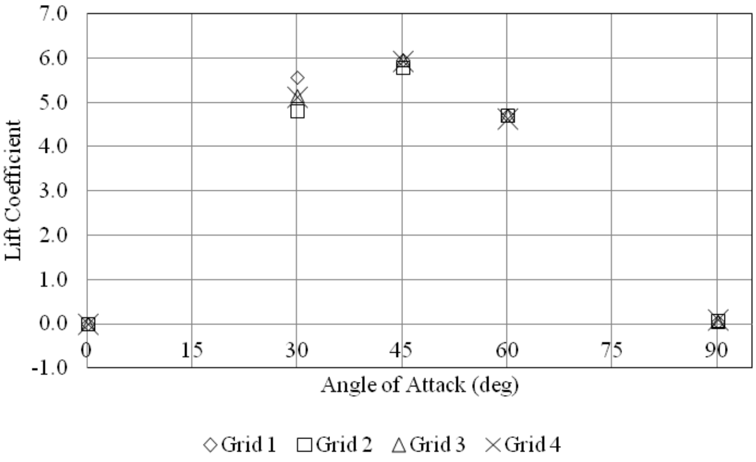

Figure 37. Lift coefficient comparison of four different grid sizes

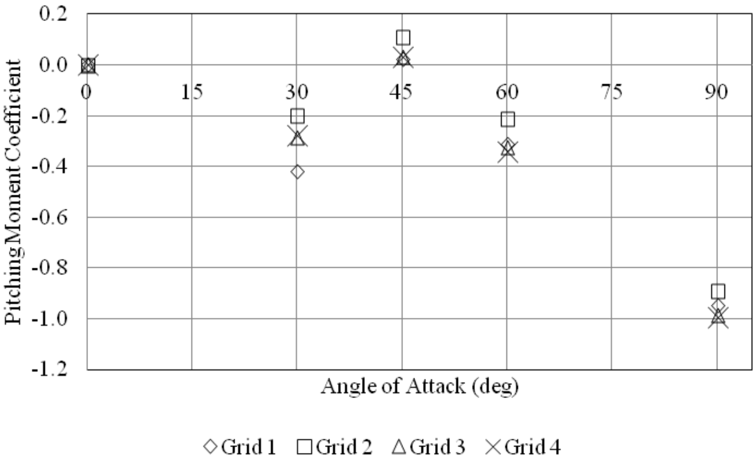

Figure 38. Pitching moment coefficient comparison of four different grid sizes

Taking the results of Grid 4 as the reference values, comparison between the results reveals that for the drag coefficient values the differences between the grids are less than 3% except Grid 1. The largest differences for the lift coefficient values occur at 30° angle of attack which are 8.9% for Grid 1, 5.9% for Grid 2 and 0.8% for Grid 3. At pitching moment coefficient values, the highest differences between the grids occur. The moment coefficient is dependent on the overall pressure distribution around the decoy different than the drag and lift coefficients. For instance, two identical decoys with different pressure distributions can have the same drag coefficient but cannot have the same moment coefficient. As can be observed in Figure 38, Grid 1 and Grid 2 are very different from the results of Grid 4. For Grid 3 however, the largest difference is found out to be 3.5% occurring at 60° angle of attack.

According to these results, Grid 3 was used for all the steady and transient CFD analyses carried out throughout the thesis. Due to the fact that Grid 3 has 23.7% less number of elements compared to Grid 4 and a largest error of 3.5% occurring at very high angles of attack, it is evaluated to be an optimization of solution accuracy and calculation cost, especially for the 6DOF transient CFD analyses explained in Chapter 5 considering the calculation times are measured in days / weeks.

4.5 EVALUATION OF THE 3DOF ASSUMPTION

In Section 2.4, the reasons for adopting a 3DOF approach were discussed. Before carrying out the runs for the whole 6DOF analysis matrix, the validity of the 3DOF assumption should be checked. To evaluate the 3DOF assumption, the CFD solution of two different cases, one of which is 3DOF and the other 6DOF, is compared in terms of trajectory, angle, velocity, acceleration, forces and moments.

4.5.1 3DOF / 6DOF Solution Methodology

CFD methodology with FLUENT was utilized for the calculation of 3DOF / 6DOF motion of the decoy with the flowfield. The analysis conditions were similar to the conditions described in Section 3.2, with two basic differences: the dynamic mesh model and the pressure-farfield boundary condition. The same grid explained in Section 3.2.5 was utilized.

For 3DOF / 6DOF motion applications, FLUENT is able to remesh and smooth the volume mesh around the geometry or move the entire domain utilizing the equations of motion, with the dynamic mesh model. The calculations were done and outputs, such as Euler Angles were given in the inertial frame. [14]

FLUENT does not have a feature to model the motion of the body in 3DOF. Hence, to achieve 3DOF motion, the inertia values except the mass moment of inertia in the pitching axis were taken as very unrealistically high values. This prevents angular motion in roll and yaw axes. As there is no initial velocity in lateral direction, there is no translational motion as well.

The problem is not a safe-seperation problem, so there is no relative motion between two bodies. Because of this fact, there is no need to remesh or smooth the domain mesh around the decoy as its motion progresses. In addition, it is going to increase the computational calculation time of the solution. To avoid this situation, the whole domain around the decoy moves according to the translational and rotational velocities around the decoy. In other words, it is different than the usual methodology of CFD analyses in where the domain and the geometry is fixed and there is flow velocity on the domain like a wind tunnel. To achieve this, the boundary condition on the outside of the domain, which is a pressure-farfield boundary condition should have zero relative velocity.

The time step used in this analyses were based on the time step selection study discussed in Section 4.1, which was a time step of 0.05ms.

4.5.2 Comparison of 3DOF / 6DOF Motion

The analyses were done for two different center of gravity values CG1 and CG2 at Mach numbers of 0.3 and 0.6. At CG1 cases, the decoy does not have static stability, while at CG2 cases, the decoy does. The static stability of the decoys was evaluated with the preliminary calculations done with 3FL-DYN. A statically unstable case was selected in order to evaluate the validation of the 3DOF assumption for this case as well. The pitching angle (θ) of the decoy were used for comparison purposes.

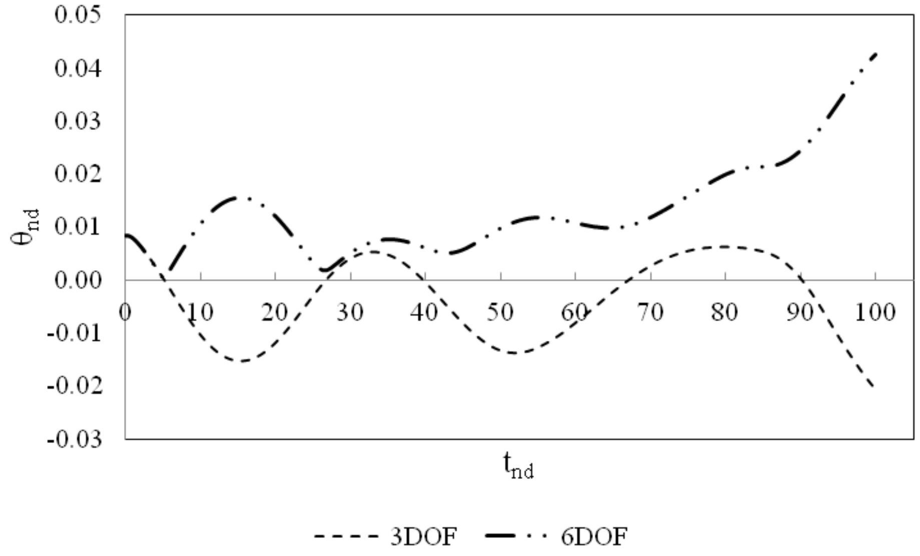

Figure 39. Non-dimensional Theta vs. Time 3DOF / 6DOF comparison for M = 0.3, CG1

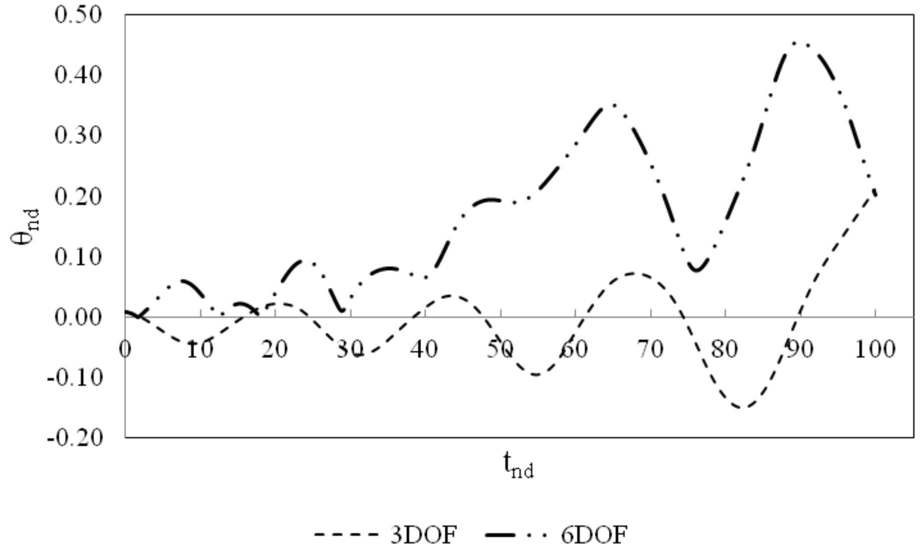

Figure 40. Non-dimensional Theta vs. Time 3DOF / 6DOF comparison for M = 0.6, CG1

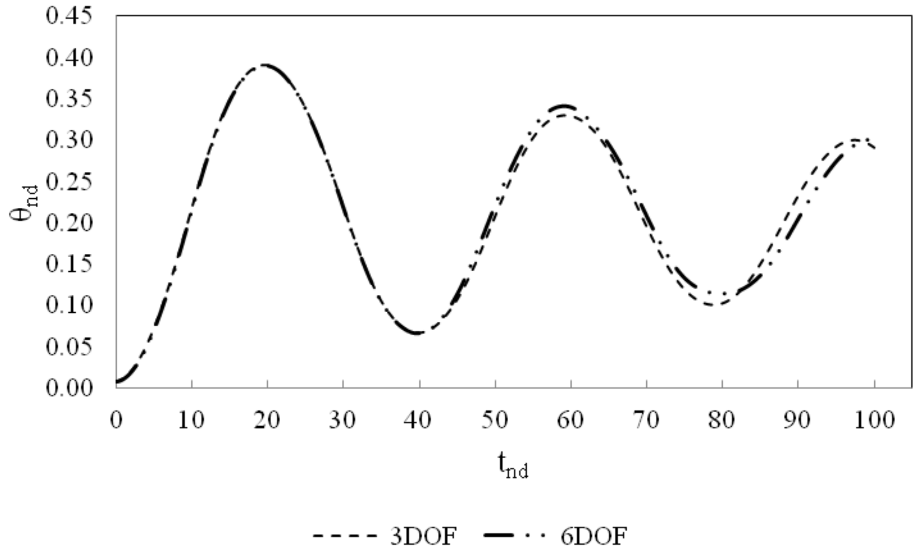

Figure 41. Non-dimensional Theta vs. Time 3DOF / 6DOF comparison for M = 0.3, CG2

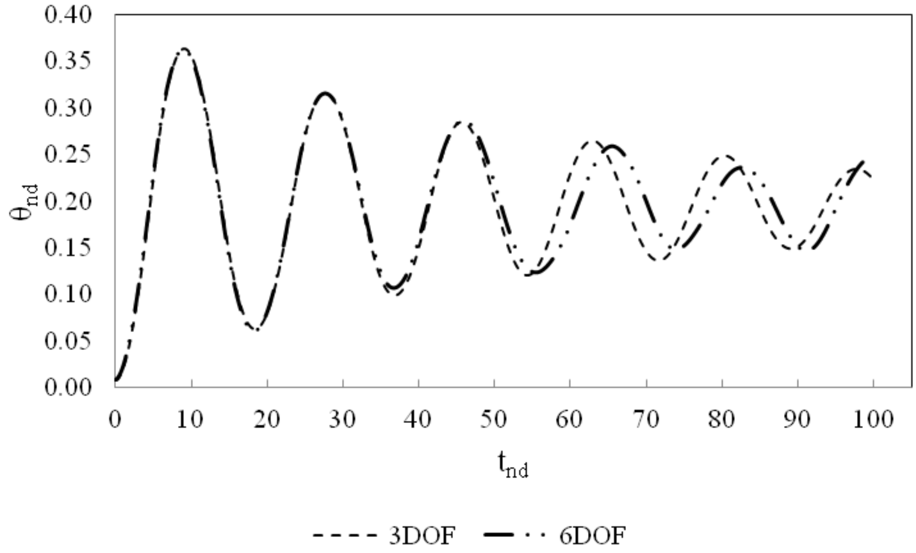

Figure 42. Non-dimensional Theta vs. Time 3DOF / 6DOF comparison for M = 0.6, CG2

The 6DOF results of the statically unstable case (CG1) were found out to be very different from the 3DOF results for both Mach numbers. The behavior of the decoy, the magnitude and frequency of the oscillations are not consistent. This is the consequence of the yawing and rolling in 6DOF motion, which can be seen from Figure 43 and Figure 44 for M = 0.6 case. Patel et al. [22] state that according to the wind tunnel results even if the angle of sideslip is zero, due to asymmetrical vortex shedding, at high angles of attack large side forces and dynamic out-of-plane loadings may occur, resulting in a yawing motion. As high angles of attacks occur during the pitching motion, a rolling motion is inevitable with the coupling of yawing and pitching motion for the decoy. This is due to the smaller mass moment of inertia in the roll axis for slender bodies. However, for the statically stable case, the results were found out to be very similar for both Mach numbers. They were not expected to be on top of each other, which is again due to the effect of 6DOF motion (Figure 45) resulting in a rolling motion, but the trends of the oscillations are consistent. The effect of rolling motion of the statically stable decoy is similar to that of a roll-stable missile, which utilizes the conservation of angular momentum for lateral stability during flight. [25] Considering the yawing motion, it is observed that the magnitude of the oscillations is one quarter of the magnitude of pitching oscillations and start to diminish after a certain time. (Figure 46)

It is understood that in order for the 3DOF assumption to work effectively, the cases investigated should have static stability. In the nonexistence of static stability, the motion in the lateral direction is dominant proving the 3DOF assumption invalid.

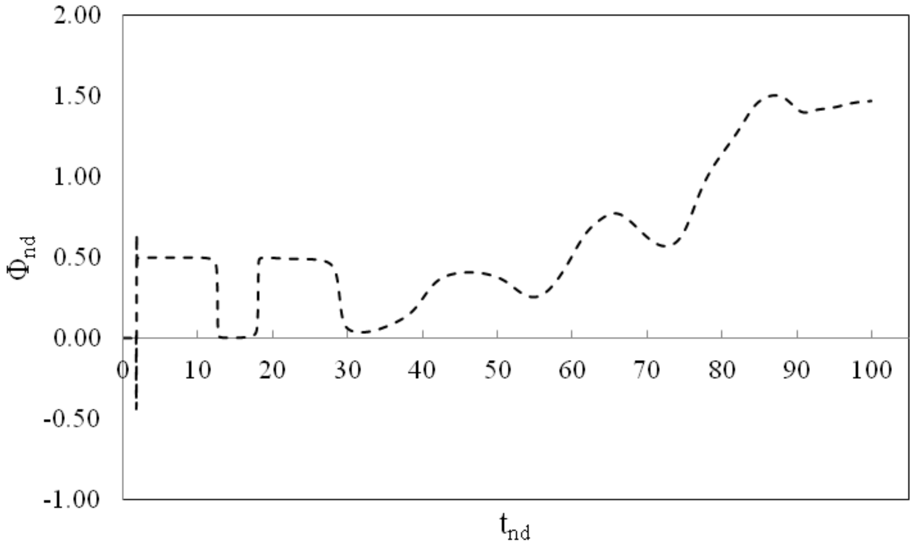

Figure 43. Non-dimensional Phi vs. Time of 6DOF motion for M = 0.6, CG1

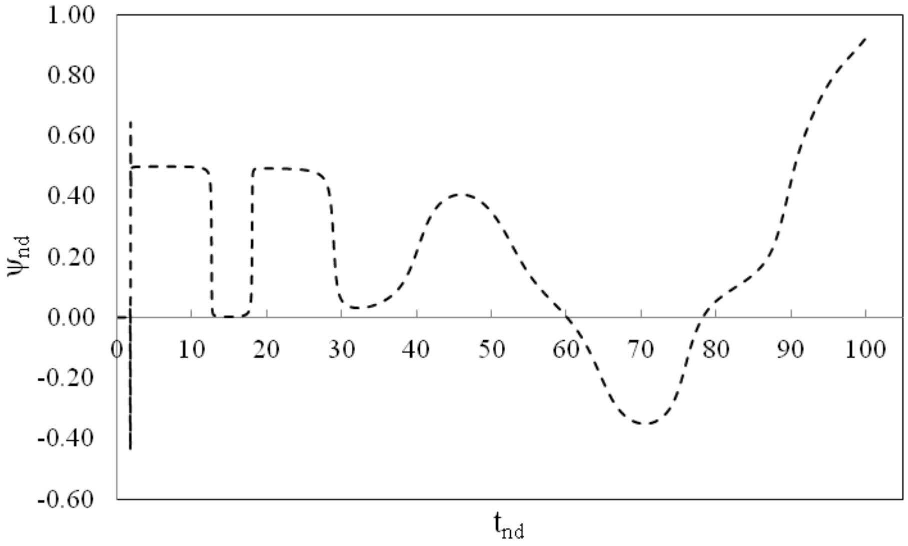

Figure 44. Non-dimensional Psi vs. Time of 6DOF motion for M = 0.6, CG1

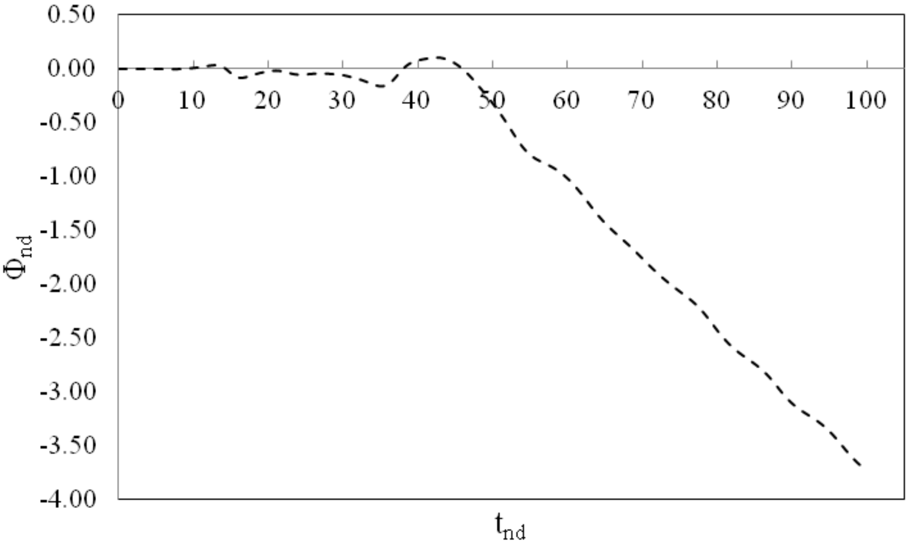

Figure 45. Non-dimensional Phi vs. Time of 6DOF motion for M = 0.6, CG2

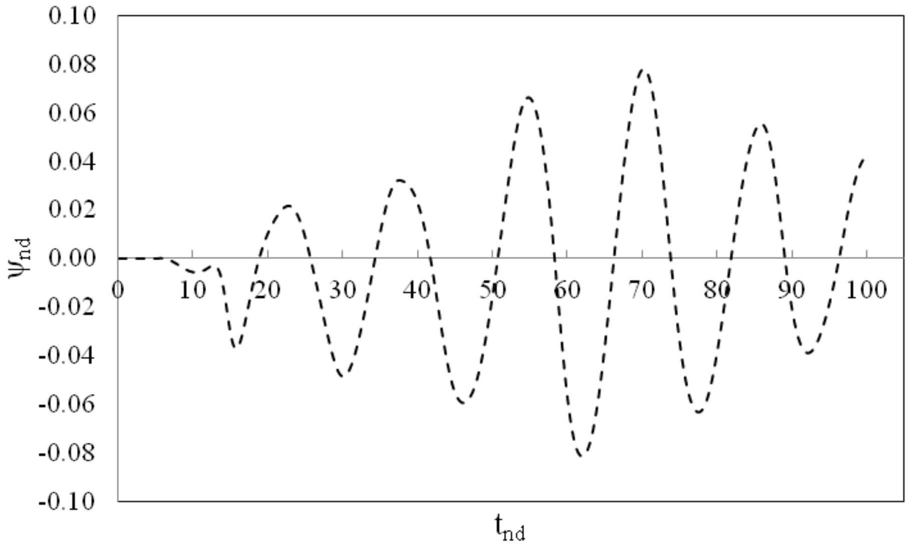

Figure 46. Non-dimensional Psi vs. Time of 6DOF motion for M = 0.6, CG2

CHAPTER 5

RESULTS AND DISCUSSIONS

In this chapter, the results obtained from 3FL-DYN are compared with those of transient 6DOF CFD analyses. 3FL-DYN's ability to capture the effects of the variation of center of gravity, Mach number and tail sizes is investigated.

5.1 ANALYSIS CONDITIONS

The relevant analysis parameters / conditions required (boundary conditions, time step size etc.) for the 6DOF FLUENT CFD analyses discussed in Sections 3.2, 4.1, 4.4 and 4.5.1. To ease the reader, all relevant parameters are gathered together and summarized here in Table 3.

Table 3. The analysis conditions

Boundary Conditions	Pressure-Farfield (domain) Adiabatic No-slip Wall (decoy)
Turbulence Model	Realizable k-epsilon
Air	Compressible Ideal-Gas
Solver Approach	Pressure-Based Coupled
Discretization	Second-Order, Green-Gauss Node Based
Grid Size	2798373 cells (Tail = 100% case)
First Layer Thickness (mm)	0.1
# of Prism Layers	11
Motion Model	Dynamic Mesh model with 6DOF
Time Step (ms)	0.05

The analysis matrix consists of two center of gravity positions, three Mach number and two different tail sizes, which can be seen in Table 4. Considering the cross-matching of all the combinations of these analyses, in order not to overwhelm the reader, the results are given here for a selected reference case. This case is the most probable configuration and flight condition used for the decoy design. The results of all the other cases are given in APPENDIX A.

As explained in Section 2.6.2, the center of gravity of the decoy is measured from half of the length of the decoy (positive direction pointing towards the nose of the decoy) and given as the percentage fraction of the length. For instance, CG = 15% means that the center of gravity of the decoy is $0.15\ l$ front of the half length of the decoy. Tail size is varied by changing the chord of the tail and given as a percentage of the tail size of the reference case. For the analysis matrix, apart from the values for the reference case, a center of gravity and a tail size value which are going to reduce the static stability of the decoy were selected considering the static stability discussion in Section 4.5.2. All the cases have longitudinal static stability and have the same initial conditions in terms of altitude and attitude. For Tail = 80% case, a whole new set of time-independent CFD analyses were done with the conditions given in Sections 3.2 and 4.3.1.

Taking this information into account, the reference case has a Mach number of 0.6, CG position of 30% and a tail size of 100%. For the investigation of every variable, the pitch angle (θ), and the trajectories were compared with each other to observe the differences between the 3FL-DYN and 6DOF CFD analyses. In addition, to observe the trends more clearly, the results of 3FL-DYN for different variables and the results of the 6DOF CFD are plotted seperately. Moreover, pressure and Mach number distributions around the decoy at different times are given. For flowfield visualization, FieldView and Tecplot software which have the capability to draw streamlines, shear lines, pressure distributions etc. were used. [23, 24]

Table 4. The analysis matrix

<table>
<tr><td>Mach Numbers</td><td colspan="2">0.30</td><td colspan="2">0.45</td><td colspan="2">0.60</td></tr>
<tr><td>Center of Gravity (CG)</td><td colspan="3">10 %</td><td colspan="3">30 %</td></tr>
<tr><td>Tail Size</td><td colspan="3">80 %</td><td colspan="3">100 %</td></tr>
</table>

5.2 CENTER OF GRAVITY EFFECT

To investigate the ability to capture effect of center of gravity position, two center of gravity positions of 10% and 30% were analyzed at every Mach number and tail size in the analysis matrix. For convenience, effects of the center of gravity locations at M = 0.6, Tail size = 100% condition was thoroughly examined in this section. The results of the other cases individually can be seen from APPENDIX A.

From Figure 47 to Figure 50, pitch angles (θ) obtained from two methodologies at two center of gravity locations were plotted with respect to time. To ease the reader, plots are organized so that either the methodologies (Figure 47, Figure 48) or either the effect of c.g. position are compared. (Figure 49, Figure 50)

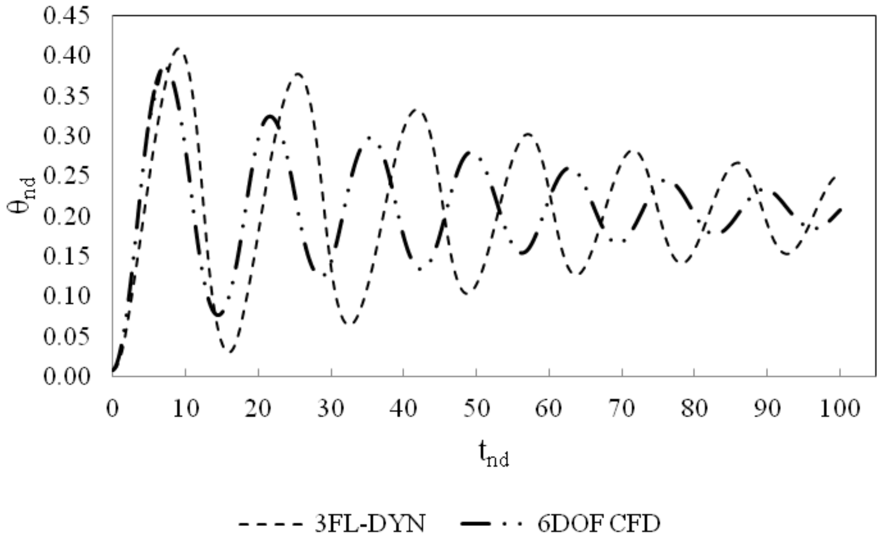

Figure 47. Non-dimensional Theta vs. Time 3FL-DYN / 6DOF CFD comparison for M = 0.6, CG = 30%, Tail = 100%

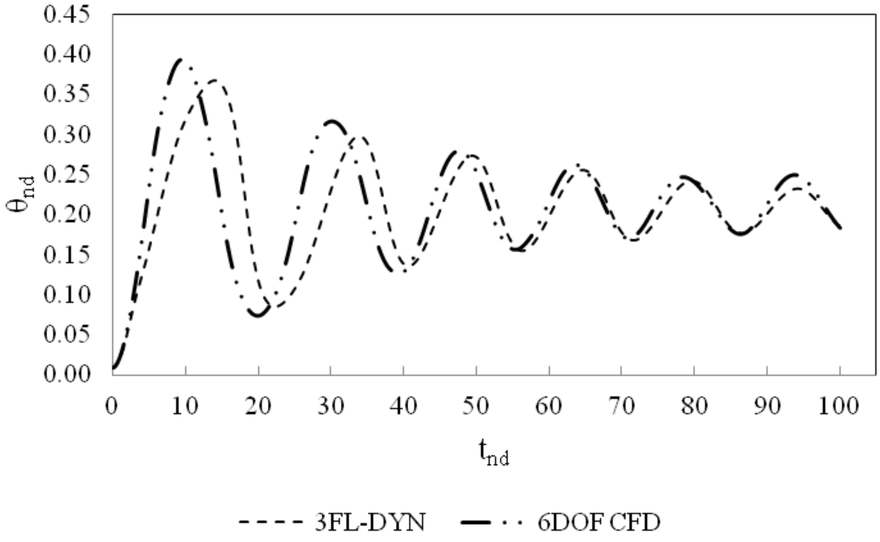

Figure 48. Non-dimensional Theta vs. Time 3FL-DYN / 6DOF CFD comparison for M = 0.6, CG = 10%, Tail = 100%

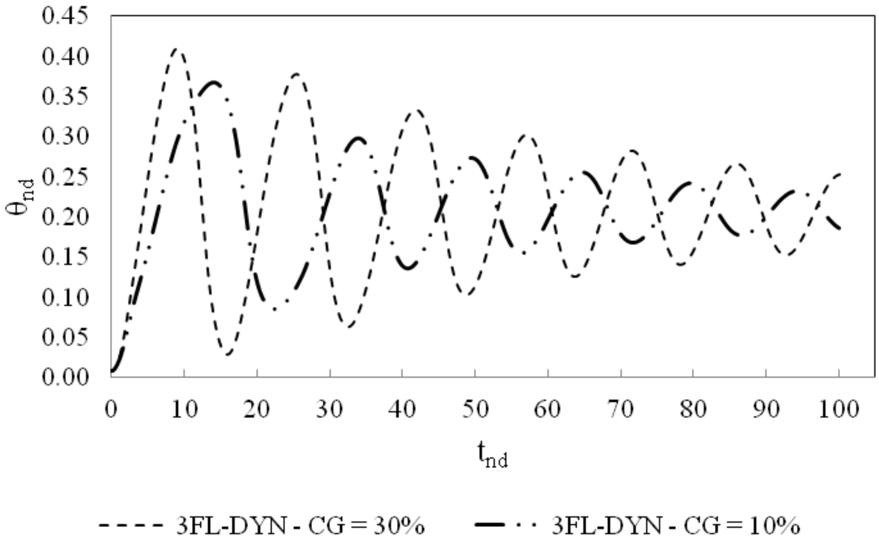

Figure 49. 3FL-DYN Non-dimensional Theta vs. Time comparison of two center of gravity values for M = 0.6, Tail = 100%

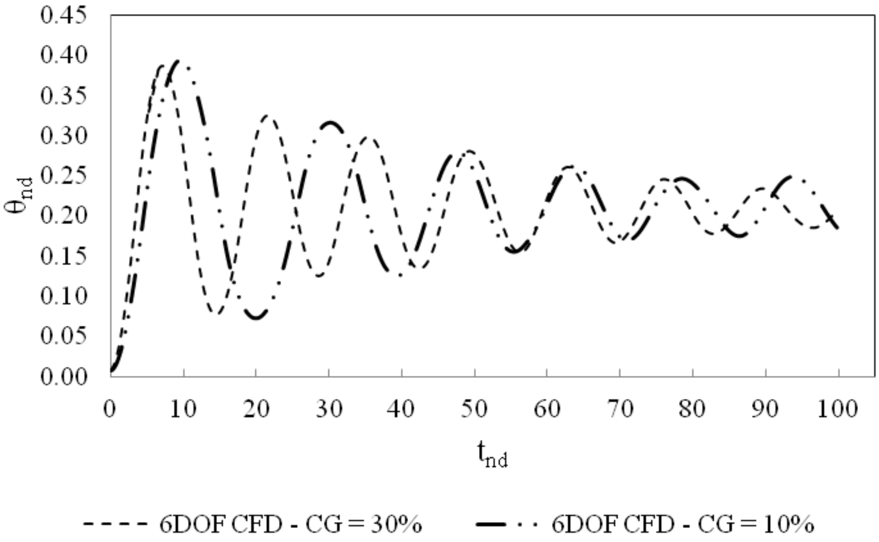

Figure 50. 6DOF CFD Non-dimensional Theta vs. Time comparison of two center of gravity values for M = 0.6, Tail = 100%

Comparing the 3FL-DYN with the 6DOF CFD results, it is obvious that for the CG = 10% case the results are closer. This is due to the fact that initially as the decoy has a high angle of attack, CG = 30% case has a higher moment arm compared to the CG = 10% case for the pitching moment resulting in higher accelerations in the pitching direction hence higher frequency of oscillations.

Trendwise, 3FL-DYN was able to capture the higher frequency of the oscillations for the CG = 30% case. But as 6DOF CFD was able to dissipate more energy by damping mechanisms in the lateral directions, the magnitude of the oscillations decreases more rapidly as well as the frequency. As damping is dependent on the rate of change of position in the motion, the higher accelerations in CG = 30% case causes this situation, which is benign for the CG = 10% case. The 3DOF method is more conservative for initial design purposes owing to the fact that the frequency and the magnitude of the oscillations are greater than that of the 6DOF CFD results.

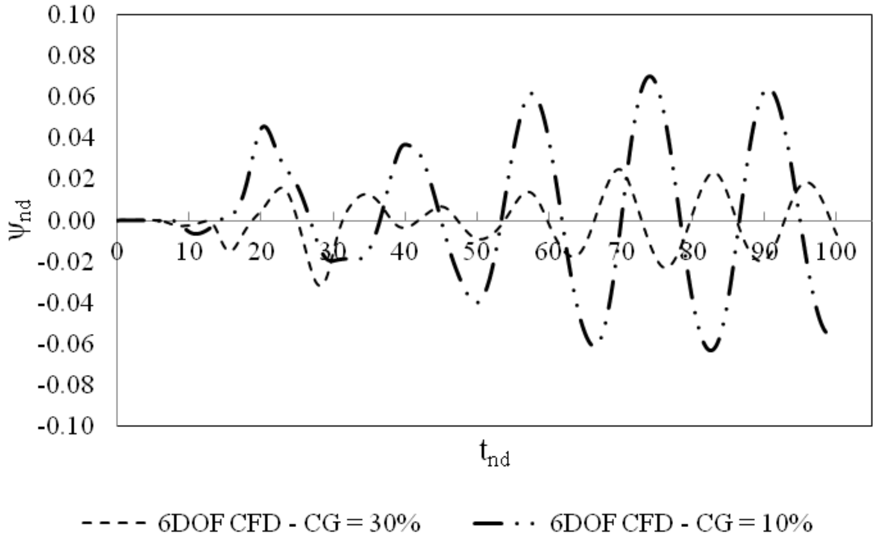

Figure 51. 6DOF CFD Non-dimensional Psi vs. Time comparison of two center of gravity values for M = 0.6, Tail = 100%

In Figure 51, the lateral motion in the yaw direction can be observed. All of the cases have continuous rolling motion as can be seen from APPENDIX A. The lateral motion is caused by the asymmetrical vortex shedding occurring at high angles of attack as explained in [22]. As the decoy is a slender body, its mass moment of inertia in the roll direction is about one order of magnitude less than the mass moment of inertia values in pitch and yaw directions. This fact leads to a continuous motion in the roll axis for both CG values, just like a roll-stabilized missile. There is motion in the yaw direction for both cases, but the highest magnitude of the oscillations is about 5-6 times smaller than that of the pitching motion. Higher magnitude of oscillations in the yaw direction are observed for the CG = 10% case as expected because of lower correcting yaw moments.

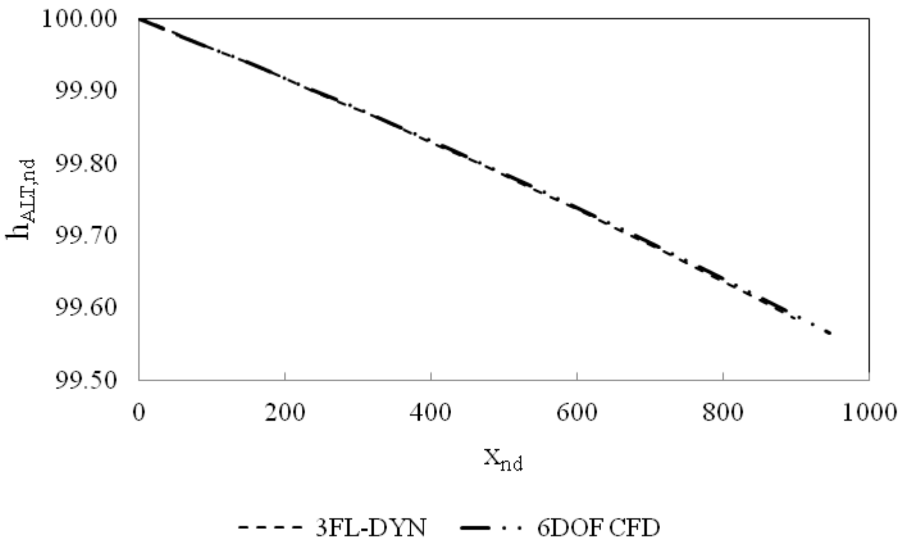

Figure 52. 3FL-DYN / 6DOF CFD Trajectory Comparison for M = 0.6, CG = 30%, Tail = 100%

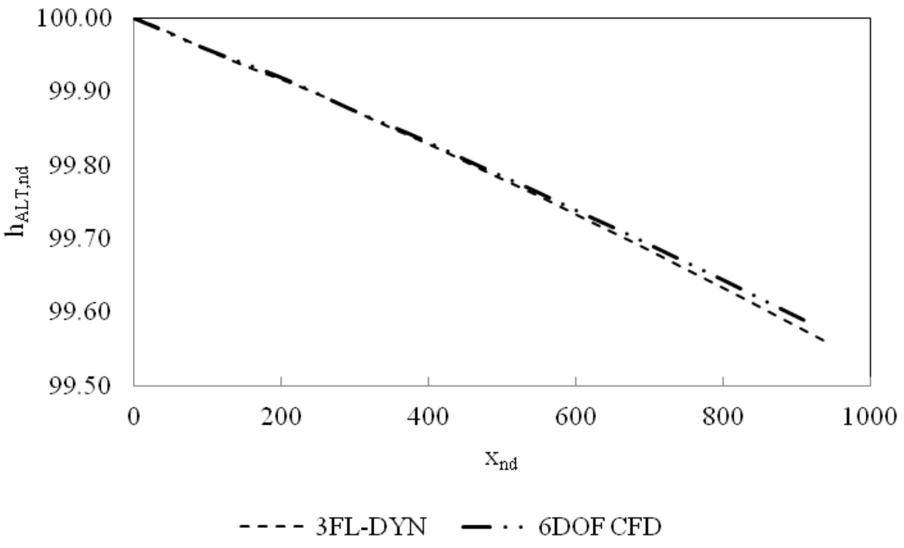

Figure 53. 3FL-DYN / 6DOF CFD Trajectory Comparison for M = 0.6, CG = 10%, Tail = 100%

For both cases, the trajectory of the decoy was captured very well by the 3FL-DYN which can be seen from Figure 52 and Figure 53. Translation in lateral direction is not comparable to that of the longitudinal direction.

Visualization of the motion history of the decoy at two different center of gravity values obtained from 6DOF CFD analyses is given in Figure 54, in where the decoy is colored with the gage pressure values. Starting from the initial time point, the motion history is given with a non-dimensional time interval of 10 as well. The tail portion of the decoy was made transparent to ease the observation of the pressure distribution on the decoy. The horizontal and vertical distances covered by the decoy is scaled down to 2.5%, while the decoy itself is not scaled. More dominant yawing motion of the CG = 10% case as well as the rolling motion for the both cases can be observed from the motion history. Besides, the higher pressures seen on the direction to where the decoy moves shows the yawing correction made by the decoy, while the lower pressures (blue) at higher pitch angle positions shows a separation around that region indicating a high angle of attack value for the decoy. The lower pressures start to diminish as the time marches on, implying the stabilization of the decoy.

The comparisons of pitch angles, trajectories as well as the flowfield for center of gravity values at different Mach numbers and tail sizes are proved to be coherent with the results explained above. These results are given in APPENDIX A.

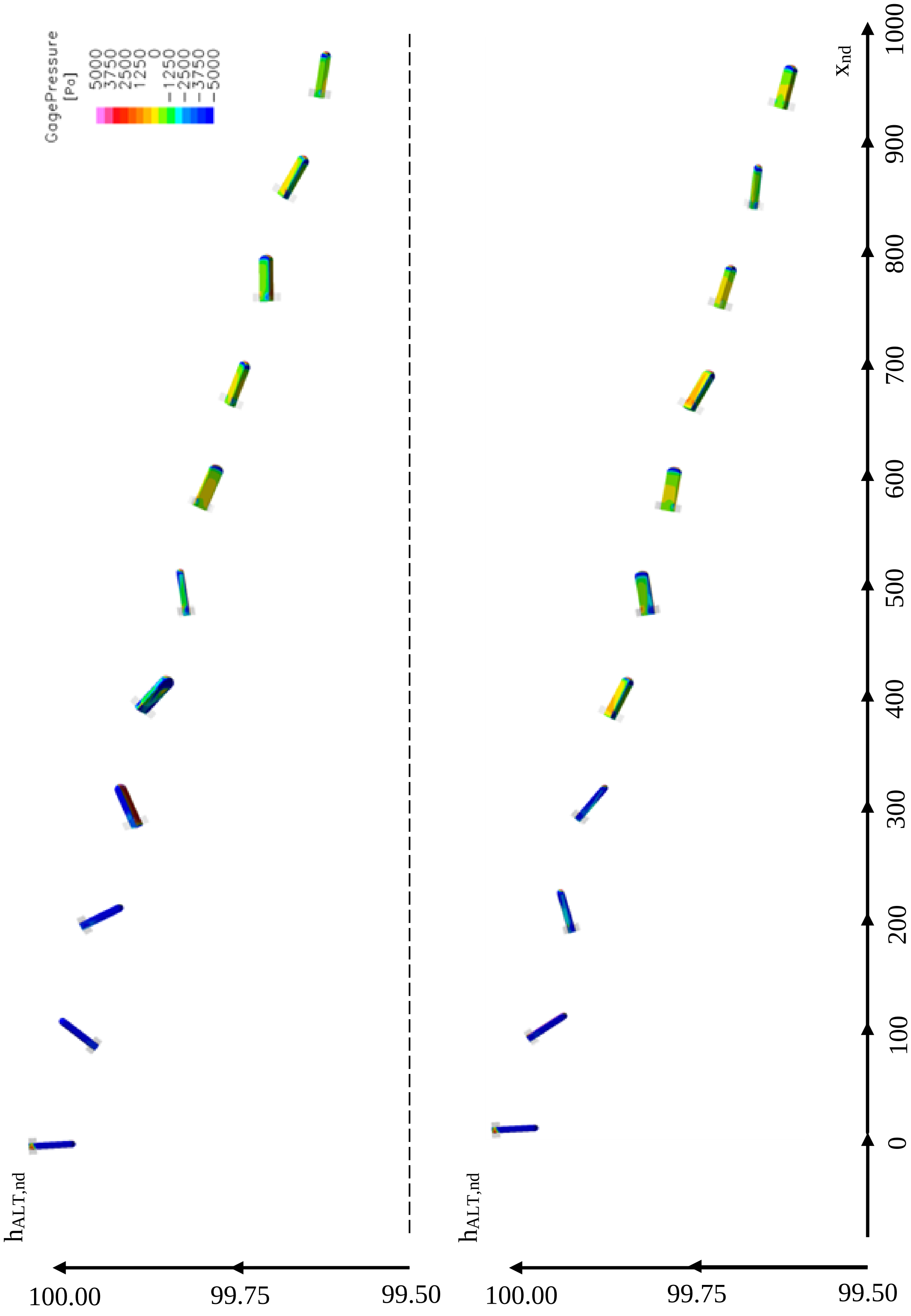

Figure 54. Motion history of the decoy at different time points with 10 non-dimensional time interval obtained from 6DOF CFD analyses colored with the pressure distribution around the decoy for two different center of gravity values for M = 0.6, Tail = 100% (CG = 10% : Left, CG = 30% Right)

5.3 MACH NUMBER EFFECT

To study the effect of Mach number variation, three Mach number values, 0.3, 0.45 and 0.6, were considered at every center of gravity and tail size value in the analysis matrix. For ease, effect of Mach number variation at CG = 30%, Tail Size = 100% condition was thoroughly examined throughout this section. For the results of the other cases, APPENDIX A should be referred.

From Figure 55 to Figure 59, pitch angle (θ) obtained from two methodologies at three Mach numbers were plotted with respect to time. To ease the reader, plots are organized so that either the methodologies (Figure 55 to Figure 57) or either the Mach number effect are compared. (Figure 58, Figure 59)

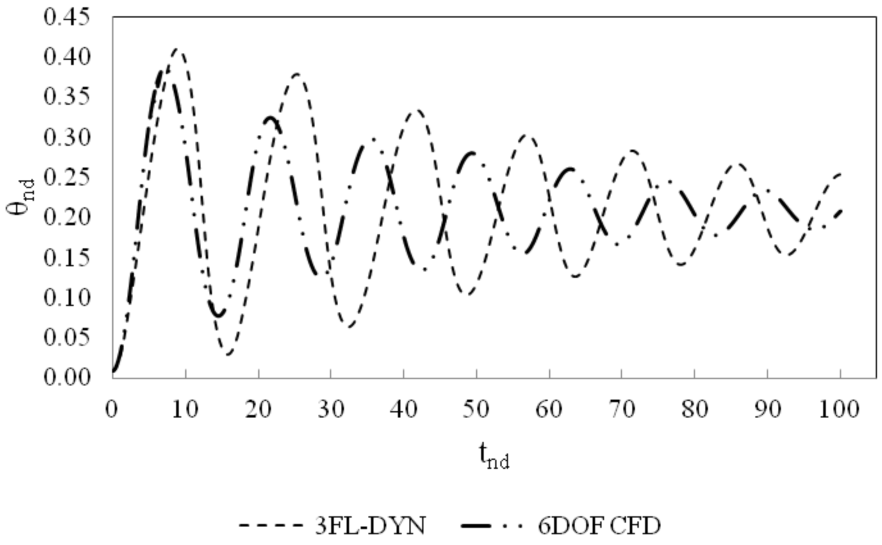

Figure 55. Non-dimensional Theta vs. Time 3FL-DYN / 6DOF CFD comparison for M = 0.6, CG = 30%, Tail = 100%

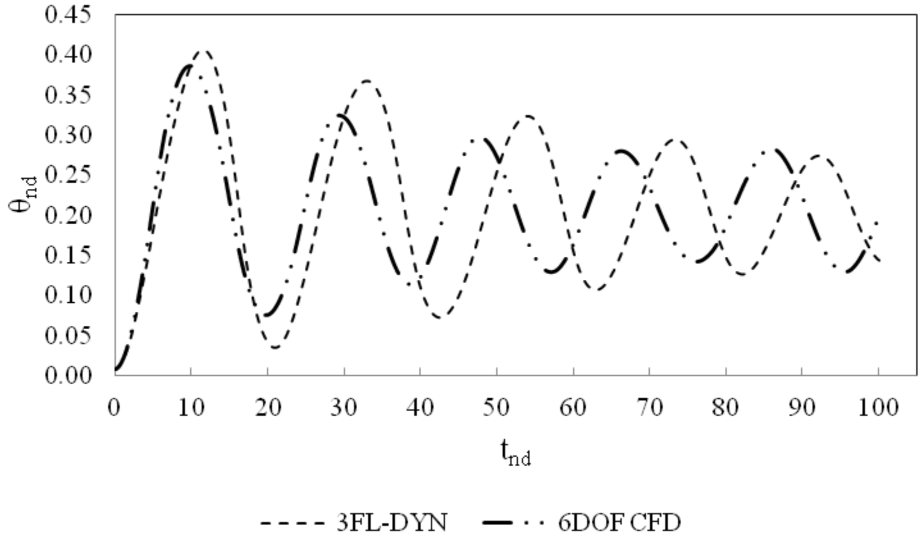

Figure 56. Non-dimensional Theta vs. Time 3FL-DYN / 6DOF CFD comparison for M = 0.45, CG = 30%, Tail = 100%

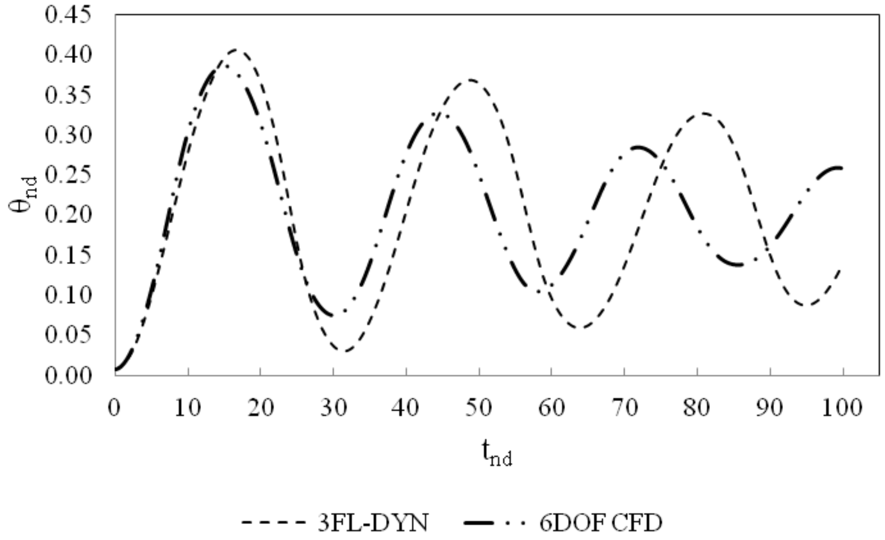

Figure 57. Non-dimensional Theta vs. Time 3FL-DYN / 6DOF CFD comparison for M = 0.3, CG = 30%, Tail = 100%

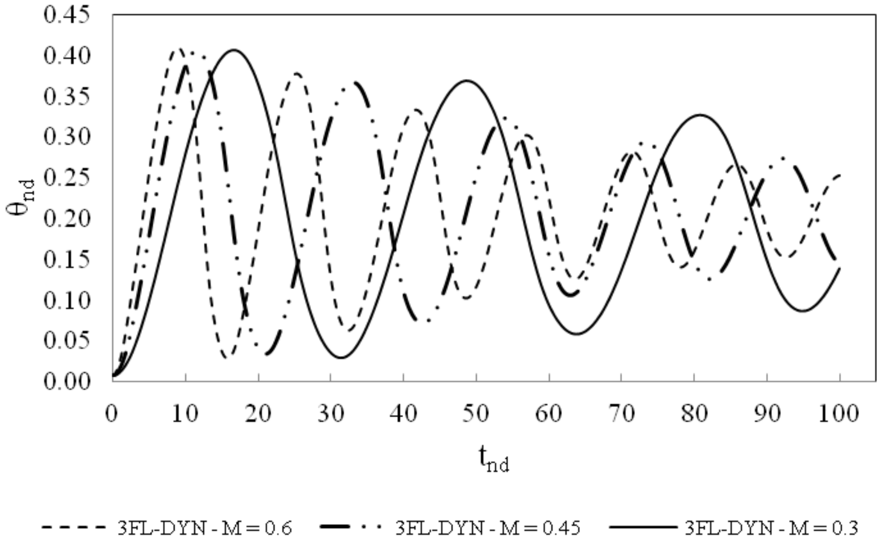

Figure 58. 3FL-DYN Non-dimensional Theta vs. Time comparison of three Mach number values for CG = 30%, Tail = 100%

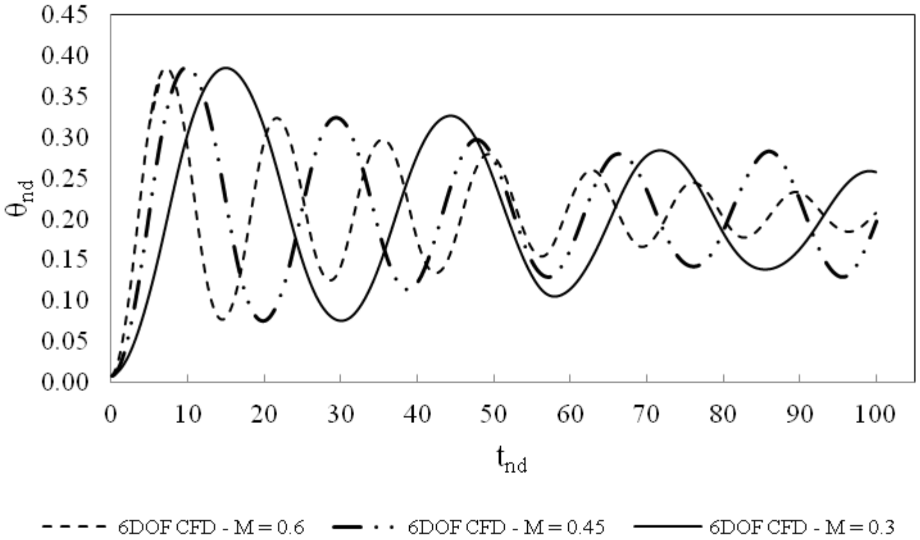

Figure 59. 6DOF CFD Non-dimensional Theta vs. Time comparison of three Mach number values for CG = 30%, Tail = 100%

When the 3FL-DYN results with the 6DOF CFD results are compared, it is clear that the magnitude of the oscillations of pitch angle (θ) are overestimated by the 3FL-DYN. This is due to the fact that being similar to the center of gravity cases, dissipation due to damping mechanisms in lateral direction causes the oscillations to decay faster. When the rate of change of the magnitudes of the oscillations and rate of change of position affecting the damping derivatives are considered, higher the

Mach number, higher the difference between the two methodologies is. Trendwise, 3FL-DYN was able to capture the frequency increasing with Mach number. As the magnitude and frequency of the oscillations are higher in 3FL-DYN, this method is more conservative for initial design purposes.

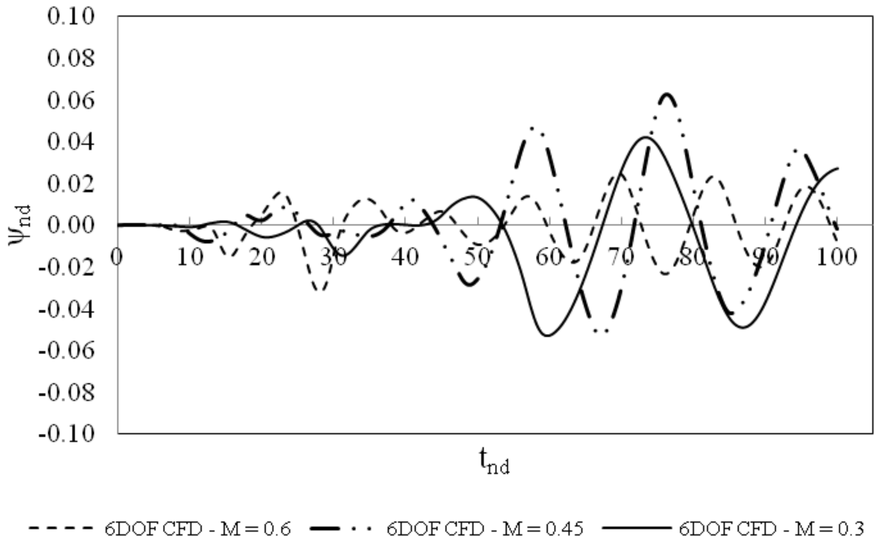

Figure 60. 6DOF CFD Non-dimensional Psi vs. Time comparison of three Mach number values for CG = 30%, Tail = 100%

The yawing motion of the decoy can be observed from Figure 60. All of the cases have continuous rolling motion as can be seen from APPENDIX A. As explained thoroughly in Section 5.2, due to the fact that the decoy is exposed to high angles of attack, lateral out-of-plane forces and large side forces occur causing motion in lateral direction. [22] The forces and moments are larger for M = 0.6 case, hence the continuous rolling motion is more effective compared to other Mach numbers. Trendwise, higher the Mach number, higher the forces / moments and more effective the rolling motion is. Examining the yawing motion, it is clear that the highest magnitude of oscillations is 7-8 times smaller than that of the motion in pitching direction.

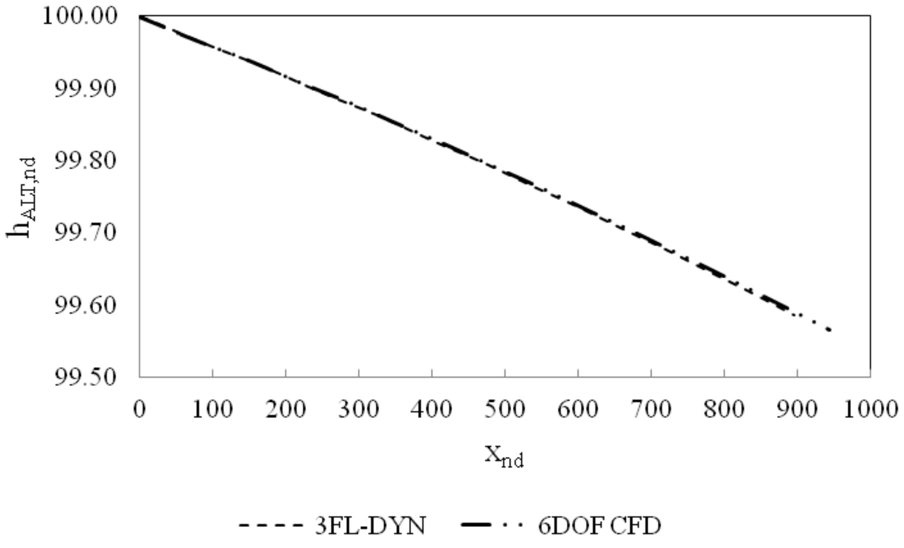

Figure 61. 3FL-DYN / 6DOF CFD Trajectory Comparison for M = 0.6, CG = 30%, Tail = 100%

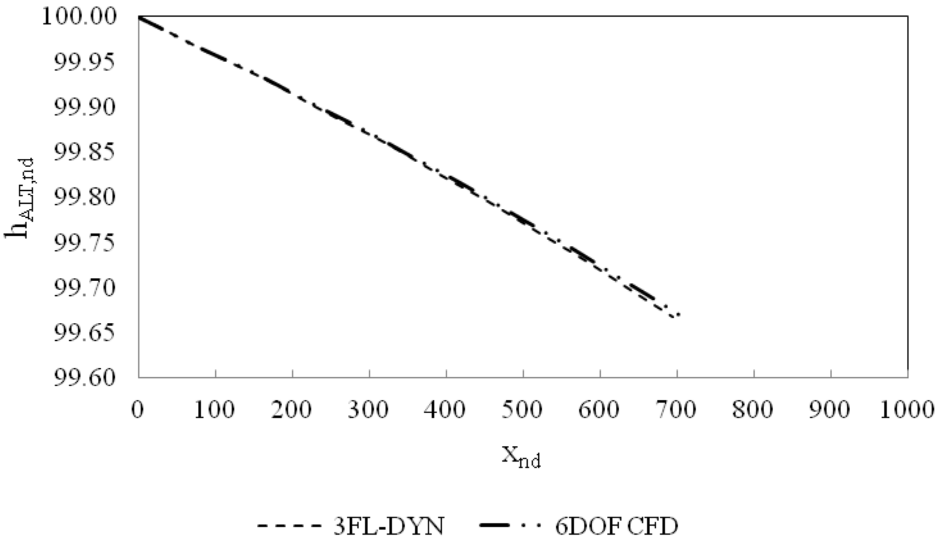

Figure 62. 3FL-DYN / 6DOF CFD Trajectory Comparison for M = 0.45, CG = 30%, Tail = 100%

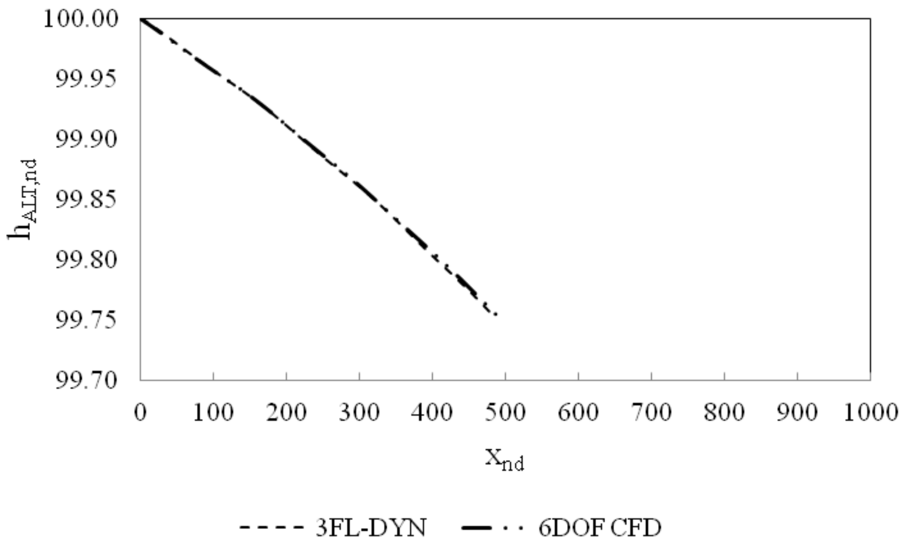

Figure 63. 3FL-DYN / 6DOF CFD Trajectory Comparison for M = 0.3, CG = 30%, Tail = 100%

Concerning the trajectories drawn for different Mach numbers, it is obvious that, taking Figure 61 to Figure 63 into account, they are captured very well by 3FL-DYN. Translation in lateral direction is not comparable to that of the longitudinal direction.

Mach number distributions around a plane cutting the decoy at different time points with a non-dimensional time interval of 20 are given in Figure 64. The tail portion of the decoy was made transparent to ease the observation of the Mach distribution on the cutting plane. It is clear that taking the size of the separation zones, especially “a” and “b” time points, into account, the decoy is exposed to high angles of attack at every Mach number case. This results in a lateral motion explained above, as can be observed from the other time points in terms of decoy position. As time marches on due to the stabilization of the decoy, the separation zone sizes begin to decrease as the angle of attack values start to decrease. Motion history of the decoy is not given as due to the horizontal distances covered by the three Mach number cases are different.

Concerning the Mach number effect at different center of gravity and tail size values, given in APPENDIX A, the comparisons of pitch angles and trajectories as well as the flowfield proved to be consistent with the results explained above.

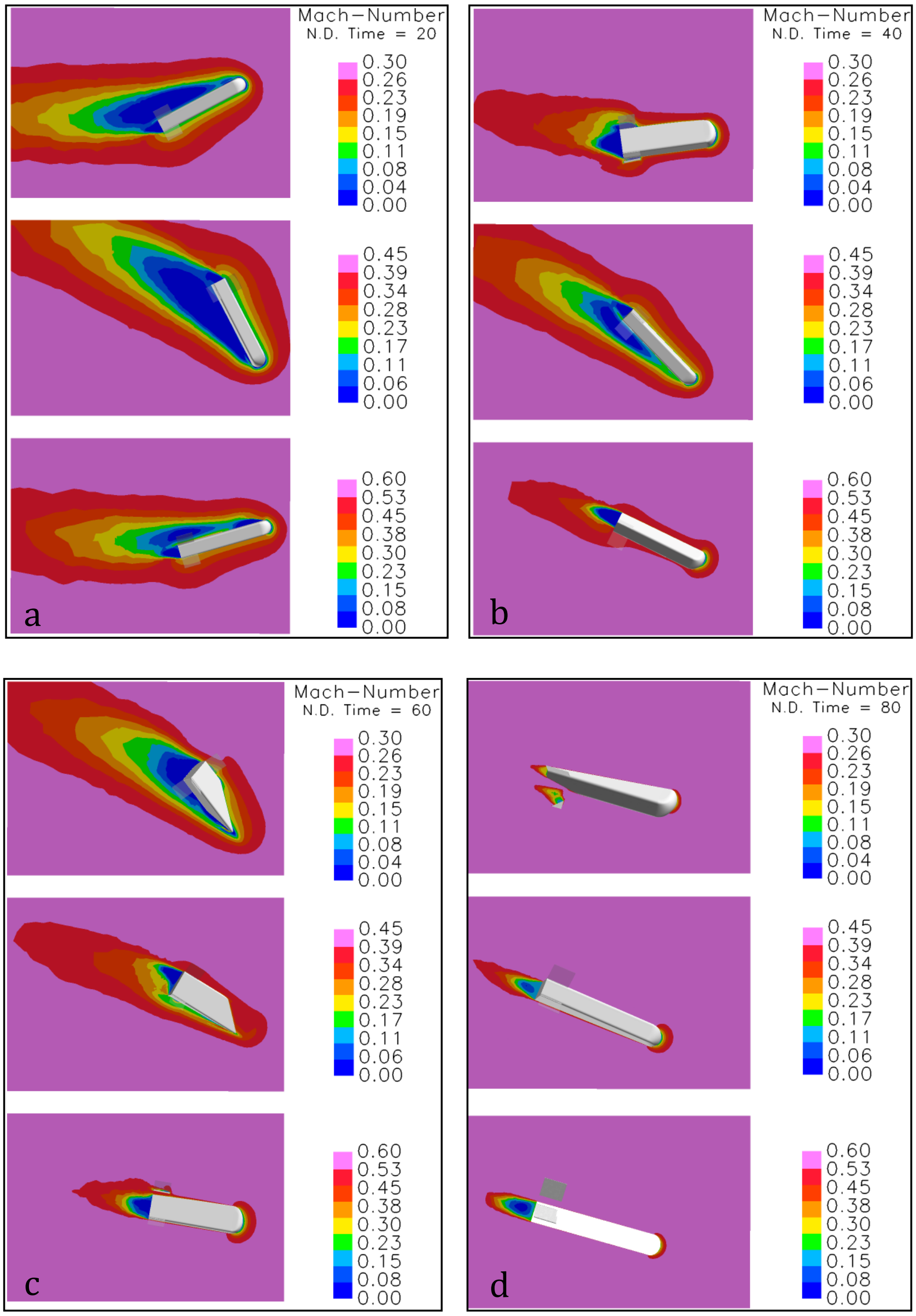

Figure 64. Mach Number distribution around the decoy at different time points a, b, c, d with 20 non-dimensional time interval obtained from 6DOF CFD analyses for three different Mach Number values for CG = 30%, Tail = 100%
(M = 0.3 : Top, M = 0.45 : Middle, M = 0.6 : Bottom)

5.4 TAIL SIZE EFFECT

Investigation of the effects of tail size variation was done by considering two different tail sizes. Only the chord lengths of the tail were changed. The tail sizes of 80% and 100% were investigated at every Mach number and center of gravity value present in the analysis matrix. For convenience, the effects of tail size variation of the CG = 30%, M = 0.6 condition was considered for this section. APPENDIX A includes the other cases at different CG and Mach number values.

From Figure 47 to Figure 50, pitch angle (θ) obtained from two methodologies at two center of gravity locations were plotted with respect to time. To ease the reader, plots are organized so that either the methodologies (Figure 47, Figure 48) or either the effect of center of gravity position is observed. (Figure 49, Figure 50)

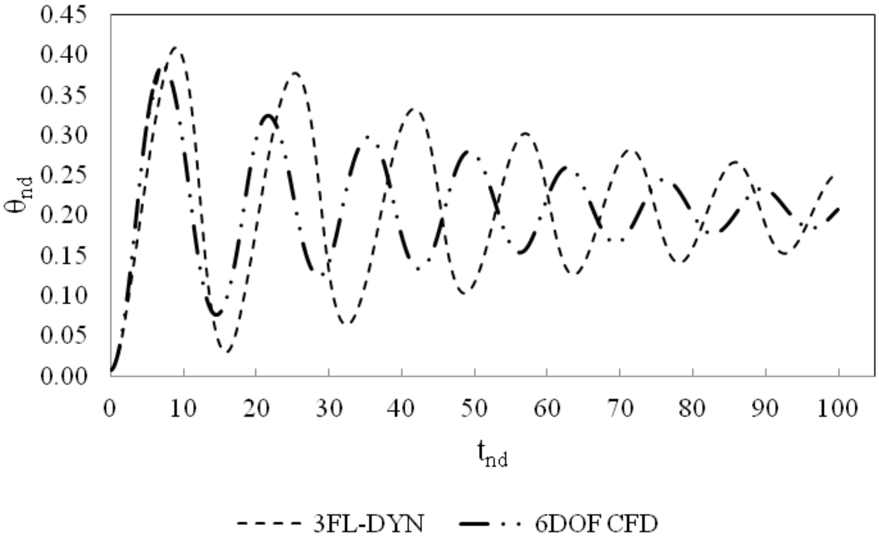

Figure 65. Non-dimensional Theta vs. Time 3FL-DYN / 6DOF CFD comparison for M = 0.6, CG = 30%, Tail = 100%

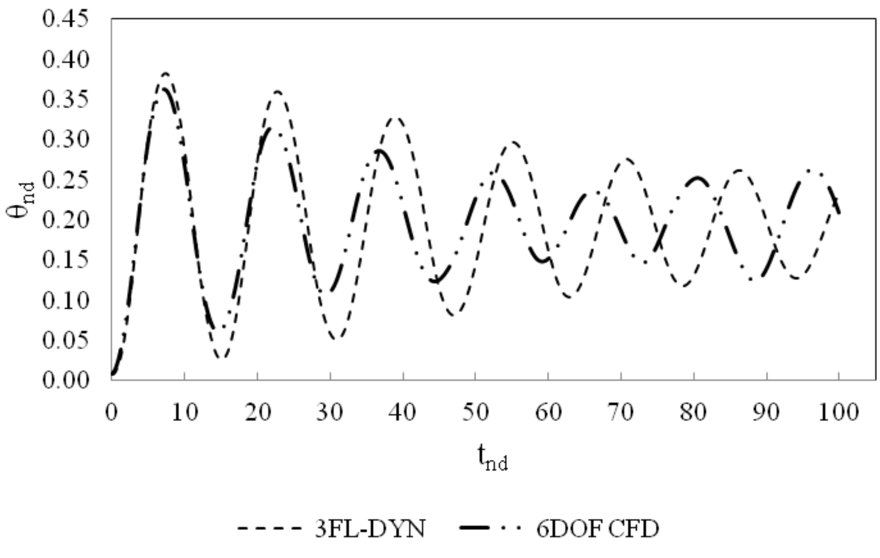

Figure 66. Non-dimensional Theta vs. Time 3FL-DYN / 6DOF CFD comparison for M = 0.6, CG = 30%, Tail = 80%

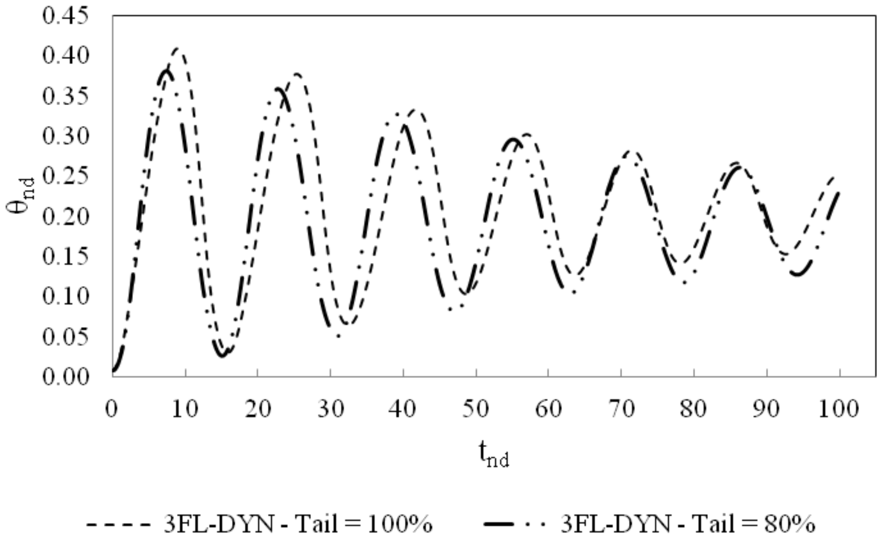

Figure 67. 3FL-DYN Non-dimensional Theta vs. Time comparison of two tail size values for M = 0.6, CG = 30%

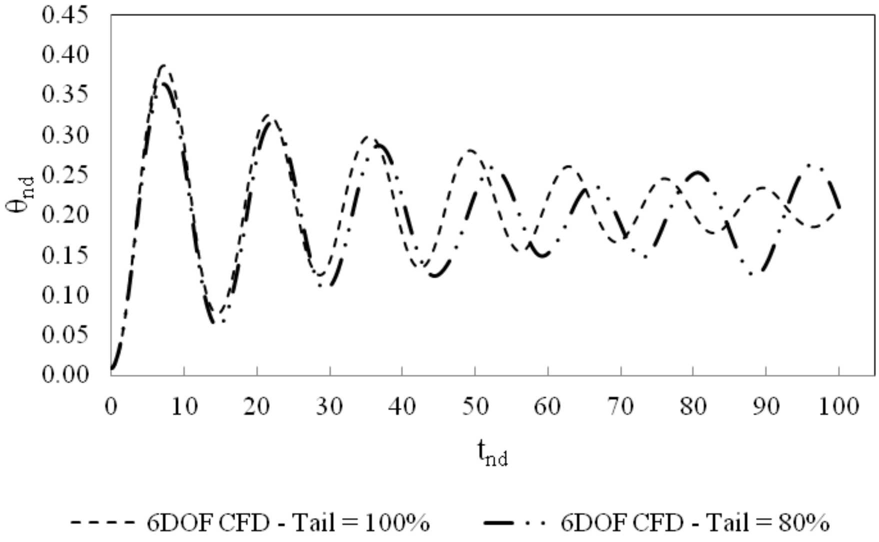

Figure 68. 6DOF CFD Non-dimensional Theta vs. Time comparison of two tail size values for M = 0.6, CG = 30%

The effect of tail size is similar to that of the center of gravity effect, especially in terms of stability. Increasing the tail size has the same effect as positioning the center of gravity to a location more closer to the nose. For instance, similar to the effect observed for CG = 10% case in Section 5.2, the 3FL-DYN results for the Tail = 80% case are closer to 6DOF CFD results than that of the Tail = 100% case. Especially, the magnitude of oscillations is very similar. The CG = 30% case had a larger moment arm, hence larger pitching moments resulting in higher angular accelerations. This is the same situation for the Tail = 100% case. The higher force on the tail section of the decoy can be seen from Figure 69 for the initial time step. There is more area with high pressure values for the Tail = 100% as expected, resulting in a higher moment value hence higher angular acceleration. For the purpose of initial design, as the magnitudes of oscillations are higher for the 3DOF method compared to 6DOF CFD results, the 3DOF method is more conservative.

From Figure 67 and Figure 68, it is observed that the increase in 20% tail size has less effect than an increase in 20% center of gravity location. An increase in 20% tail size results in more similar frequency and magnitudes of oscillations compared to a 20% increase in center of gravity position.

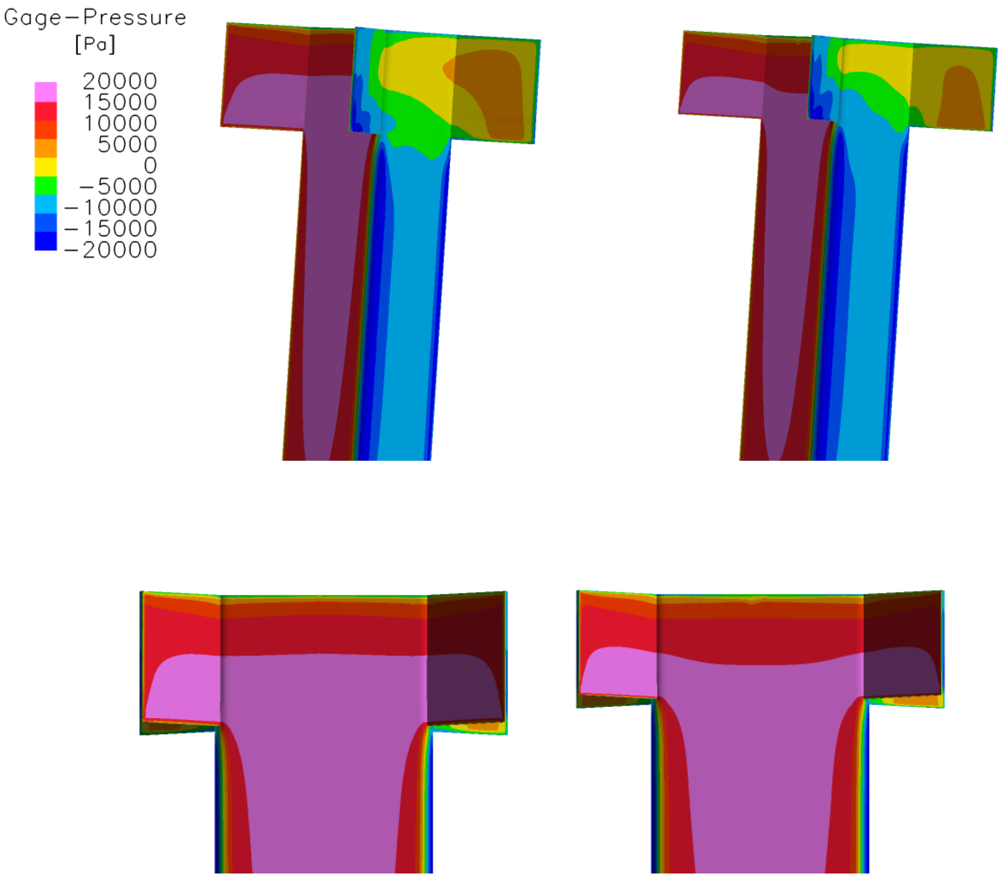

Figure 69. Pressure distribution on the tail section of the decoy for two different tail sizes at initial time step (Tail = 100% : Left, Tail = 80% Right)

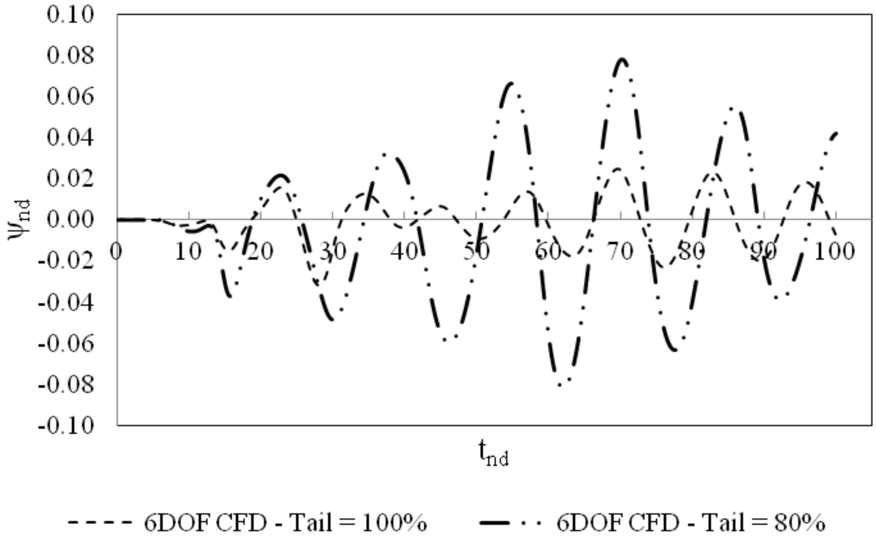

Figure 70. 6DOF CFD Non-dimensional Psi vs. Time comparison of two tail size values for M = 0.6, CG = 30%

The lateral motion in the yaw direction can be observed in Figure 70. All of the cases have continuous rolling motion as can be seen from APPENDIX A. Similar to the cases presented in the previous sections, there is a continuous rolling motion for both tail size values as expected due to lower roll mass moment of inertia. The decoy with a smaller tail size value starts the continuous rolling motion sooner than the Tail = 100% case due to smaller correcting moments in lateral direction. There is motion in yaw direction for both cases, but the magnitudes of the yaw angle oscillations are smaller for Tail = 100% case. This is due to larger correcting yawing moments as expected. The highest magnitude of the yaw angle oscillations is 5-6 times smaller than that of the pitching angle oscillations.

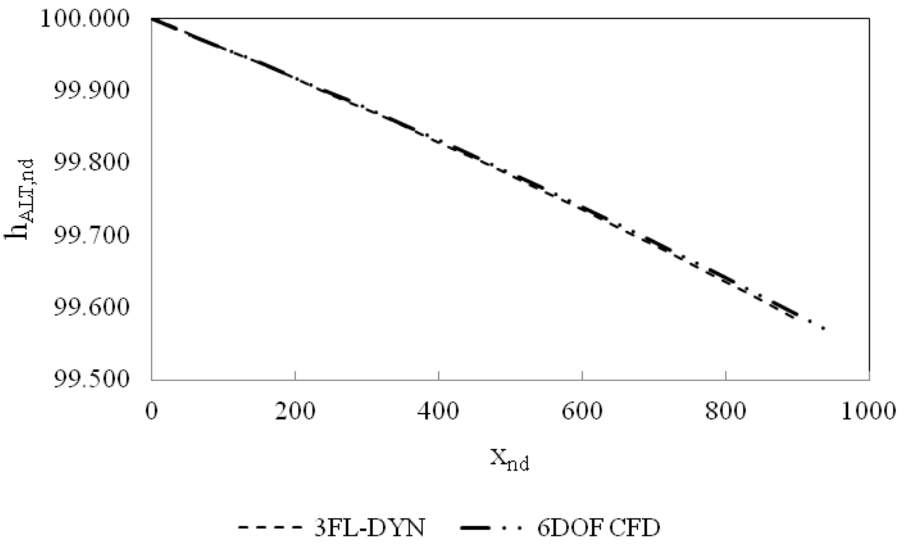

Figure 71. 3FL-DYN / 6DOF CFD Trajectory Comparison for M = 0.6, CG = 30%, Tail = 100%

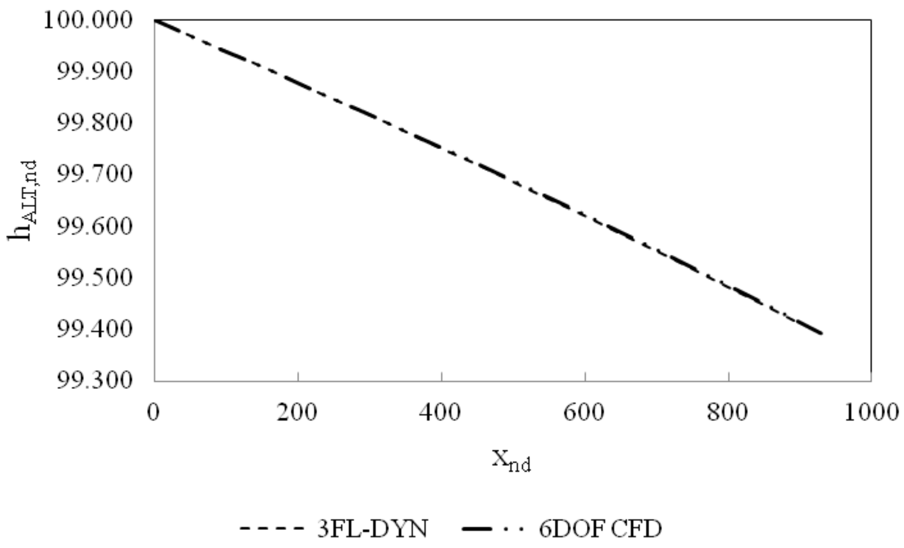

Figure 72. 3FL-DYN / 6DOF CFD Trajectory Comparison for M = 0.6, CG = 30%, Tail = 80%

Trajectory-wise, for both cases, 3FL-DYN results seem to agree very well with 6DOF CFD results which can be seen from Figure 71 and Figure 72. Translation in lateral direction is not comparable to that of the longitudinal direction.

Motion history of the decoy was visualized at two different tail sizes and colored with the gage pressure values obtained from 6DOF CFD in Figure 73. The motion history is given with a non-dimensional time interval of 10, starting from the initial time point similar to the center of gravity effect visualization above. The horizontal and vertical distances covered by the decoy is scaled down to 2.5% while the decoy itself is not scaled down. The rolling motion is apparent for both cases and they both have low pressure zones at the first three time points indicating flow seperation. This shows that the decoy is being exposed to high angles of attack. The low pressure zones diminish at the last time steps indicating the stabilization of the decoy. The pressure distribution of the Tail = 100% case is more uniform as this case stabilizes faster than the Tail = 80% case.

Tail size effect comparisons in terms of pitch angle, trajectory etc. at different center of gravity values and Mach numbers are proved to be consistent with the explanations made above. These results are given in APPENDIX A.

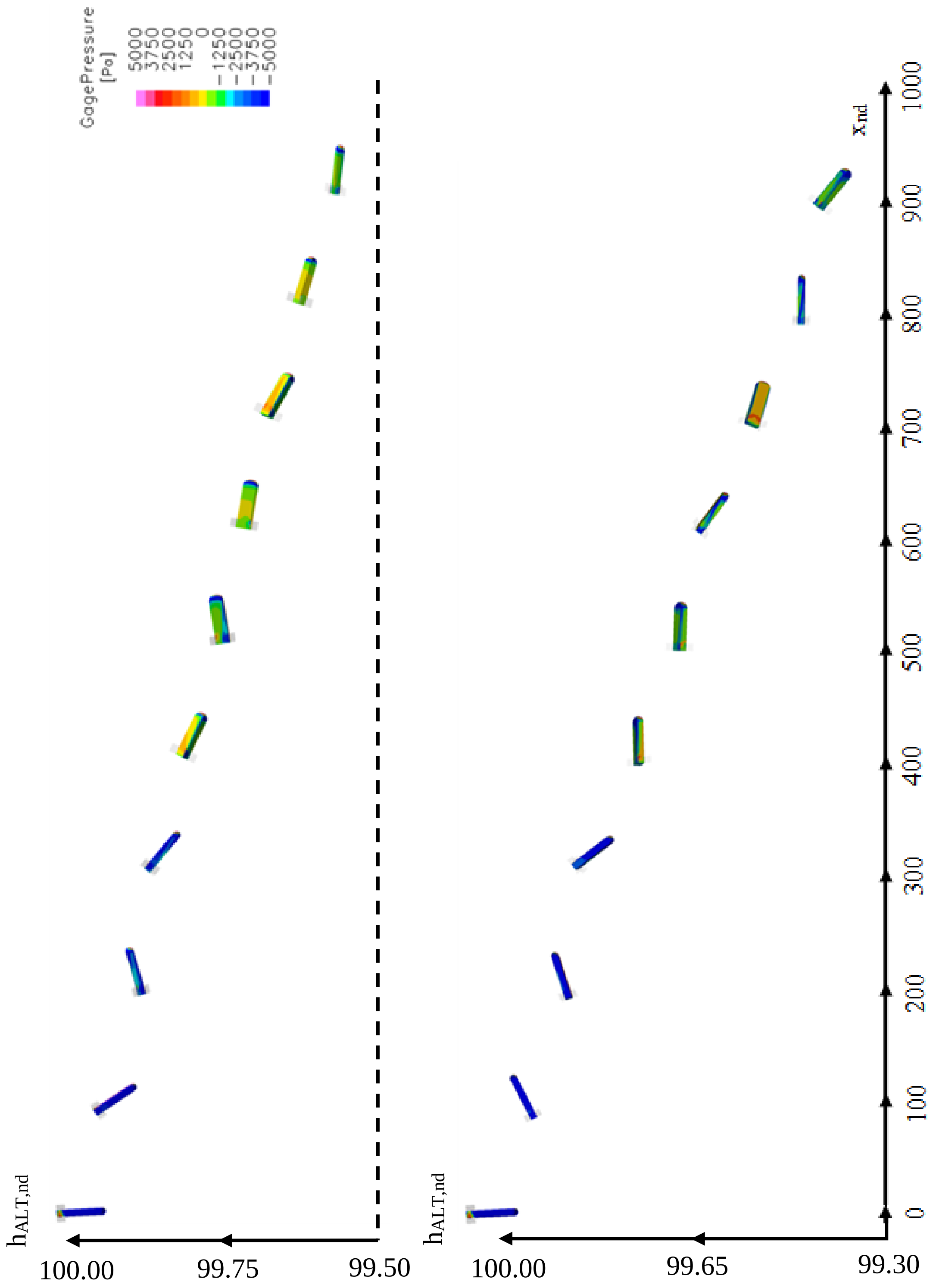

Figure 73. Motion history of the decoy at different time points with 10% time interval obtained from 6DOF CFD analyses colored with the pressure distribution around the decoy for two different tail size values for M = 0.6, CG = 30% (Tail = 100% : Left, Tail = 80% Right)

CHAPTER 6

CONCLUSION AND FUTURE WORK

The thesis has described a fast initial design methodology for a decoy and investigated the validity of the approach. For the decoy, a 3DOF motion assumption was discussed and the equations of motion were derived. The equations were numerically integrated by a code in a quasi-steady manner with the help of tabulated aerodynamic data. The aerodynamic coefficients in the tables were obtained from steady CFD calculations. An attempt to obtain the data by DatCOM did not yield satisfactory results.

An assessment of the methodology was made in terms of time step size selection for both 3FL-DYN and transient CFD calculations, grid independence, inclusion of the pitch damping term and the evaluation of 3DOF assumption. In these studies, time step and the grid size were selected such that the solution is independent from these numerical parameters. During the discussion of pitch damping inclusion, without the pitch damping term, the other terms such as damping caused by drag, lift etc. were found out to be insufficient. 3DOF assumption was evaluated by comparing transient 3DOF CFD and 6DOF CFD results. The results showed that given the decoy has static stability and the motion in the lateral direction is benign, the 3DOF assumption can be made for a level flight condition.

To validate the 3DOF initial design methodology, comparisons between the results obtained from 3FL-DYN and transient 6DOF CFD were carried out. The terms of comparisons were angular / translational velocities, accelerations, trajectories and angular positions. For comparing purposes, instead of expecting the results to be on top of each other, the ability to capture the effects of the variations of different variables such as Mach number, center of gravity and tail sizes was considered. The flowfields of some of the 6DOF CFD results were investigated as well. According to the results, 3FL-DYN was able to capture the effect of the variations of the variables as well as the magnitude / frequency of the oscillations. As expected, the results of the two methodologies were not identical due to lateral motion as expected. But, as 3DOF method was found out to be more conservative, it was deemed sufficient for fast initial design purposes. The trajectories obtained from 3FL-DYN agreed very well with the 6DOF CFD results.

For future studies, the effect of the flowfield around the aircraft, from which the decoy is deployed, should be added to 3FL-DYN as an initial condition. This way, the safe separation of the decoy from the aircraft could be initially evaluated as well. This could be done by using CFD analyses or a panel code. In addition, other configurations different than body-tail should also be investigated. (like wing-body-tail) Besides, as the methodology was compared with transient CFD results for the validation the initial design methodology, the comparison should be done with flight test results of the decoy itself.

REFERENCES

[1] Definition of Decoy, Dictionary.com LLC. http://dictionary.reference.com/browse/decoy, last visited 08.04.2014

[2] Flare CM 218 K7 Type 1 Datasheet, Chemring Countermeasures Ltd. www.chemringcm.co.uk, last visited on 09.04.2014

[3] Milione, R. *Examples of Electronic Warfare Countermeasures.* Institute of Defense and Government Advancement. http://www.idga.org/communications-engineering-and-it/articles/electron-warfare-108, last visited on 08.04.2014

[4] Arnold, R.J. et Epstein C.S. *AGARD Flight Test Techniques Series Volume 5 Store Seperation Flight Testing.* North Atlantic Treaty Organization, p.48,1992.

[5] Jendzurski, J. et Paulter, N.G. *Calibration of Speed Enforcement Down-The-Road Radars.* Journal of Research of the National Institute of Standards and Technology, V.114, May 2009.

[6] Møller, C. *The Theory of Relativity*. Oxford UK: Oxford University Press, p.1, 2nd ed., 1976.

[7] Stengel, R.F. *Flight Dynamics.*Princeton University Press, 2004.

[8] Siouris, G.M. *Missile Guidance and Control Systems.* Springer, 2004.

[9] Brochu, R. et Lestage, R. *Three-Degree-of-Freedom (DOF) Missile Trajectory Simulation Model and Comparative Study with a High Fidelity 6DOF Model.* Defense Research and Development Canada, DRDC Valcaltier, TM 2003-056, 2003.

[10] *Standard Atmosphere.* International Organization for Standardization, ISO 2533:1975, 1975.

[11] Canale R.P. et Chapra, S.C. *Numerical Methods for Engineers.*McGraw Hill, 6th ed., 2009.

[12] Moore, M., Stoy, S. ve Vukelich, S. *Missile DatCOM: Volume 2 - User's Manual.* McDonnell-Douglas Missile Systems Company. Vol.2, p.1,1989

[13] Altair HyperWorks Desktop 11, Altair Engineering Inc., 2011

[14] ANSYS FLUENT 14.5 User's Guide, Fluent Inc., 2012

[15] Versteeg, H. et Malalasekra, W. *An Introduction to Computational Fluid Dynamics.*Pearson, 2nd ed., 2007.

[16] P. A. Davidson. *Turbulence - An Introduction for Scientists and Engineers*. Oxford University Press, 2004.

[17] Moin, P. et Mahesh, K. *Direct Numerical Simulation: A Tool in Turbulence Research.* Annual Reviews of Fluid Mechanics, Vol. 30: 539, 1998.

[18] Rumsey, C.L., Sanetrik, M.D. et al. *Efficiency and Accuracy of Time-Accurate Turbulent Navier-Stokes Computations.* Computers & Fluids. Vol. 25, No. 2, pp.217-236, 1996.

[19] Wilcox, D.C. *Turbulence Modeling for CFD.* DCW Industries, Inc., 1994.

[20] Ogata, K. *System Dynamics*. University of Minnesota, 4th ed., 2005.

[21] Karcz, J et Kacperski, L. *An effect of grid quality on the results of numerical simulations of the fluid flow field in an agitated vessel.*14th European Conference on Mixing, 2012.

[22] Patel, M., Sowle, Z. et al. *Aerodynamic Control of a Small Projectile.*44th AIAA Aerospace Sciences Meeting and Exhibit, AIAA 2006-667, 2006.

[23] Fieldview 12.3 User’s Guide, Intelligent Light, 2010.

[24] Tecplot 360 User’s Guide, Tecplot Inc., 2006.

[25] Blakelock, J. *Automatic Control of Aircraft and Missiles.* John Wiley & Sons, p.230-231, 1991.

APPENDIX A

SUPPLEMENTARY RESULTS

In this part, the pitch and yaw angles as well as the trajectories of the other combinations of center of gravity, Mach number and tail sizings other than the reference case explained in Section 5.1 are given.

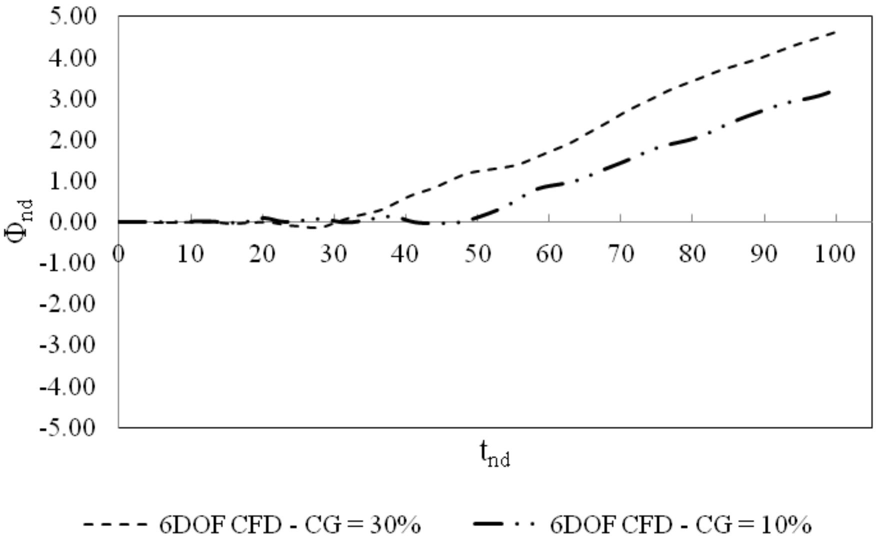

Figure 74. 6DOF CFD Non-dimensional Phi vs. Time comparison of two center of gravity values for M = 0.6, Tail = 100%

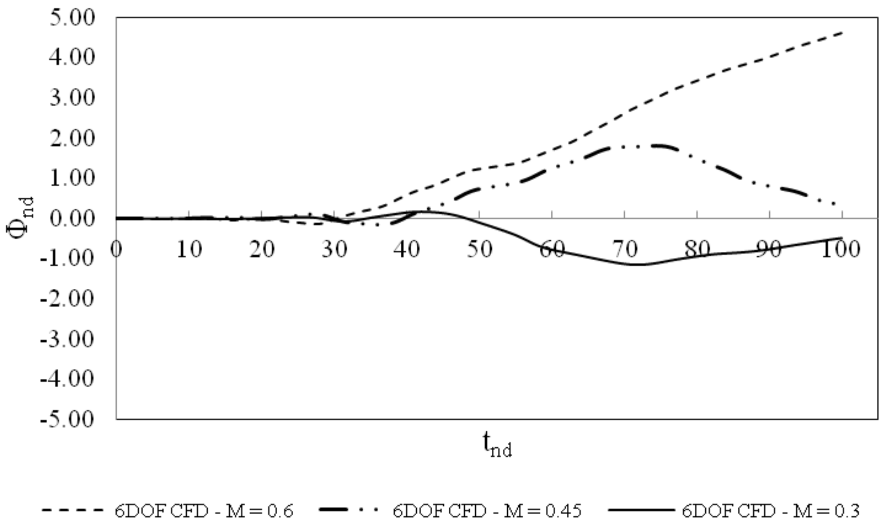

Figure 75. 6DOF CFD Non-dimensional Phi vs. Time comparison of three Mach numbers for CG = 30%, Tail = 100%

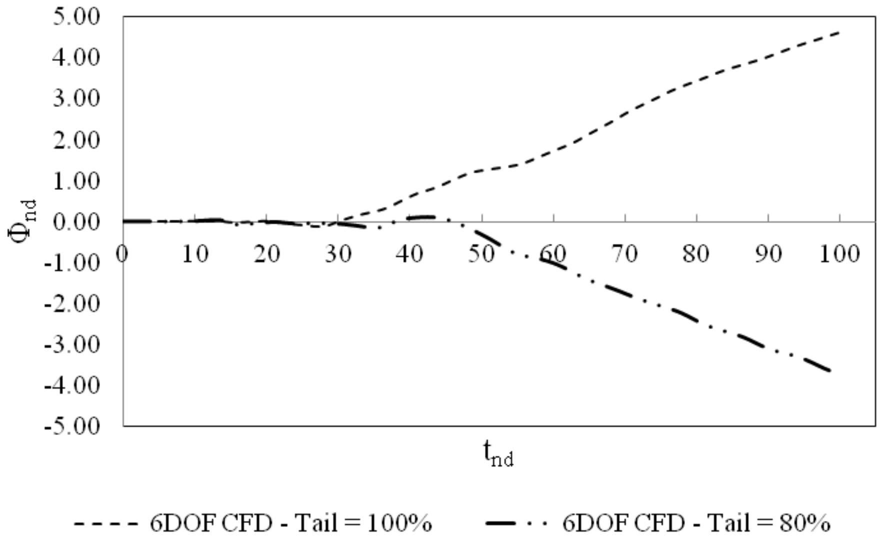

Figure 76. 6DOF CFD Non-dimensional Phi vs. Time comparison of two tail sizes for M = 0.6, CG = 30%

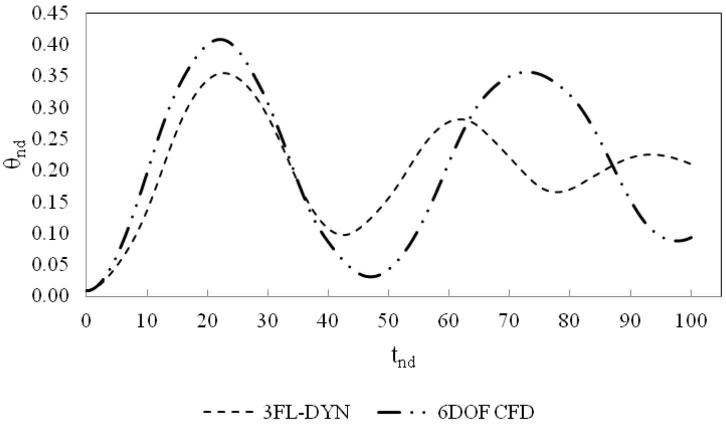

Figure 77. Non-dimensional Theta vs. Time 3FL-DYN / 6DOF CFD comparison for M = 0.3, CG = 10%, Tail = 80%

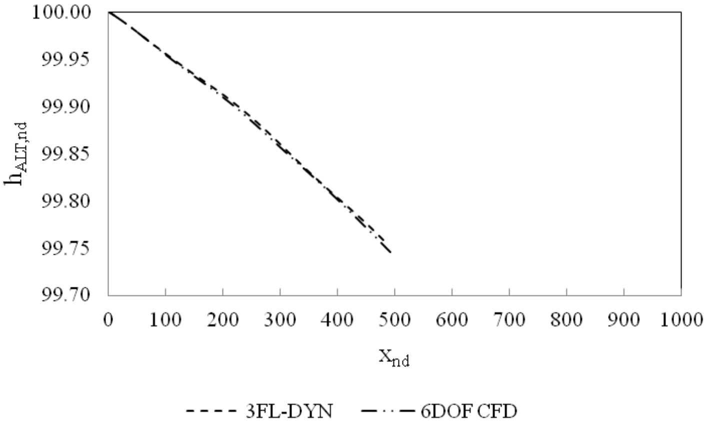

Figure 78. 3FL-DYN / 6DOF CFD Trajectory Comparison for M = 0.3, CG = 10%, Tail = 80%

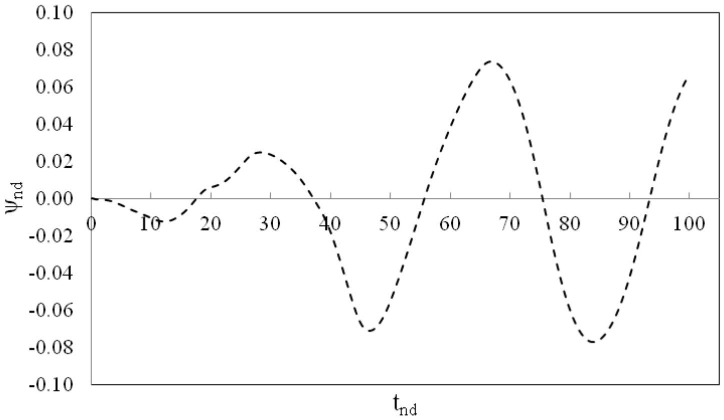

Figure 79. 6DOF CFD Non-dimensional Psi vs. Time for M = 0.3, CG = 10%, Tail = 80%

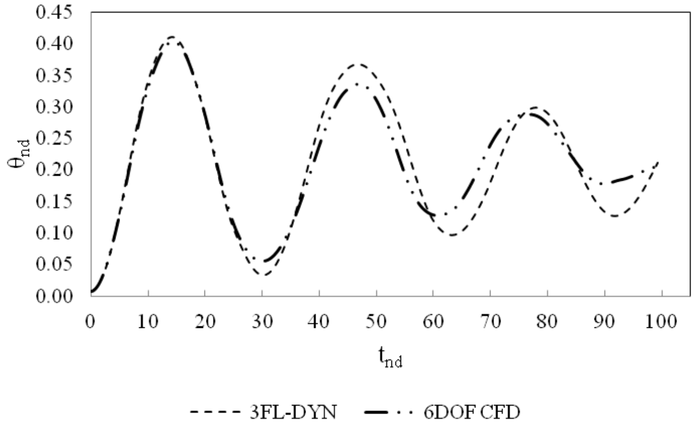

Figure 80. Non-dimensional Theta vs. Time 3FL-DYN / 6DOF CFD comparison for M = 0.45, CG = 10%, Tail = 80%

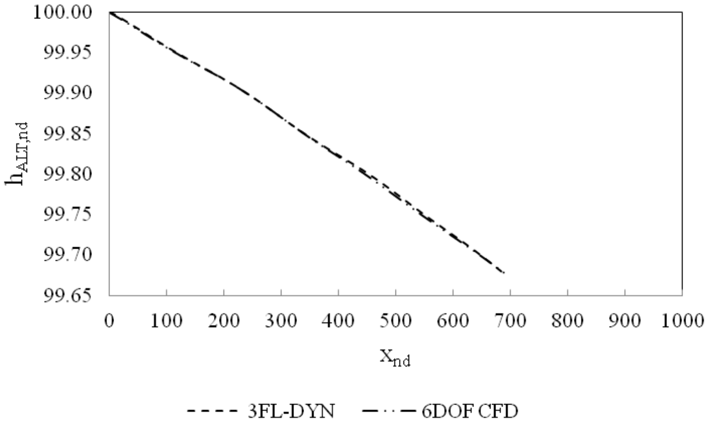

Figure 81. 3FL-DYN / 6DOF CFD Trajectory Comparison for M = 0.45, CG = 10%, Tail = 80%

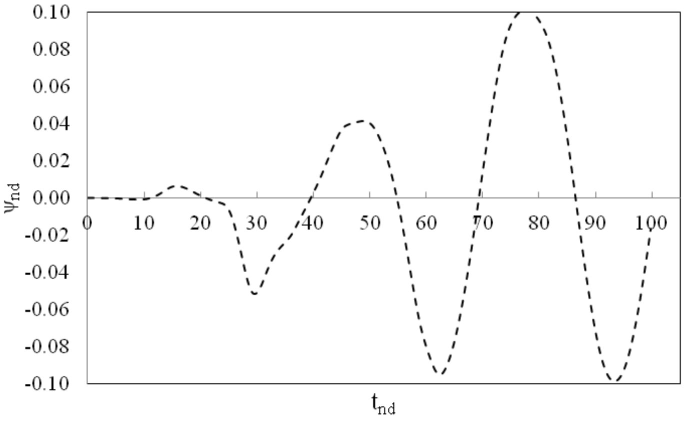

Figure 82. 6DOF CFD Non-dimensional Psi vs. Time for M = 0.45, CG = 10%, Tail = 80%

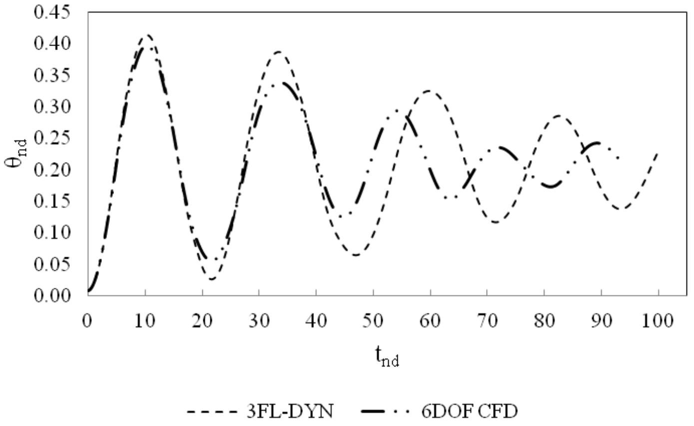

Figure 83. Non-dimensional Theta vs. Time 3FL-DYN / 6DOF CFD comparison for M = 0.6, CG = 10%, Tail = 80%

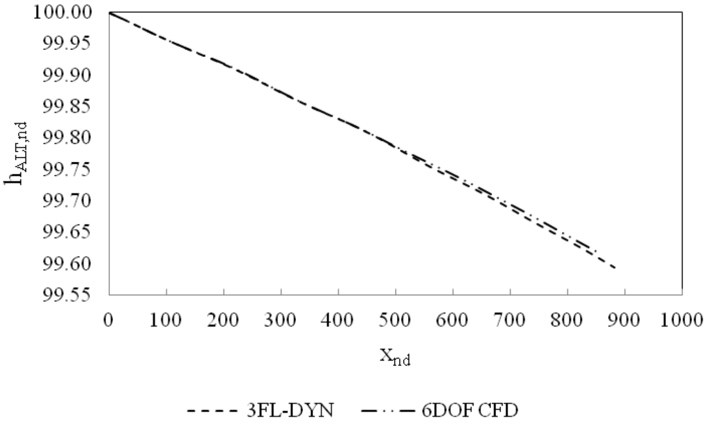

Figure 84. 3FL-DYN / 6DOF CFD Trajectory Comparison for M = 0.6, CG = 10%, Tail = 80%

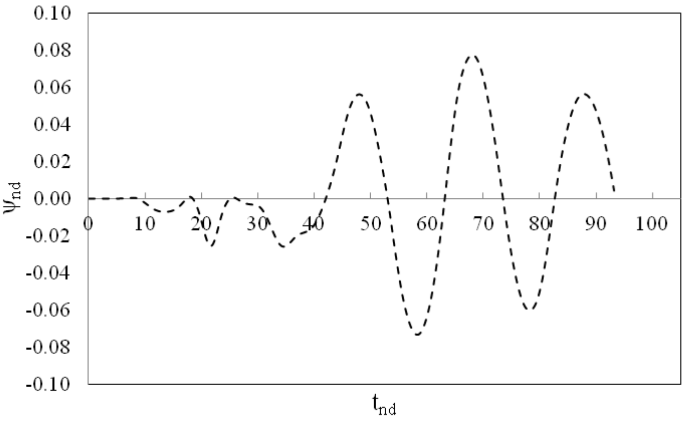

Figure 85. 6DOF CFD Non-dimensional Psi vs. Time for M = 0.6, CG = 10%, Tail = 80%

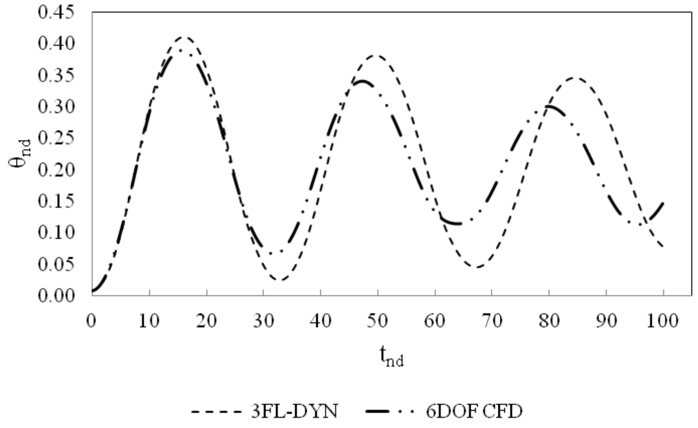

Figure 86. Non-dimensional Theta vs. Time 3FL-DYN / 6DOF CFD comparison for M = 0.3, CG = 30%, Tail = 80%

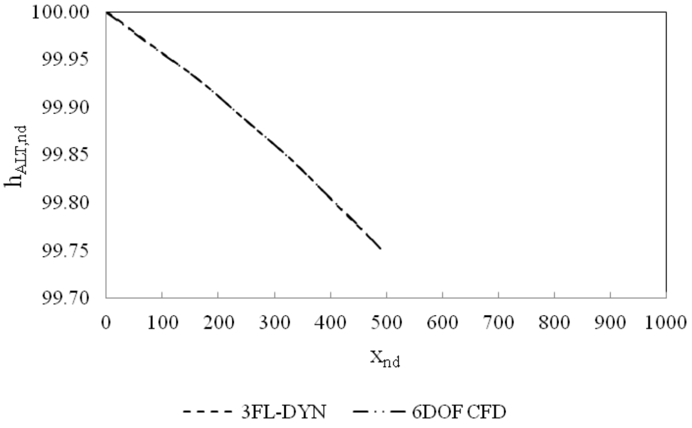

Figure 87. 3FL-DYN / 6DOF CFD Trajectory Comparison for M = 0.3, CG = 30%, Tail = 80%

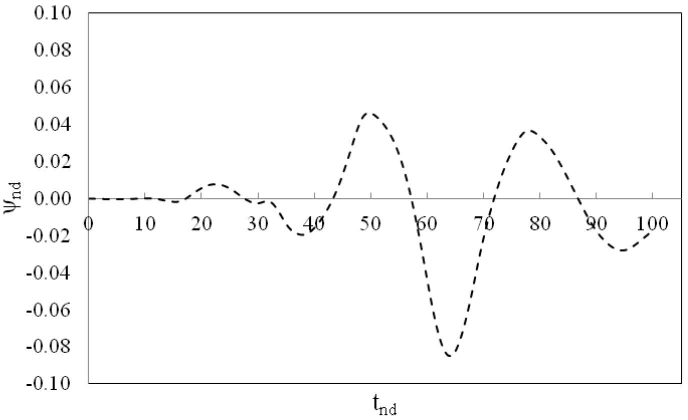

Figure 88. 6DOF CFD Non-dimensional Psi vs. Time for M = 0.3, CG = 30%, Tail = 80%

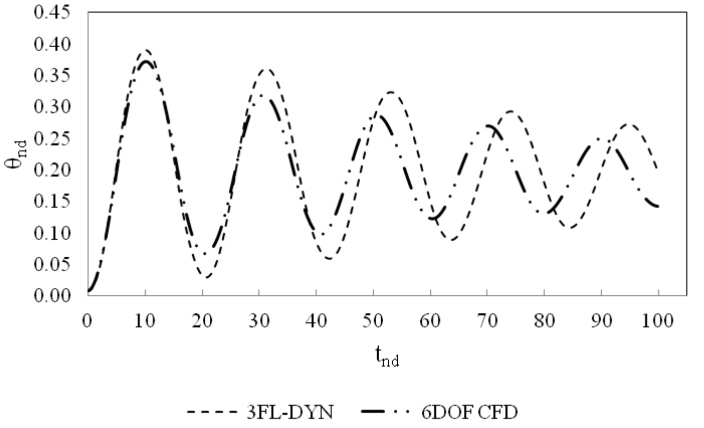

Figure 89. Non-dimensional Theta vs. Time 3FL-DYN / 6DOF CFD comparison for M = 0.45, CG = 30%, Tail = 80%

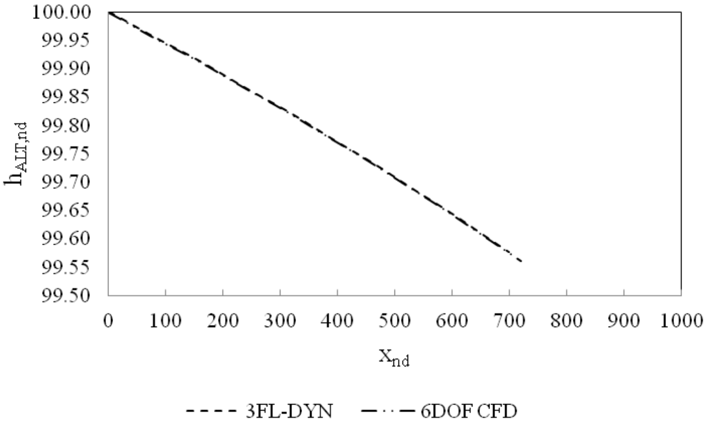

Figure 90. 3FL-DYN / 6DOF CFD Trajectory Comparison for M = 0.45, CG = 30%, Tail = 80%

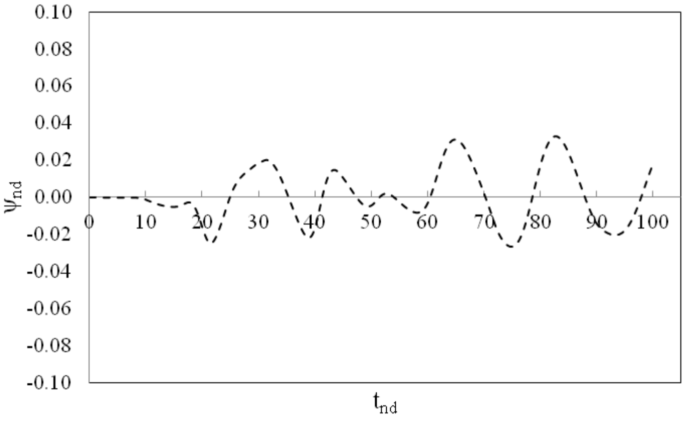

Figure 91. 6DOF CFD Non-dimensional Psi vs. Time for M = 0.45, CG = 30%, Tail = 80%

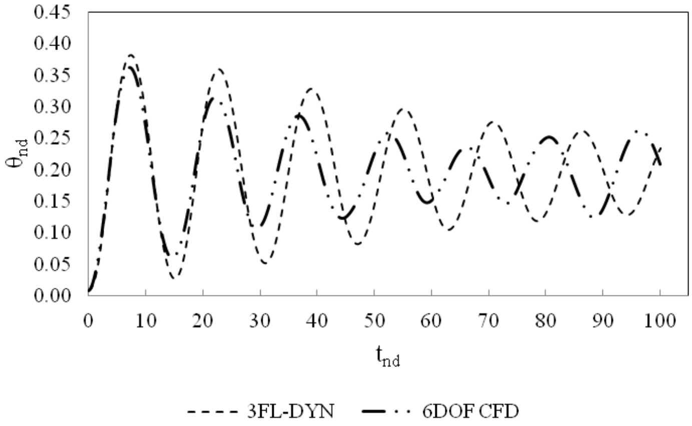

Figure 92. Non-dimensional Theta vs. Time 3FL-DYN / 6DOF CFD comparison for M = 0.6, CG = 30%, Tail = 80%

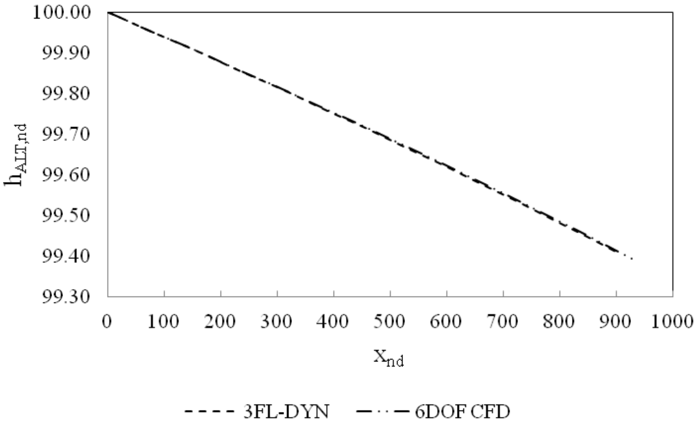

Figure 93. 3FL-DYN / 6DOF CFD Trajectory Comparison for M = 0.6, CG = 30%, Tail = 80%

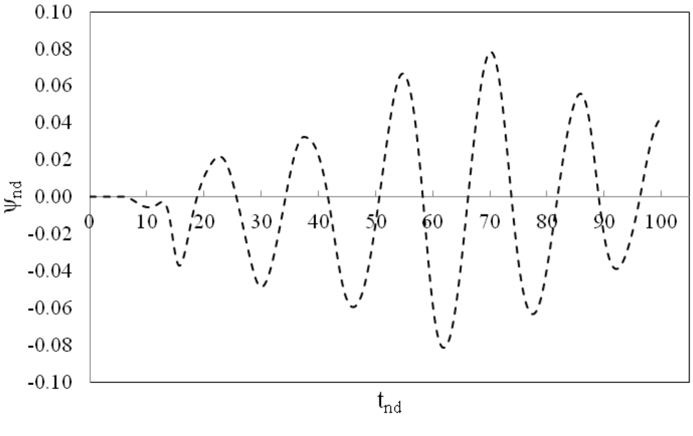

Figure 94. 6DOF CFD Non-dimensional Psi vs. Time for M = 0.6, CG = 30%, Tail = 80%

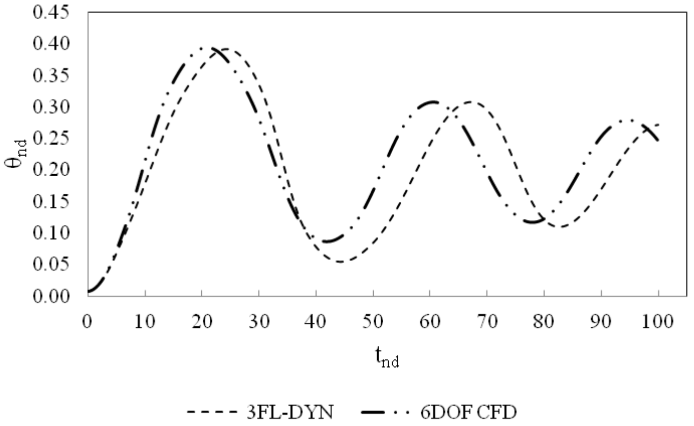

Figure 95. Non-dimensional Theta vs. Time 3FL-DYN / 6DOF CFD comparison for M = 0.3, CG = 10%, Tail = 100%

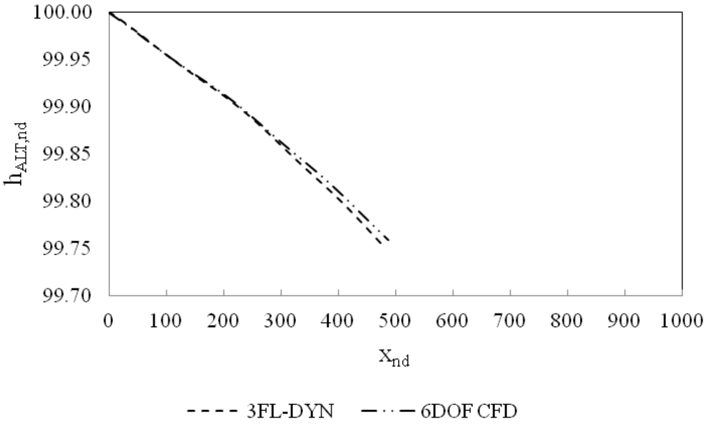

Figure 96. 3FL-DYN / 6DOF CFD Trajectory Comparison for M = 0.3, CG = 10%, Tail = 100%

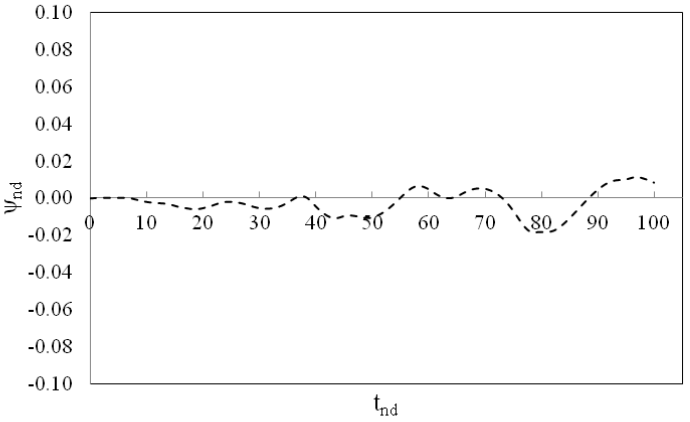

Figure 97. 6DOF CFD Non-dimensional Psi vs. Time for M = 0.3, CG = 10%, Tail = 100%

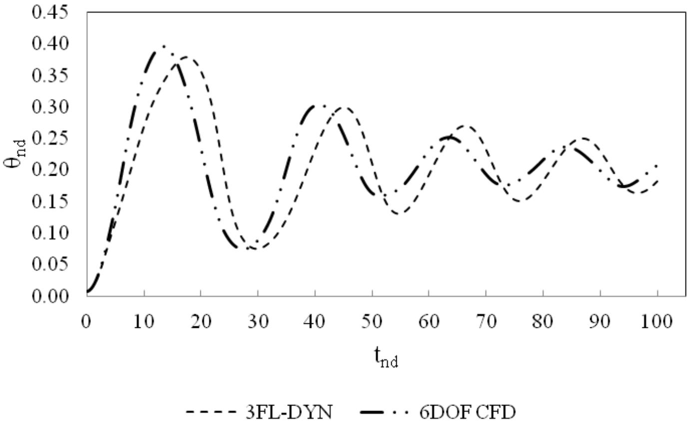

Figure 98. Non-dimensional Theta vs. Time 3FL-DYN / 6DOF CFD comparison for M = 0.45, CG = 10%, Tail = 100%

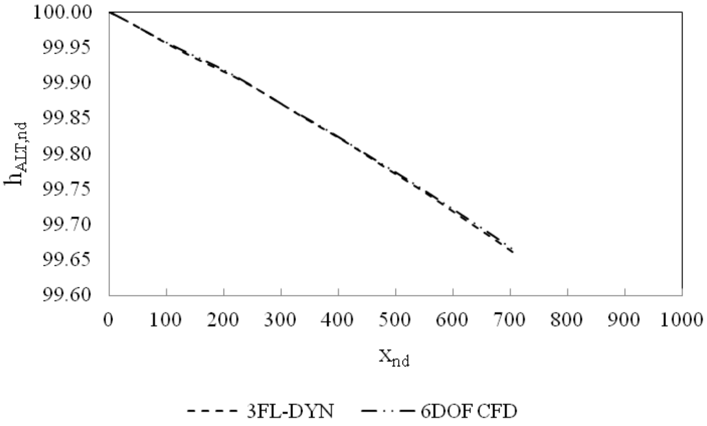

Figure 99. 3FL-DYN / 6DOF CFD Trajectory Comparison for M = 0.45, CG = 10%, Tail = 100%

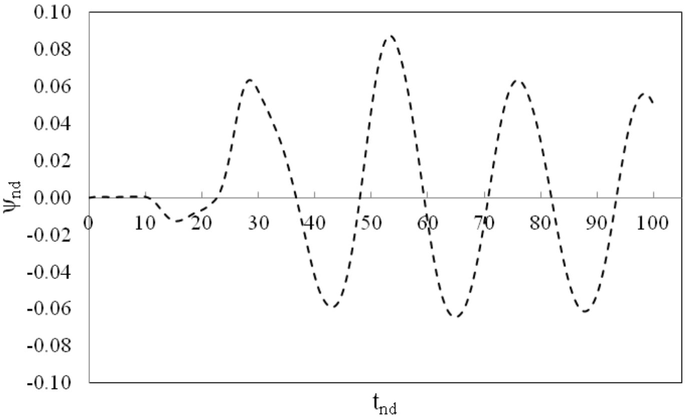

Figure 100. 6DOF CFD Non-dimensional Psi vs. Time for M = 0.45, CG = 10%, Tail = 100%

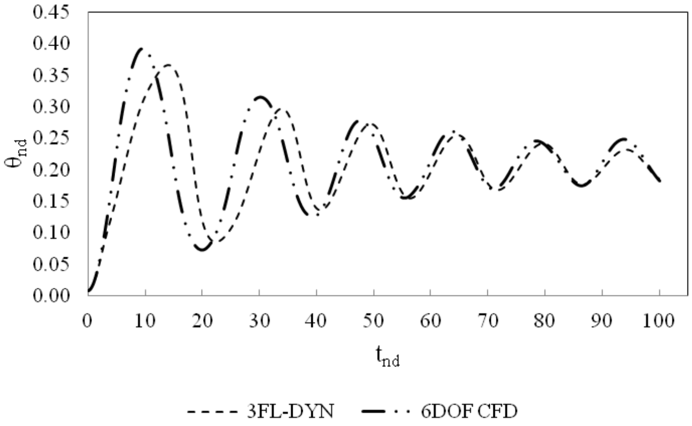

Figure 101. Non-dimensional Theta vs. Time 3FL-DYN / 6DOF CFD comparison for M = 0.6, CG = 10%, Tail = 100%

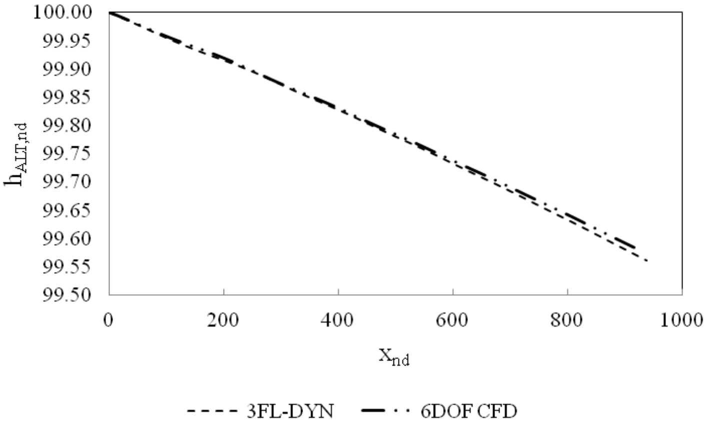

Figure 102. 3FL-DYN / 6DOF CFD Trajectory Comparison for M = 0.6, CG = 10%, Tail = 100%

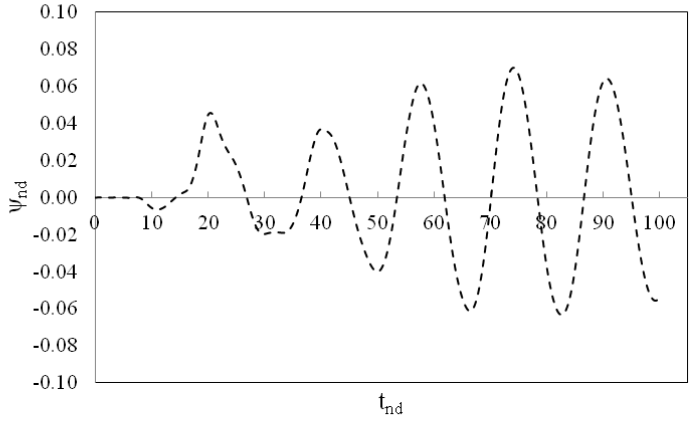

Figure 103. 6DOF CFD Non-dimensional Psi vs. Time for M = 0.6, CG = 10%, Tail = 100%

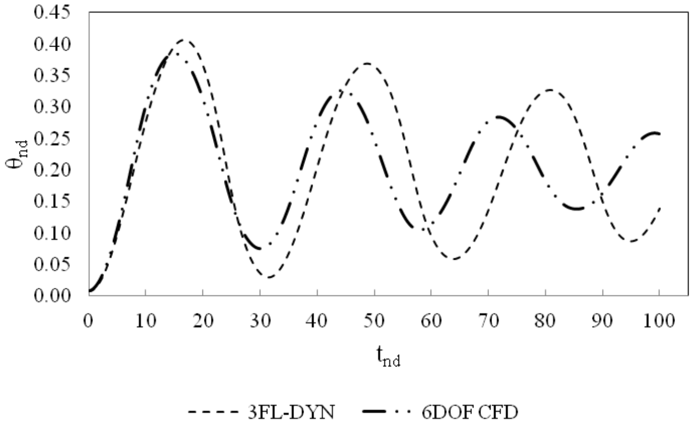

Figure 104. Non-dimensional Theta vs. Time 3FL-DYN / 6DOF CFD comparison for M = 0.3, CG = 30%, Tail = 100%

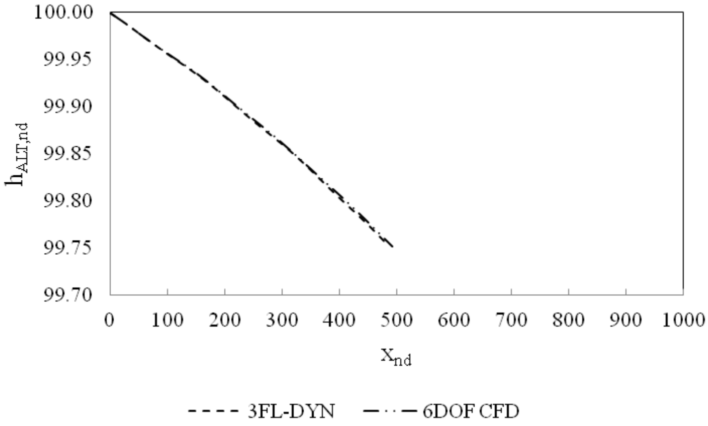

Figure 105. 3FL-DYN / 6DOF CFD Trajectory Comparison for M = 0.3, CG = 30%, Tail = 100%

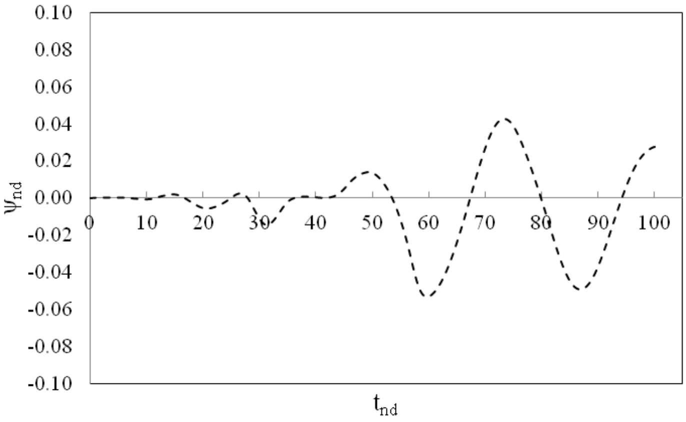

Figure 106. 6DOF CFD Non-dimensional Psi vs. Time for M = 0.3, CG = 30%, Tail = 100%

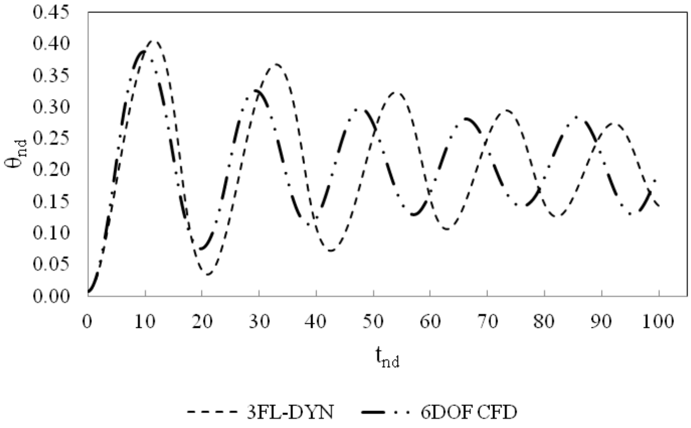

Figure 107. Non-dimensional Theta vs. Time 3FL-DYN / 6DOF CFD comparison for M = 0.45, CG = 30%, Tail = 100%

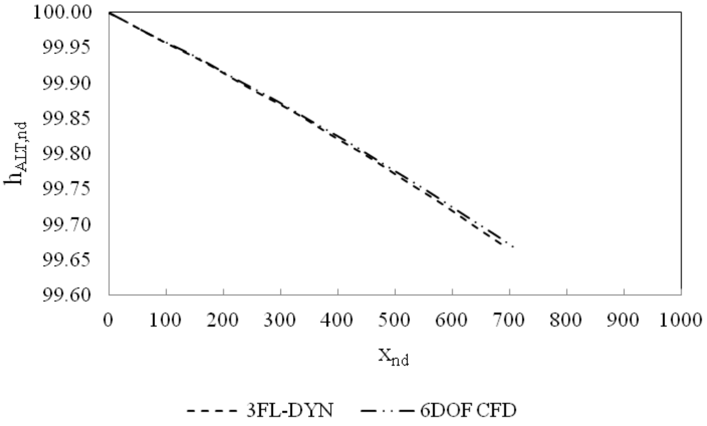

Figure 108. 3FL-DYN / 6DOF CFD Trajectory Comparison for M = 0.45, CG = 30%, Tail = 100%

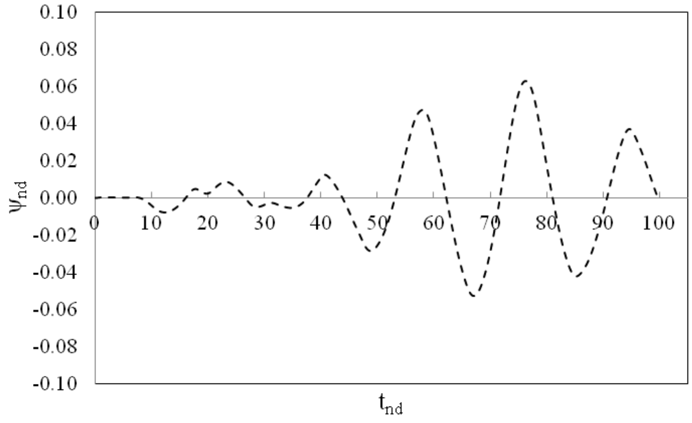

Figure 109. 6DOF CFD Non-dimensional Psi vs. Time for M = 0.45, CG = 30%, Tail = 100%

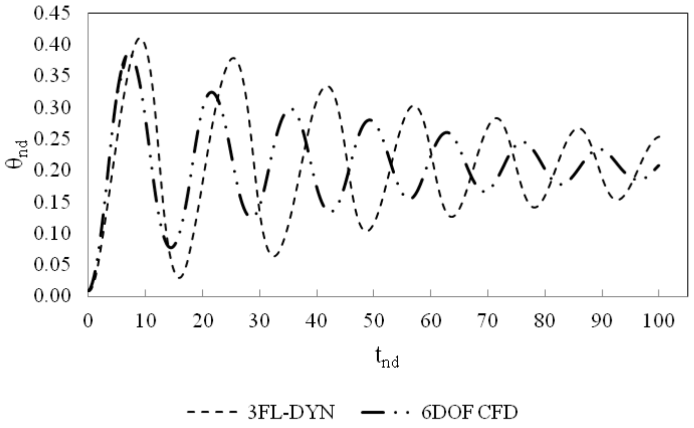

Figure 110. Non-dimensional Theta vs. Time 3FL-DYN / 6DOF CFD comparison for M = 0.6, CG = 30%, Tail = 100%

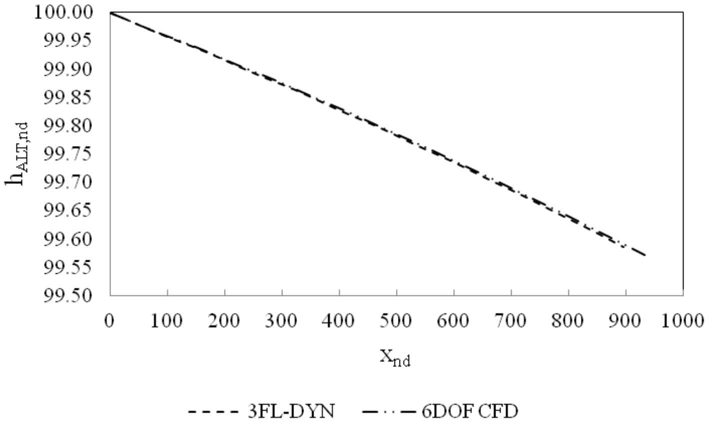

Figure 111. 3FL-DYN / 6DOF CFD Trajectory Comparison for M = 0.6, CG = 30%, Tail = 100%

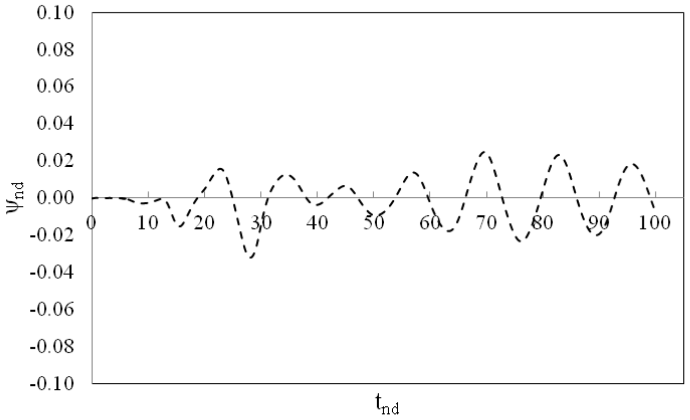

Figure 112. 6DOF CFD Non-dimensional Psi vs. Time for M = 0.6, CG = 30%, Tail = 100%